이 학 박 사 학 위 논 문

Bis(tridentate) Ruthenium(II) Complexes Containing Quinone Substituents or *N*-Heterocyclic Carbene Ligands: Design, Synthesis and Manipulation of Photoinduced Electron Transfer

퀴논 또는 헤테로고리 카벤을 포함하는 루테늄 화합물: 디자인, 합성, 광유도 전자전이 조절

2014년 2월

서울대학교 대학원

화학부 무기화학전공

김 형 묵

Bis(tridentate) Ruthenium(II) Complexes Containing Quinone Substituents or *N*-Heterocyclic Carbene Ligands: Design, Synthesis and Manipulation of Photoinduced Electron Transfer

Supervisor: Prof. Young Keung Chung

By

Hyeong-Mook Kim

A Thesis for Ph.D. Degree

in Inorganic Chemistry

2014

Department of Chemistry

Graduate School

Seoul National University

Table of Contents

Part I. Photoinduced Electron Transfer in Rigid, Cofacially Aligned π-Stacked Ruthenium(II)-Bridge-Quinone Systems

Section 1. Study on Unsymmetric 6-Benzoquinonyl-2,2',6',2"-terpyridine Based on Ru(II) Complexes

Section 2. Study on 1-Benzoquinonyl NN^C Type *N*-Heterocyclic Ligand Based on Ru(II) Complexes

Part II. Manipulation of Optical Band Gap by Controlling the Oxidation Potential in Bis(tridentate) Ru(II) *N*-Heterocyclic Carbene Complexes

Abstract

Part I. Photoinduced Electron Transfer in Rigid, Cofacially Aligned π-Stacked Ruthenium(II)-Bridge-Quinone Systems

Section 1. Study on Unsymmetric 6-Benzoquinonyl-2,2',6',2"-terpyridine Based on Ru(II) Complexes

New π-stacked $[Ru(tpy)_2]^{2+}$ (T_T)-benzoquinone (Q) donor−acceptor (D−A) systems, [Ru(6-(2-cyclohexa-2',5'-diene-1,4-dione)-2,2':6',2"-terpyridine) (2,2':6', 2"-terpyridine)][PF_6]$_2$ (TQ_T), and [Ru(6-(2-cyclohexa-2',5'-diene-1,4-dione)-2,2':6',2"-terpyridine)(4'-phenyl-2,2':6',2"-terpyridine)] [PF_6]$_2$ (TQ_TPh) have been synthesized and characterized. Orthogonal alignment of Q to the tpy ligand imposes this unit juxtaposed cofacially on the central pyridyl ring in another tpy with a typical van der Waals distance. The low-energy electronic absorptions of these complexes are mainly metal-to-ligand charge transfer (MLCT) in nature, similar to that observed in T_T benchmark system, and do not exhibit distinguishable metal-to-Q charge transfer (MQCT) absorption in spite of the proximal location of the electron acceptor unit (Q) to the electron donor unit (T_T). TD-DFT calculation supports the experimental results that the collective oscillator strength of MQCT bands remains

~0.002. Due to the negligible intensity of MQCT bands, evaluation of H_{DA} between the ground and the lowest energy MQCT states are not available through conventional Mulliken-Hush analysis. For such systems, H_{DA} values were successfully evaluated from the relative difference (ξ) of the carbonyl stretching frequency between the neutral Q and its one-electron radical anion, which was determined by an ultrafast visible-pump/mid-IR-probe (TrIR) spectroscopic method. TrIR results showed that the partial charge localized on the Q moiety in the MQCT state was ca. $-0.97e$, and the corresponding H_{DA} was ~1600 cm^{-1}. This value was in good agreement with that estimated by the Mulliken population analysis of the ground-state geometry.

Keywords. ruthenium, quinone, terpyridine (tpy), MLCT, MQCT, photoinduced electron transfer (ET), electronic coupling matrix element (H_{DA}), ultrafast visible pump/mid-IR-probe spectroscopy (TrIR)

Section 2. Study on 1-Benzoquinonyl NN^C Type *N*-Heterocyclic Carbene Based on Ru(II) Complexes

A new π-stacked donor-acceptor (D-A) system, [Ru(1-([2,2'-bipyridine]-6-yl-methyl)-3-(2-cyclohexa-2',5'-diene-1,4-dionyl)-1*H*-imidazole)(2,2':6',2"-

terpyridine)][PF_6]$_2$ (ImQ_T), has been synthesized and characterized. Similar to its precedent, [Ru(6-(2-cyclohexa-2',5'-diene-1,4-dione)-2,2':6',2"-terpyridine)(2,2':6',2"-terpyridine)][PF_6]$_2$ (TQ_T), this system has a cofacial alignment of terpyridine (tpy) ligand and quinonyl (Q) group, which facilitates an electron transfer through π-stacked manifold. Despite the presence of lowest-energy charge transfer transition from the Ru-based-HOMO-to-Q-based-LUMO (MQCT) predicted by theoretical calculations by using time-dependent density functional theory (TD-DFT), the experimental steady-state absorption spectrum does not exhibit such a band. The selective excitation to the Ru-based occupied orbitals-to-tpy-based virtual orbital MLCT state was thus possible, from which charge separation (CS) reaction occurred. The photo-induced CS and thermal charge recombination (CR) reactions were probed by using ultrafast visible-pump/mid-IR-probe (TrIR) spectroscopic method. Analysis of decay kinetics of Q and Q^- state CO stretching modes as well as aromatic C=C stretching mode of tpy ligand gave time constants of <1 ps for CS, 1-3 ps for CR, and 10-20 ps for vibrational cooling processes. The electron transfer pathway was revealed to be Ru-tpy-Q rather than Ru-bpy-imidazol-Q.

Keywords. Ruthenium, NHC, polypyridyl, MLCT, MQCT, electron transfer, charge separation, charge recombination, time-resolved IR spectroscopy

Part II. Manipulation of Absorption Maxima by Controlling the Oxidation Potentials in Bis(tridentate) Ru(II) *N*-Heterocyclic Carbene Complexes

Homoleptic and heteroleptic Ru complexes have been of great interest as sensitizers for a dye-sensitized solar cell (DSSC). Manipulation of redox potential of such complexes is important for improving efficiencies of DSSCs. Here, a series of seven Ru(II) complexes bearing *N*-heterocylic carbene (NHC) ligands (**NNC** or **NN^C**, where NN = bipyridyl, C = NHC, and ^ = methylene spacer) have been newly designed and synthesized. These complexes are fully characterized by ^{1}H and ^{13}C NMR spectroscopy, high-resolution mass spectrometry and elemental analysis. The electronic structures of these complexes were analyzed by spectroscopic and electrochemical methods and further confirmed by theoretical calculations. Voltammetric data show that all complexes possessing NHC ligand exhibited lower $Ru^{II/III}$ oxidation potentials relative to $Ru(tpy)_2$ benchmark mainly due to strong σ-donating properties of NHC ligands. The oxidation potentials of Ru complexes studied in this work are in the following order; $Ru(tpy)_2$ > Ru(tpy)(bzim) > $Ru(bzim)_2$ > Ru(tpy)(im) > Ru(tpy)(^bzim) > $Ru(im)_2$ > $Ru(^im)_2$ > Ru(tpy)(^im) (bzim = 3-([2,2'-bipyridin]-6-yl)-1-methyl-1H-benzimidazolyl, im = 3-([2,2'-bipyridin]-6-yl)-1-methyl-1H-imidazolyl, ^bzim = 3-(2,2'-bipyridine-6-ylmethyl)-1-methyl-1H-benzimidazolyl, ^im = 3-(2,2'-bipyridine-6-ylmethyl)-1-methyl-1H-imidazolyl). Disruption of conjugation between bipyridyl and NHC groups (**NN^C** type ligands)

rather than the mere increase of the number of carbene ligands appear to be more efficient to destabilize the HOMO energy level of these complexes. Theoretical calculation results indicate that the electron densities of HOMOs in Ru(**NNC**)-type complexes are delocalized over Ru metal and **NNC** ligand but those in Ru(**NN^C**)-type complexes are localized within Ru metal and NHC moiety, which is major background of observed oxidation potentials. This work provide an insight in the design motif of Ru complexes in DSSC and other photocatalyst application.

Keywords. ruthenium, NHC, polypyridyl, MLCT, redox potential, ligand field

Student Number: 2007-20302

Background

1. Introduction

Electronic excitation of the 'special pair' of chlorophyll in photosynthetic reaction center in green plants leads to electron transfer to quinone acceptor.[1] This process involves ultrafast electron transfer cascade mechanism and the reaction center is finally returned to its pre-photolysis state by reduction of the oxidized special pair.[2] Over the past decades, the development and understanding of light-driven charge separation and sequential electron transfer in molecular systems have received great attention as methods for converting solar energy into chemical potential and researchers have designed molecular systems that mimic the electron relay in photosynthesis.[3]

Molecular assemblies were synthesized to contain a variety of electron donor (D) and electron acceptor (A) groups. Among them, ruthenium(II) polypyridyl complexes, such as $Ru(bpy)_3^{2+}$ (bpy = 2,2'-bipyridine) and $Ru(tpy)_2^{2+}$ (tpy = 2,2',6',2''-terpyridine) have historically attracted much interest due to their light-induced electron and energy transfer reactions derived from the properties of the lowest excited electron triplet metal-to-ligand charge transfer (^{3}MLCT) state.[4] In particular, $Ru(bpy)_3^{2+}$ and its derivatives were well researched as an artificial photosynthetic device for relative long lifetime, however, this system is sometimes not adequate because substitution on bipyridine decrease the symmetry of the complex, leading to geometric isomers.[5] However, bis(tridentate) complexes have recently adopted for incorporation into larger assemblies, as substitution on the 4′ position leads to linear structures without the bothersome formation of enantiomers or diastereomers. In addition to various functionalization of 4' position on terpyridine, the properties of

bis(tridentate) metal complexes were manipulated by replacing terpyridine with the new types of coordinating ligands, such as *N*-heterocyclic carbene ligand and cyclometalated ligand.[6]

2. Photoinduced Electron Transfer Theory

2.1 Electronic Transition by Light

The photon is treated as quantum energy that can promote an electron in an occupied orbital to a higher energy state of the molecule. This electronic transition will occur only when the quantum energy of the photon precisely matches the energy gap between the initial and the final states of the dye. The efficiency of absorbing light is characterized by the absorbance (A) or transmittance (T), defined as

$$A(\lambda) = \log\left(\frac{I_0}{I}\right) = -\log T(\lambda) = \varepsilon(\lambda) c \ell \qquad \text{(eq. 1)}$$

where I_0 and I are the intensities of the incident light and the transmitted light, respectively. $\varepsilon(\lambda)$, c and ℓ are molar absorption coefficient (L mol^{-1} cm^{-1}), molar concentration of a sample (M) and the length of a cell containing sample (cm), respectively. In many cases, light absorbing molecules in solution follow the eq. 1 (*Beer-Lambert Law*), except at high concentration due to aggregate formation. $\varepsilon(\lambda)$ is an index of light absorbing efficiency at certain wavelength and is proportional to cross-section, the apparent area of absorbing molecule. The relation is given by

$$\varepsilon(\lambda) = \frac{1}{h\ 10} N_A\, \sigma \qquad \text{(eq. 2)}$$

N_A is Avogadro's number, and for molecule with $\varepsilon(\lambda_{max}) = 15000$ M^{-1} cm^{-1}, for example, a ruthenium polypyridyl complex, would correspond to an area of 0.6 $Å^2$.

Electronic transition is viewed as perturbation of the electron by electromagnetic wave. In classical mechanics, a light absorbing molecule was considered as

oscillating dipole and its oscillating property, that is, excitation probability was explained with the term oscillator strength (*f* value) and the equation is

$$f = \frac{8\pi m\tilde{\nu}}{3he^2}\ \mu^2 \qquad \text{(eq. 3)}$$

m and *e* are the mass and charge of electron, respectively and $\tilde{\nu}$ is the wavenumber of light energy for transition and μ is the transition dipole moment integral. *f* is a dimensionless quantity and the value is normalized so that it can range from 0 to 1. A strong transition will have an *f* value close to 1. Quantum mechanical transition moment is a transient dipole resulting from the displacement of charges during the transition between the initial and the final state. Transition dipole moment integral, μ can be expressed as $\langle\Psi_1|\breve{\mu}|\Psi_2\rangle = \int \Psi_1\breve{\mu}\Psi_2 d\tau$, where Ψ_1 and Ψ_2 are wavefunctions at states 1 and 2 respectively and $\breve{\mu}$ is the dipole moment operator.

The probability of a transition is also governed by the selection rules which determine whether the transition is allowed or not. There are major two selection rules for absorption transition, spin-forbidden transitions and symmetry-forbidden transitions. The former rule means that transition between states of different multiplicities are forbidden. The latter rule indicates that if the symmetry of one of the components of the electronic transition dipole moment is transformed following the same symmetry as the overall symmetry of the molecule, the transition is allowed. For octahedral transition metal complexes, for example, the symmetry selection rule prohibits d-d transitions whereas d-π^*, π-d and π-π^* transitions are usually encountered. These rules are very simple, however, not absolute laws but just

barometers for the intensities of specific transitions. A forbidden transition can occur but the intensity is always weak compared to that of the allowed transition.

2.2 Fate of Excited State

According to Born-Oppenheimer approximation, electronic motion is much more rapid than nuclear motion such as molecular vibration. Electronic excitation takes about 10^{-15}s (fs) while molecular vibration takes $10^{-10}\sim10^{-12}$s (ps). Therefore, we can assume that the electronic transition is likely to occur without changing nuclear positions. This is the Frank-Condon principle, the vertical transition.

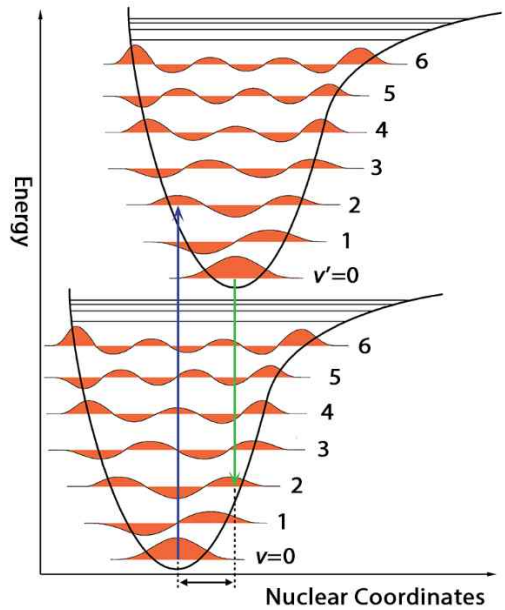

Figure 1. Electronic transition by the Franck-Condon principle

The excited state has normally the same spin multiplicity as the ground state, in the case of ruthenium(II) complex is singlet. Deactivation can take place in a radiative or non-radiative decay.

2.3 Diabatic and Adiabatic States

Electron transfer reactions involve the movement of an electron from the donor to the acceptor. Electron transfer can occur through space, through solvent or through bond. Through-space electron transfer occurs only over the short distance (< 0.5 nm) whereas through-covalent bond electron transfer may occur over much longer distances.

As in explaining vibration of diatomic molecule, the Hooke's law description, parabolic energy curve is also useful in discussion of the energy levels in more complicated molecules. In diagram, horizontal axis is nuclear coordinate which lumps together all the distances in all the bonds. Though the real picture would be a multidimensional representation, the two-dimensional parabola is used as a handy frame of reference for simplification. As mentioned earlier, electron transfer is vertical transition in the diagram. (the Franck-Condon principle) And conservation of energy requires that the transition should be horizontal line on the diagram. Therefore, electron jumping from the donor to the acceptor has to occur at intersection point of the two parabolas.

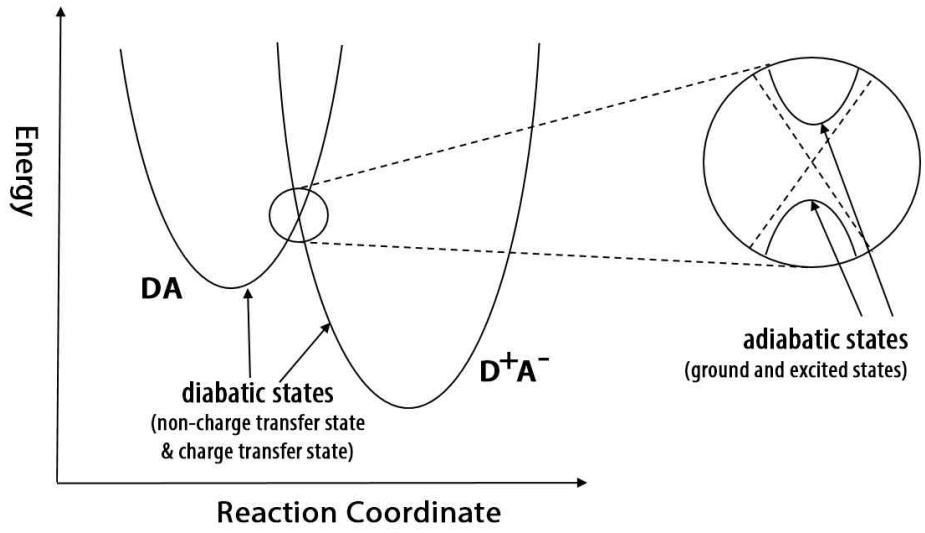

Figure 2. Potential energy surface for the diabatic and adiabatic states

In electron transfer theory, diabatic state is often used to describe the reactant and product states - the reactant state being the non-charge transfer state, ψ_{DA} where the electron is localized on the donor part (D) and the product state being the charge transfer state, ψ_{D+A-} in which the electron has been transferred to a spatially distinct acceptor region (A). These states give rise to the diabatic energy profiles depicted in left side of Figure 2. In diabatic states, electron transfer is a quantum jump from one curve to the other.

If the state ψ_{DA} and the state ψ_{D+A-} interact each other, the electron lingers at the barrier, and the curves representing the two states smooth to form a continuum as depicted in right side of Figure 2, with a quasi-state at the top of the activation barrier.

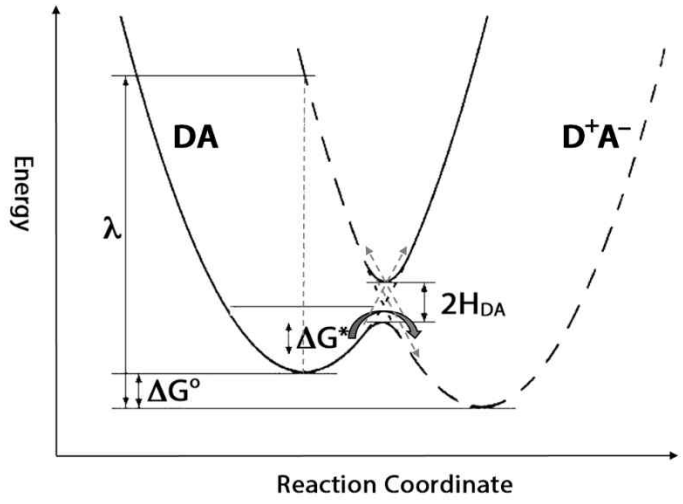

Figure 3. Potential energy surface for the adiabatic states, H_{DA} is the electronic coupling constant. The adiabatic electron transfer pathway is depicted by bold arrow and diabatic electron transfer pathway by dotted arrow.

It is occurring on a potential energy surface associated with a single electronic state. This is viewed in the adiabatic basis (ψ_{DA}, ψ_{D+A-}) obtained from the diabatic states and the degree of interaction between the two states is describe as the term, the electronic coupling matrix element, H_{DA} ($= \langle \psi_{DA} | H_{el} | \psi_{D+A-} \rangle$) where H_{el} is the system electronic Hamiltonian.

The splitting between the upper and lower adiabatic potential curves corresponds to twice the H_{DA} and the crossing is much easier for interacting systems. H_{DA} is predicted to decline exponentially with distance of the donor and the acceptor, because the electronic wavefunctions of the two states have exponential radial character.

2.4. Kinetics of Electron Transfer - The Marcus-Hush Analysis [7]

The Marcus-Hush theory is the most famous semi-classical electron transfer theory.

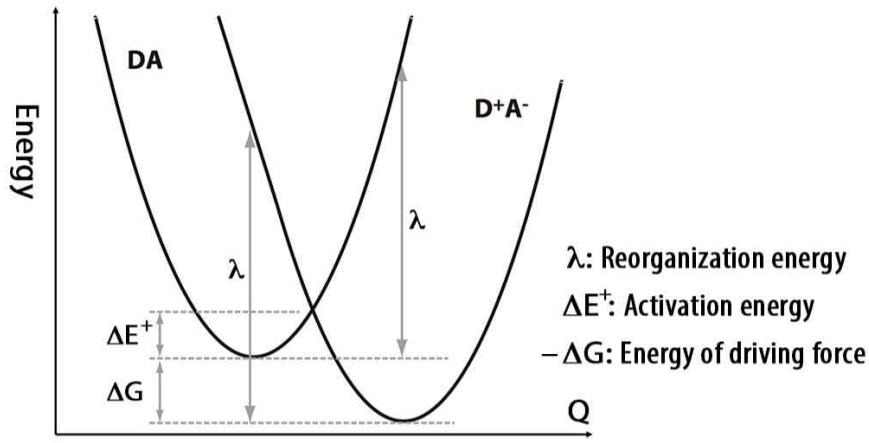

Figure 4. Marcus-Hush theory of electron transfer, electronic coupling is not shown for clarity

The reorganization energy, λ, is the energy it would take to force the reactants (on the left) to have the same nuclear configuration as the products (on the right) without letting the electron transfer. Q denotes the generalized reaction coordinate for the electron transfer reaction (a projection down from the 3N-6 molecular degrees of freedom, where N is the number of atoms in the system). The Marcus-Hush theory of electron transfer can be represented mathematically as follow

$$\Delta E^{+} = \frac{(\lambda+\Delta G)^2}{4\lambda}, \quad k_{ET} = |H_{DA}|^2 \sqrt{\frac{\pi}{h^2 k_B T \lambda}} exp\left\{-\frac{(\lambda+\Delta G)}{4k_B T}\right\} \qquad \text{(eq. 4)}$$

The major achievement of the Marcus-Hush relation is that it allows a semi-classical description of vibrational dynamics accompanying the electronic transition. Only a small number of parameters need to be considered, namely H_{DA}, λ and ΔG. These terms can be obtained experimentally or theoretically. Controllable change of H_{DA} and ΔG can be obtained by altering the structure of the complex.

There is an important relationship between λ and ΔG. According to eq. 4, the rate of electron transfer is exponentially dependent on the driving force plus reorganization energy squared in the exponent. This gives rise to three regimes of electron transfer as shown in Figure 5, below.

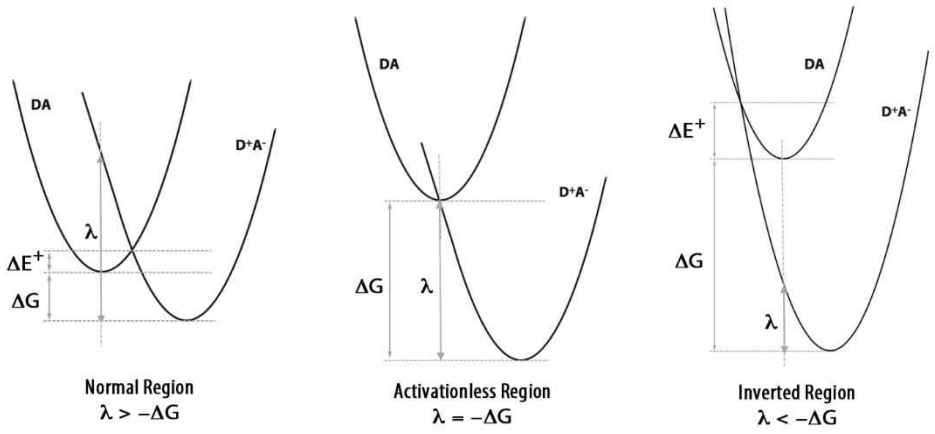

Figure 5. Three regimes for electron transfer with increasing driving force, $-\Delta G$.

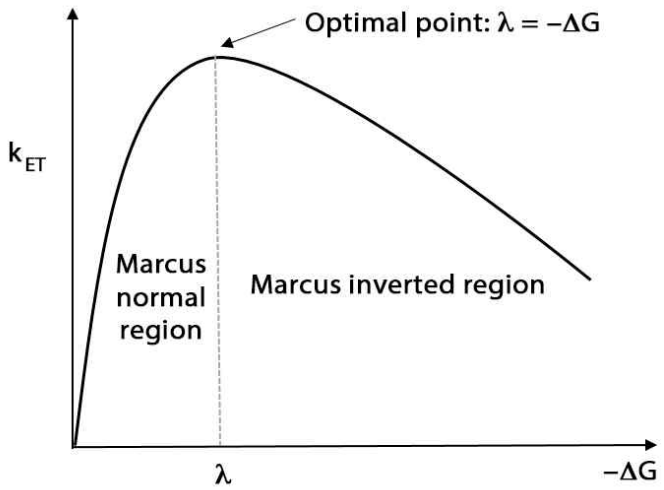

Figure 6. Electron transfer rate constants vs. driving force

Figure 6 shows how the rate of electron transfer depends on the driving force (here in terms of $-\Delta G$). The maximum is found when $-\Delta G$ is equal to the reorganization energy, λ. When the driving force becomes greater than the reorganization energy, we enter the Marcus inverted region. It is interesting to note that the inverted region was proposed by Marcus in the 1950's, but was not experimentally verified until the 1980s. Marcus won the Nobel Prize in Chemistry in 1992.

3. Bis(terpyridine) Ruthenium Complexes as Sensitizers.

3.1 Spectroscopic and Photophysical Properties of $[Ru(tpy)_2]^{2+}$

The UV-Vis spectra of transition metal complexes arises as a result of electronic transitions and the spectra that we see is the combination of the different types of transitions as they occur within the complex. Generally, octahedral metal complexes possess a center of symmetry. According to the symmetry selection rule, the center of symmetry is a necessary condition for a transition to be allowed that the electron moves from an orbital that is even with respect to inversion through the center of symmetry, to an orbital that is uneven with respect to inversion. Because all d orbitals in an octahedral complex are even with respect to inversion, d-d transitions are forbidden and so their intensities are very week. The relatively intense and broad absorption band in visible region (400~530 nm) is due to strong ^{1}d-π^* metal-to-ligand charge transfer transitions (MLCT), electron density can be transferred from d or n orbitals localized on the metal ion to a π^* orbital on the ligand.

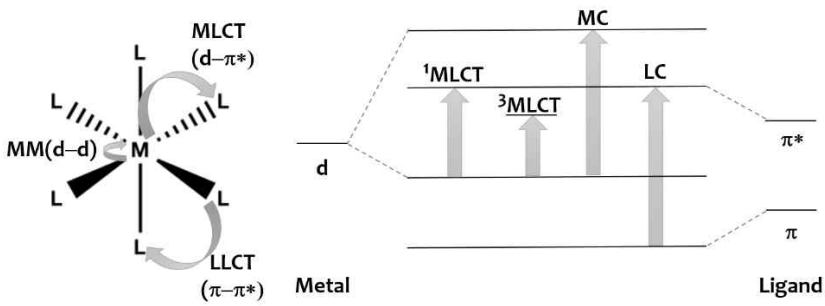

Figure 7. Charge transfer in octahedral metal complex

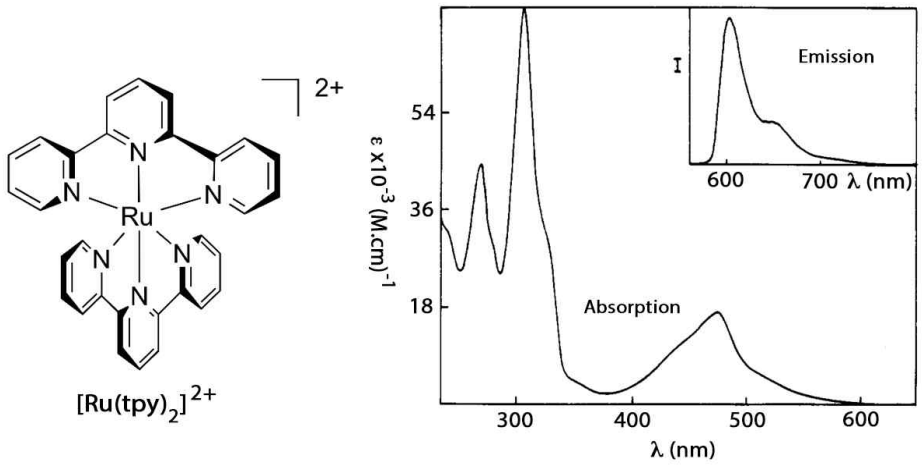

Figure 8. Structure and absorption spectrum of $[Ru(tpy)_2]^{2+}$ in acetonitrile solution at room temperature (The spectrum in inset is luminescence at 77 K)

Ruthenium(II) complexes don't exhibit ^{3}d-π^* transition is forbidden by the selection rule. The energy level of MLCT state is dependent on both the oxidation potential of the metal ion and the reduction potential mainly originated from a ligand. Very intense bands in the UV region (< 350 nm) are assigned to ligand-centered $\pi - \pi^*$ transitions.

Unlike $[Ru(bpy)_3]^{2+}$, bis(tridentate) complex, $[Ru(tpy)_2]^{2+}$ is not emissive at room temperature, but emissive only at low temperature. This emission is characteristic of triplet metal-to-ligand charge transfer state (^{3}MLCT) level. This anomalously weak emission at room temperature was explained that the unfavorable bite angles associated terpyridine ligand result in a relatively weak ligand field such that low-lying MC states are available to quench the luminescent ^{3}MLCT state.[7]

3.2 Redox Properties of $[Ru(tpy)_2]^{2+}$ and Its Analogues with Ru-C Bond

The $[Ru(tpy)_2]^{2+}$ type complexes are electrochemically active and undergo a reversible $Ru^{II/III}$oxidation and a reversible ligand-centered reduction. Equations below represent the oxidation and the reduction process, respectively.

$$[Ru^{II}(LLL)_2]^{2+} \rightarrow [Ru^{III}(LLL)_2]^{3+} + e^-$$

$$[Ru^{II}(LLL)_2]^{2+} + e^- \rightarrow [Ru^{II}(LLL)(LLL^-)]^+$$

Table 1. Cyclic voltametric data for bis(tridentate) Ru(II) complexes

	1	2[6(a)]	3[6(d)]
$E_{1/2}$ (V) of $Ru^{II/III}$	+1.55	+0.81	+1.46
$E_{1/2}$ (V) of $L/L^{\bullet -}$	-0.99	-1.30	-1.07

Potentials reported relative vs ferrocene/ferrocenium (Fc/Fc^+) used as an internal standard and converted to NHE by the relation ferrocene/ferrocenium vs. NHE = +0.64 V.

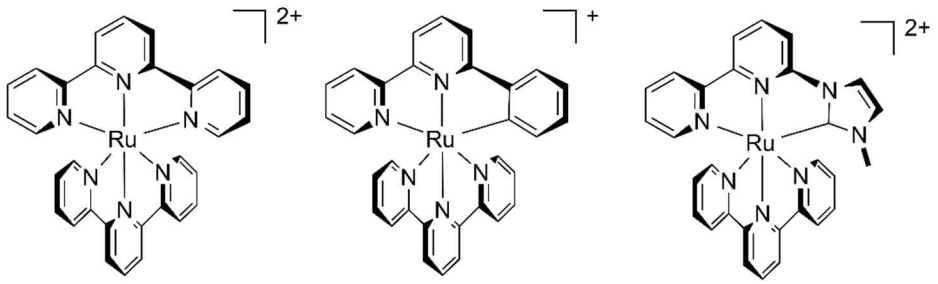

Figure 9. $[Ru(tpy)_2]^{2+}$ and Ru(II) complex with Ru-C bond.

The half-wave oxidation and reduction potentials for $[Ru(tpy)_2]^{2+}$ and heteroleptic bis(tridentate) Ru(II) complexes are summarized in Table 1. In comparison to neutral nitrogen atom based on terpyridine, the cyclometalated NNC type complex (2) caused cathodic shift of about 0.7 V for the metal based oxidation.[6(a)] Due to the strong electron donor ligand, the more electron-rich metal center increases back-donation to ligand and accordingly shifts the ligand-based reduction to more negative potentials. Albeit to a lesser extent, complexes with *N*-heterocyclic carbene ligand show a similar tendency.[6(b)-(d)]

3.3 $[Ru(tpy)_2]^{2+}$ as Artificial Photosynthetic Molecular Devices (PMD)

On the basis of photochemical, photophysical and electrochemical properties, Ru(II) complexes with 2,2'-bipyridine are the best photosensitizers and used as artificial photochemical molecular devices based on photoinduced charge separation or energy migration. For example, the triad system shown in Figure 9 was studied by Hammarström and co-workers.[9(a)] This system is based on benzoquinone (Q) as an electron acceptor, phenothiazine (PTZ) as an electron donor and $Ru(bpy)_3$ acting as a chromophore. The PTZ^+-Ru^{2+}-BQ^- charge-separated state is formed via sequential electron transfer steps of Ru^{2+} to BQ and PTZ to Ru^{3+}.

However, octahedral metal complexes containing 2,2'-bipyridine type ligands exist enantiomers by the nature of bidentate ligand. Moreover, a functional group substituted bidentate ligand can cause various stereoisomers. In contrast to behavior

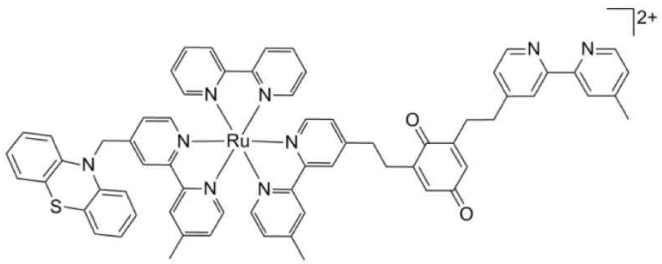

Figure 9. $[Ru(bpy)(bpy\text{-}PTZ)(bpy\text{-}Q)]^{2+}$ synthesized by Hammarström et al.

of bipyridine, six coordinated $Ru(tpy)_2$ type complexes exist as achiral, symmetric complex. Even introducing a substituent (electron donating or accepting group) in the 4' position of terpyridine makes no additional problems. When electron donor and electron acceptor components are anchored to 4' position of tpy, the symmetry of complex is retained and it is convenient way to control the separation distance of D and A. Because of its geometry, tpy is a good candidate to artificial photosynthetic molecular devices.

3.4 Quinone as an Electron Acceptor

Quinones are extensively used as electron acceptors in mimicking natural photosynthetic system since they play a pivotal role in natural photosynthesis.[10] The extraordinary character of quinone comes from low lying unoccupied orbitals which are ready for accepting electrons and the ability to form hydrogen bond. Some groups synthesized porphyrin-quinone dyad molecules linked by linear carotenoid polyene

or cofacially π-stacked bridge which were found to carry out photo-driven electron transfer.

There also have been a number of researches involving ruthenium complexes containing a quinone moiety. These systems were developed to examine intramolecular electron transfer which is necessary characteristic in the design of artificial photosynthetic device. Schanze and Sauer studied electron transfer rates in Ru(II) complexes which a metal center acting as a donor is separated from the acceptor, *p*-benzoquinone by oligo(L-proline) spacers[9(b)] (Figure 10). As the distance from ruthenium to quinone increased, the rate of electron transfer was seen to decrease.

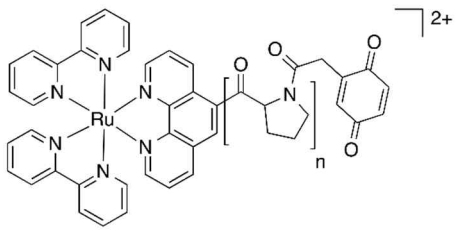

Figure 10. Ruthenium-Quinone complex synthesized by Schanze and Sauer

David A. Modarelli synthesized ruthenium(II) and osmium(II) bis(terpyridine) donor acceptor dyad and used benzoquinone (BQ) and a substituted pyromellitimide (PI) as the electron acceptors.[9(c)] They estimated the rates of electron transfer by combination of femtosecond and nanosecond transient absorption and time-resolved spectroscopy experiments. Charge separation was found only in Ru(II)-BQ and occurred on the picosecond time-scale. The rates of charge separation and charge

recombination was strongly dependent on the number of phenyl ring and it was attributed to the decreased electronic coupling of donor and acceptor caused by additional barrier.

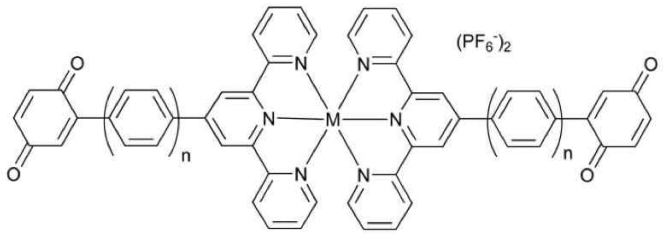

Figure 11. M(tpy-(ph)$_n$-Q)$_2$ complexes (M = Ru, Os) synthesized by Modarelli

4. Dissertion Overview

Although a number of metal complexes containing symmetric 4' position functionalized 2,2',6',2"-terpyridine have been prepared and characterized, little is known about a complex with unsymmetric terpyridine. Up to date, most electron transfer studies were conducted with a long donor-acceptor distance. Because the electronic coupling is strongly dependent on the distance between the donor and the acceptor, so we decided to research the intramolecular electron transfer system which the acceptor is very close to the donor and synthesized all new designed Ru(II) complexes.

In section 1 of part I, we have newly synthesized unsymmetric 6-benzoquinonyl-2,2',6',2"-terpyridine based Ru(II) complexes for investigating intramolecular electron transfer. Interestingly, the quinone ring was placed on central pyridyl ring of another terpyridine with cofacially π-stacked and therefore the distance of the electron acceptor quinone from ruthenium was only less than 5 Å. When the electron transfer occurred to quinone, the vibrational frequency of the characteristic carbonyl group changed instantly. With the aid of an ultrafast visible-pump/mid-IR-probe spectroscopic method, the degree of the electronic coupling and the kinetics of electron transfer were studied.

In the work of section 1 of part I, electron transfer to quinone was observed but we couldn't confirm the electron transfer pathway. In section 2 of part I, in order to discover the electron transfer pathway, we changed the combination of ligands from tpy and tpy-Q to tpy and NHC-Q introducing the new tridentate ligand with *N*-

heterocyclic carbene moiety. Due to strong electron donating power of carbene ligand, unidirectional electron transfer was caused and the photoinduced charge separation was proved to take place via π-stacked manifold of van der Waals contact, not through covalent bond. Detailed kinetics of charge separation, charge recombination and vibrational cooling in ground state were also studied minutely by analyzing transient IR absorption spectrum and calculating the vibrational frequencies of both ground and CS states by time-dependent density functional theory.

Recently, *N*-heterocyclic carbene (NHC) ligands have become universal in organometallic and inorganic chemistry. However, their photophysical and chemical properties in their ruthenium complexes have been relatively less well studied. Several years ago, we reported the synthesis of a handful of the Ru(II)-NHC complexes based on bip ligand (bip = 2,6-bis-(3-methylimidazolium-1-yl) pyridine) which has two imidazolium carbene units. Due to multiple number of carbene in bip ligand, redox potentials and light absorbing property differ greatly from well known chromophore, Ru(II) polypyridyl complexes. In part II, for fine tuning of various properties of the complex and investigating the effect of single NHC unit, we synthesized a series of seven Ru(II) complexes bearing unsymmetric NHC ligands which has one carbene. (NNC or NN^C type) The electronic structures of these complexes were analyzed by spectroscopic and electrochemical methods and further examined by theoretical calculations.

5. Reference

(1) (a) D. C. Arnett, C. C. Moser, P. L. Dutton and N. F. Scherer, *J. Phys. Chem*. B, **1999**, *103*, 2014–2032; (b) T. Pullerits and V. Sundstrom, *Acc. Chem. Res*. **1996**, *29*, 381-389.

(2) (a) V. K. Yachandra, K. Sauer and M. P. Klein, *Chem. Rev*. **1996**, *96*, 2927–2950; (b) W. Ruttinger and G. C. Dismukes, *Chem. Rev*. **1997**, *97*, 1–24; (c) R. J. Debus, *Biochim. Biophys. Acta*, 1992, **1102**, 269-352.

(3) (a) Flamigni, L.; Baranoff, E.; Collin, J. P.; Sauvage, J. P., *Chem. Eur. J.* **2006,** *12*, 6592. (b) Opperman, K. A.; Mecklenburg, S. L.; Meyer, T. J., *Inorg. Chem.* **1994,** *33*, 5295. (c) McCafferty, D. G.; Friesen, D. A.; Danielson, E.; Wall, C. G.; Saderholm, M. J.; Erickson, B. W.; Meyer, T. J., *Proc. Natl. Acad. Sci. U.S.A.* **1996,** *93*, 8200.

(4) (a) E. Baranoff, J.-P. Collin, L. Flamigni and J. P. Sauvage, *Chem. Soc. Rev*. **2004**, *33*, 147-155. (b) A. Harriman, M. Hissler, A. Khatyr and R. Ziessel, *Eur. J. Inorg. Chem.*, **2003**, 955-959.

(5) (a) V. Balzani and A. Juris, *Coord. Chem. Rev*., **2001**, *211*, 97. (b) E. C. Constable, *Chem. Commun.* **1997**, 1073. (c) E. C. Constable, E. L. Dunphy, C. E. Housecroft, W. Kylberg, M. Neuburger, S. Schaffner, E. R. Schofield and C. B. Smith, *Chem. Eur. J*. **2006**, *12*, 4600-4610.

(6) (a) S. H. Wadman, M. Lutz, D. M. Tooke, A. L. Spek, F. hartl, R. W. A. Havenith, G. P. M. van Klink and G. van Koten, *Inorg. Chem*. **2009**, *48*,

1887-1990. (b) Son, S. U.; Park, K. H.; Lee, Y. S.; Kim, B. Y.; Choi, C. H.; Lah, M. S.; Jang, Y. H.; Jang, D. J.; Chung, Y. K. *Inorg. Chem.* **2004**, *43*, 6896– 6898. (c) H. J. Park, K. H. Kim, S. Y. Choi, H. M. Kim, W. I. Lee, Y. K. Kang and Y. K. Chung, *Inorg. Chem*. **2010**, *49*, 7340-7352. (d) in Press, Part II of this Thesis.

(7) Turro, N. J. Modern Molecular Photochemistry; University Science Books, Sausalito, CA: 1991.; Newton, M. D. "Quantum Chemical Probes of Ele ctron-Transfer Kinetics - the Nature of Donor-Acceptor Interactions", *Chem. Rev*. **1991**, *91*, 767-792.

(8) (a) Winkler, J. R.; Netzel, T. L.; Creutz, C.; Sutin, N. *J. Am. Chem. Soc.* **1987**, *109*, 2381. (b) Coe, B. J.; Thompson, B. W.; Culbertson, C. D.; Shoonover, J. R.; Meyer, T. J. *Inorg. Chem.* **1995**, *34*, 3385. (c) Clark, R. H.; Ann, K. I. G.; David, R. M. *Inorg. Chem.* **1991**, *30*, 538..

(9) (a) Kumar, R. J.; Karlsson, S.; Streich, D.; Jensen, A. R.; Jager, M.; Becker, H. C.; Bergquist, J.; Johansson, O.; Hammarström, L., *Chem. Eur. J.* **2010,** *16*, 2830. (b) K. S. Schanze, K. Sauer, *J. Am. Chem. Soc.* **1988**, *110,* 1180. (c) Elvin A. Aleman, Carol D. Shreiner, Cheruvallil S. Rajesh, Timothy Smith, Shana A. Garrison, David A. Modarelli. *Dalton Trans*. **2009**, *33*, 6562-6577.

(10) (a) Gunner, M. R.; Dutton, P. L., *J. Am. Chem. Soc.* **1989,** *111*, 3400. (b) Renger, G. *Angew. Chem.Int. Ed. Engl.* **1987,** *26*, 643. (c) Gupta, N.; Linschitz, H., *J. Am. Chem. Soc.* **1997,** *119*, 6384.

Part I.

Manipulation Photoinduced Electron Transfer in Rigid, Cofacially Aligned π-Stacked Ruthenium(II)-Bridge-Quinone Systems

Section 1.

Probing Ground-to-CT State Electronic Coupling for the System with No Apparent Charge Transfer Absorption Intensity by Ultrafast Visible-Pump/Mid-IR-Probe Spectroscopy

1. Introduction

The theoretical background to quantify an electronic coupling matrix element (H_{DA}) between the ground and the charge transfer (CT) states by optical CT absorption intensity had been first established by Mulliken and Hush and later expanded on by a number of scientists. [1-4] While close evaluation of H_{DA} by either an experimentally determined transition dipole moment (μ) of a CT absorption band[5-18] or a pure computational calculation through generalized Mulliken-Hush analysis[19-22] was made possible, Rubtsov et al. reported[23] an interesting result that provides a protocol to determine H_{DA} by a femtosecond visible-pump/mid-IR-probe spectroscopy (TrIR).

If adiabatic ground (Ψ_G) and CT (Ψ_{CT}) state wavefunctions are expressed as following equations,[24]

$$\Psi_G = C_1\psi_1 + C_2\psi_2 \qquad \text{(eq. 1a)}$$

$$\Psi_{CT} = C_1\psi_2 - C_2\psi_1 \qquad \text{(eq. 1b)}$$

where ψ_1 and ψ_2 are wavefunctions of zero-order ground and CT states,[4] respectively, a first order perturbation theory[4] predicts that

$$|C_1C_2| = |H_{DA}/\Delta E| \qquad \text{(eq.2)}$$

where ΔE is the ground-to-CS state energy gap. As the interaction between ψ_1 and ψ_2 increases, the magnitude of C_2 increases; the degree of CT character in the ground state or that of ground state character in the CT state scales with C_2^2. For a D-A molecule where A is Q, the vibrational frequency shift of the carbonyl stretching mode in the CT state relative to that in the ground state ($\Delta\nu_Q$) depends on the charge

built into the Q moiety. The linear correlation between $\Delta\nu_Q$ and the degree of charge built on the corresponding radical anion has been determined empirically by Rubtsov et al.[23] as $\xi \approx 2C_2^2$, where $\xi = (\Delta\nu_Q^\circ - \Delta\nu_Q)/\Delta\nu_Q^\circ$ and $\Delta\nu_Q^\circ$ is the $\Delta\nu_Q$ of the system with no D-A interaction.[6,25] From this relation along with eq.2, H_{DA} can be recast in the form of eq. 3 and becomes available if two parameters, ξ and ΔE, are known.

$$H_{DA} = \left|\Delta E\sqrt{\left(1-\frac{\xi}{2}\right)\frac{\xi}{2}}\right| \qquad \text{(eq. 3)}$$

The ξ can be obtained by TrIR with proper $\Delta\nu_a^\circ$ and ΔE values; $\Delta\nu_a^\circ$ can be determined by measuring the vibational frequency difference between the ground (ν_a°) and the reduced state (ν_a-$^\circ$) of the electron acceptor while ΔE can be obtained by conventional electrochemical methods.[26]

While Mulliken-Hush analysis has been a widely accepted protocol for the evaluation of H_{DA}, its application to a variety of real systems is limited because CT absorption band is only observable when H_{DA} is sufficiently large to reach or surpass a perturbation limit in most real systems, although the Mulliken-Hush relation is assumed to be valid only in the weak coupling limit.[4,8,16] Moreover, even if a CT absorption band is available, an accurate quantification of H_{DA} is often obscured by interference when the CT state overlaps energetically with other states or there is a significant degree of mixing between the CT state and others. Therefore, the evaluation of H_{DA} by eq. 2 through the TrIR approach is particularly useful for a system that does not exhibit distinguishable CT absorption.

2. Result and Discussion

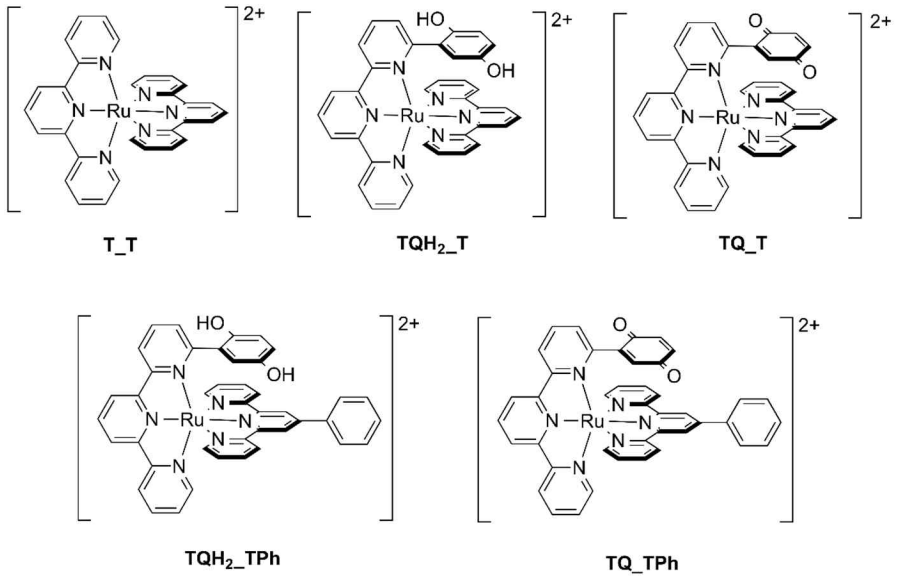

Chart 1. Structures of $[Ru(tpy)_2]^{2+}$-Q (**TQ_T**) and $[Ru(tpy)(tpyPh)]^{2+}$-Q (**TQ_TPh**) along with $[Ru(tpy)_2]^{2+}$ (**T_T**).

During our ongoing effort to develop a Ru-based chromophore system that absorbs the light over a wide range of the energy window, we have newly synthesized [Ru(6-(2-cyclohexa-2',5'-diene-1,4-dione)- 2,2':6',2"-terpyridine)(2,2':6',2"-terpyridine)] $[PF_6]_2$ (**TQ_T**), [Ru(6-(2-cyclohexa-2',5'-diene-1,4-dione)-2,2':6',2"-terpyridine) (4'-phenyl-2,2':6',2"-terpyridine)][PF_6]$_2$ (**TQ_TPh**), in which a benzoquinone (Q) electron acceptor is located on top of the central pyridyl ring of a tpy ligand in a juxtaposed manner (Chart 1). The proximal location of the electron acceptor near the electron donor Ru metal was expected to give rise to an orbital interaction between Ru-centered HOMO and Q-centered LUMO, which might generate a metal-to-Q CT (MQCT) band in the lower energy region relative to the already existing metal-to-tpy

CT band (MLCT). This feature would facilitate a light harvesting over a wide range of the energy window. Contrary to our anticipation, however, the absorption spectra of **TQ_T** and **TQ_TPh** complexes resembled those of a **T_T** archetype exhibiting only conventional MLCT bands. MQCT absorption did not prevail. The mere absence of a MQCT absorption band is not surprising if ground-to-MQCT H_{DA} is not large.[27-29] Interestingly, however, further investigation by the TrIR spectroscopic method revealed that the H_{DA} was nonetheless substantial. Here we report the details of these results, which clearly demonstrate the usefulness of TrIR in determining the magnitude of H_{DA} where the CT absorption intensity is negligible.

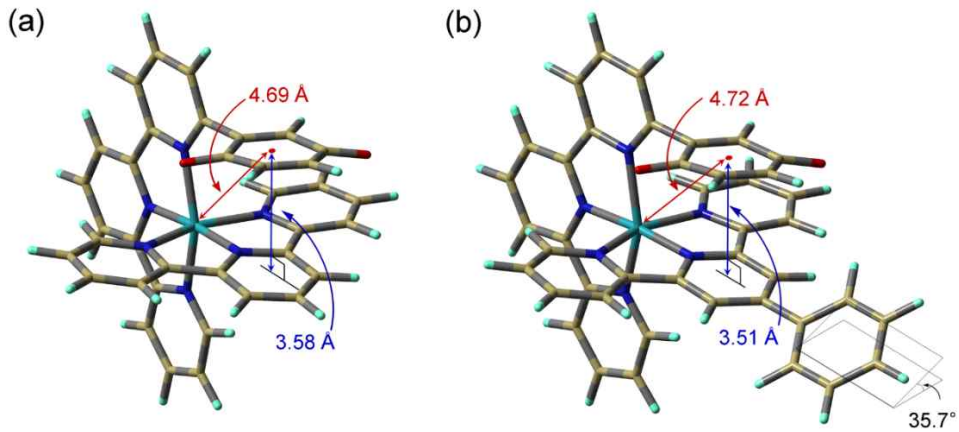

Figure 1. Geometries of **TQ_T** (a) and **TQ_TPh** (b). Metal-to-quinonyl plane centroid distances are shown in red. Quinonyl plane-to-pyridyl plane distances are shown in blue.

The **TQ_T** and **TQ_TPh** complexes were synthesized by a conventional synthetic protocol, which is summarized in Scheme 1. These complexes were fully

characterized by a series of 1D and 2D NMR studies, high-resolution mass spectroscopy, and electronic and vibrational spectroscopies. Optimized geometries by DFT calculation at B3LYP/6-31g(d)-LANL2DZ level show that the Q plane is orthogonally attached to the 6-position of one tpy ligand and is nearly coplanar with a juxtaposed pyridyl ring plane in another tpy ligand for both **TQ_T** and **TQ_TPh**. Ru-to-Q centroid distances are 4.69 and 4.72 Å for **TQ_T** and **TQ_TPh**, respectively (Figure 1). Q plane-to-pyridyl plane distances are 3.58 and 3.51 Å, respectively, indicating that the Q and pyridyl ring planes are in typical van der Waals distance for both **TQ_T** and **TQ_TPh**. Due to this π-stacking, ^{1}H-NMR peaks corresponding to quinonyl protons appear at 5.56, 6.41, and 6.68 ppm for **TQ_T** and 5.63, 6.45, and 6.52 for **TQ_TPh**, which are ~1 ppm upfield shifted relative to those of a conventional Q. However, the degree of compression between Q and tpy is only moderate compared to that of the cofacially aligned porphyrin-Q system reported previously by the Therien group.[50,51] The optimized geometry of **TQ_TPh** shows that the dihedral angle between the peripheral phenyl substituent at the 4'-position and the central pyridyl ring is ~36°.

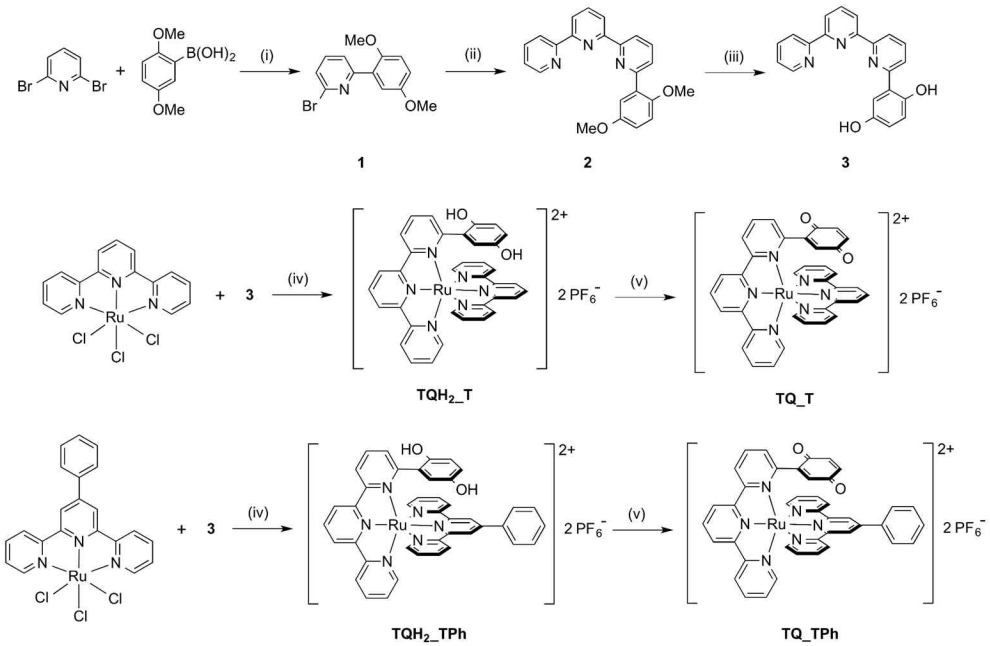

Scheme 1. Synthesis of **TQ_T** and **TQ_TPh**.

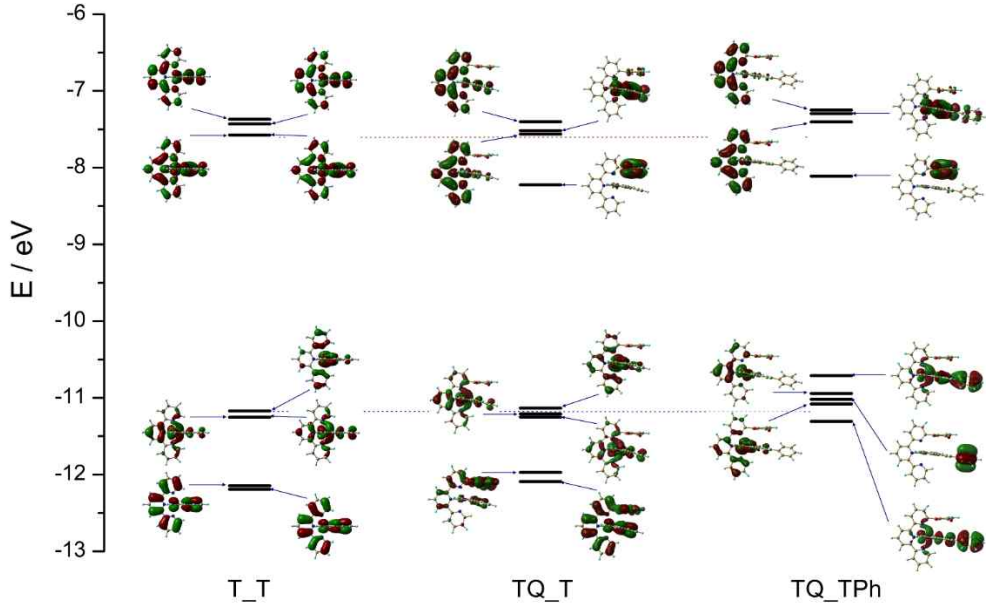

Figure 2. Energies and 3-dimensional representations of frontier molecular orbital (five highest occupied and four lowest unoccupied) diagram of $[Ru(tpy)_2]^{2+}$ (**T_T**), **TQ_T**, and **TQ_TPh** calculated at the B3LYP/LANL2DZ level. HOMO and LUMO energy level of **T_T** are guided by blue and red dotted lines, respectively.

Table 1. Energies and Percent Compositions of Frontier MOs of **TQ_T**, and **TQ_TPh**.

TQ_T						**TQ_TPh**					
MO		Electron Population (%)				MO		Electron Population (%)			
No.	E (eV)	Ru	Tpy1[a]	Tpy2[b]	Q	No.	E (eV)	Ru	PhTpy[c]	Tpy[d]	Q
3[e] (159)	-7.52	8.4	82.9	5.9	2.8	3[e] (179)	-7.30	7.8	86.6	3.8	1.8
2[e] (158)	-7.57	8.0	7.8	83.6	0.5	2[e] (178)	-7.41	8.6	4.5	86.2	0.7
1[e] (157)	-8.23	0.5	3.9	2.5	93.2	1[e] (177)	-8.12	0.3	4.0	2.4	93.3
0[e] (156)	-11.15	74.6	13.2	12.0	0.1	0[e] (176)	-10.72	42.5	50.6	6.8	0.1
-1[e] (155)	-11.22	73.7	12.9	13.2	0.3	-1[e] (175)	-10.96	74.3	13.6	12.0	0.1
-2[e] (154)	-11.27	74.9	13.6	11.3	0.2	-2[e] (174)	-11.03	74.8	11.7	13.2	0.3
-3[e] (153)	-11.99	0.2	5.1	8.7	86.0	-3[e] (173)	-11.10	0.2	99.3	0.1	0.5
-4[e] (152)	-12.11	0.1	30.3	38.3	31.3	-4[e] (172)	-11.32	45.9	47.2	6.6	0.3

[a]Tpy ligand coplanar to Q. [b] Tpy ligand where Q is attached. [c]4'-phenyl-tpy ligand. [d]Tpy-CO_2H ligand. [e]0 and 1 indicate HOMO and LUMO, respectively. –1. –2, ..., -4 correspond to HOMO-1, HOMO-2, …, HOMO-4, respectively while 2 and 3 represent LUMO+1 and LUMO+2, respectively

Table 2. Spectroscopic and Voltammetric Data.

Complex	λ_{max}[a]		ε	ν_{CO}	$E_{1/2}^{ox, b}$	$E_{1/2}^{red, b}$
	nm	cm^{-1}	$\times 10^4$ $M^{-1}cm^{-1}$	cm^{-1}	V vs NHE	
TQH_2_T	472	21,186	1.40			
TQ_T	473	21,142	1.34	1661	1.64	-0.02
TQH_2_TPh	482	20,747	2.06			
TQ_TPh	478	20,921	1.91	1661	1.62	0.01

[a]Experimental conditions: solvent = acetonitrile, temperature = 23 °C. [b]Experimental conditions: [compound] = 5 mM; [$TBAPF_6$] = 0.1 M; solvent = acetonitrile; temperature = 23 °C; scan rate = 50 mV/s; reference electrode = Ag/Ag^+; working electrode = glassy carbon. All potentials are referenced to a ferrocene/ferrocenium redox couple as an internal standard and converted to NHE by the relation ferrocene/ferrocenium vs NHE = +0.64 V.

The electrochemical redox potentials of the two complexes in acetonitrile were recorded and their values are listed in Table 2. Both complexes exhibit one electron reversible oxidation at 1.64 and 1.62 V and one electron reversible reduction at –0.02 and 0.01 V for **TQ_T** and **TQ_TPh**, respectively.[52] The energies and 3-dimensional isosurfaces of the frontier MOs of **TQ_T** (Figure 2, Table 1) obtained by DFT calculation show that HOMO is mainly localized in Ru metal (74.6 %) while LUMO is in Q (93.2 %). In the case of **TQ_TPh**, however, the electronic population in HOMO is delocalized over the phenyl-tpy ligand (50.6%) as well as Ru metal (42.5 %)

while that in LUMO is localized in Q (93.3%). Consequently, the energy level of HOMO in **TQ_TPh** was significantly destabilized by 0.43 eV relative to that in **TQ_T**. This calculation result is, however, obviously contradictory to the experimental results. The oxidation potentials of two complexes measured by cyclic voltammetry were nearly identical to each other. This discrepancy might be due to the overemphasized coplanarity in the calculated structure. The optimized geometry of **TQ_TPh** shows that the dihedral angle between the peripheral phenyl substituent at the 4'-position of the tpy ligand and the central pyridyl ring was only ~36°. In solution phase, the electronic delocalization effect should decrease due to the rotational degree of freedom. Single point calculation with the orthogonally fixed dihedral angle gives rise to a destabilization of the HOMO of **TQ_TPh** by 0.26 eV while that with the 30° does 0.81 eV, which indicates that the origin of the destabilization of the energy level of HOMO in **TQ_TPh** can be mainly ascribed to the electronic delocalization.

It is important to note that the slightly different electronic structures of **TQ_T** and **TQ_TPh** do not manifest in the electronic absorption spectra. The absorption spectra of two complexes are nearly identical except for the existence of a small shoulder at the ~520 nm region in the spectrum of **TQ_TPh** (Figure 3a). The absorption spectra of **TQ_T** and **TQH$_2$_T,** in which Q in **TQ_T** was replaced with hydroquinone (**QH$_2$**) and thus CT transition is not allowed, were also virtually identical to each other. Figure 3b shows the normalized electronic absorption profile of two complexes.

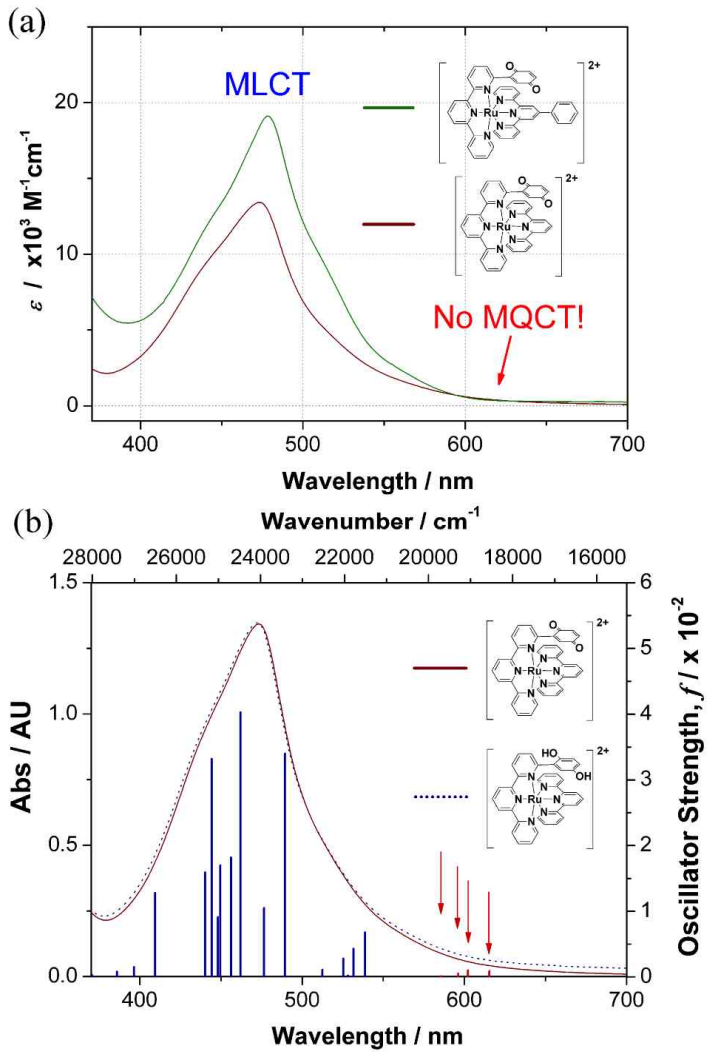

Figure 3. (a) Steady state absorption spectra of **TQ_T** (red), **TQ_TPh** (blue), and **T_TPh$_2$Q** (black) in CH_3CN at 25 °C. (b) Normalized absorption spectra of **TQ_T** (solid red) and its hydroquinone analogue, **TQH$_2$_T** (dotted blue), in wavelength (bottom abscissa). Calculated transition energies and their corresponding oscillator strengths, *f*, of singlet → singlet transitions by TD-DFT method are depicted as vertical lines in wavenumber (top abscissa). Red lines emphasized by red arrows near 600 nm are MQCT transitions. Note that the abscissa on top was shifted by 1000 cm^{-1}.

Table 3. Compositions of the CT-state wave functions of **TQ_T** and **TQ_TPh** in terms of the linear combination coefficients in the configuration expansion.[a]

State[b]	Energy		f[c]	Wavefunction	Character	Transition Dipole Moment		
	eV	cm^{-1}				au		
TQ_T								
						x	y	z
S1	2.300	18550	0.0009	0.6913 $\Psi_{0\to1}$	MQCT	-0.1062	-0.0498	-0.0528
S2	2.364	19065	0.0010	0.2519 $\Psi_{-2\to1}$ + 0.6484 $\Psi_{-1\to1}$	MQCT	-0.1290	0.0379	0.0018
S3	2.393	19297	0.0005	-0.2669 $\Psi_{-3\to1}$ + 0.5923 $\Psi_{-2\to1}$ - 0.2212 $\Psi_{-1\to1}$	MQCT + π–π^*	-0.0598	0.0721	0.0005
S4	2.443	19704	0.0001	-0.2222 $\Psi_{-4\to1}$ + 0.5699 $\Psi_{-3\to1}$ + 0.2730 $\Psi_{2\to1}$	MQCT + π–π^* + LQCT	-0.0247	0.0320	0.0255
TQ_TPh								
						x	y	z
S1	2.023	16314	0.0007	0.7012 $\Psi_{0\to1}$	MQCT + LQCT	-0.1143	0.0360	0.0195
S2	2.239	18057	0.0005	0.6960 $\Psi_{-1\to1}$	MQCT	-0.0087	0.0915	-0.0367
S3	2.311	18643	0.0003	0.6919 $\Psi_{-2\to1}$ - 0.1022 $\Psi_{-1\to1}$	MQCT	0.0402	0.0527	-0.0191
S5	2.509	20236	0.0001	0.1774 $\Psi_{-6\to1}$ + 0.1142 $\Psi_{-5\to1}$ + 0.6665 $\Psi_{-3\to1}$	LQCT + π–π^* + LQCT	-0.0179	-0.0377	0.0161
S8	2.645	21337	0.0031	0.6103 $\Psi_{-4\to1}$ - 0.1248 $\Psi_{-2\to2}$ - 0.2944 $\Psi_{-1\to2}$	MQCT + MLCT + LQCT	-0.1466	0.1600	0.0068

[a]Subscripts correspond to the following orbitals: The highest occupied orbitals have index 0, i.e. 0 = HOMO, while all other occupied orbitals have index –1. –2. …, -*n*, which correspond to HOMO-1, HOMO-2, …, HOMO-*n*, respectively. LUMO = 1, LUMO+1 = 2, LUMO+2 = 3, and so on. [b]State numbers obtained from the calculation. [c]Oscillator strength.

These results suggest that both **TQ_T** and **TQ_TPh** exhibit only the MLCT transition without possessing MQCT character. In order to elucidate the nature of the electronic transitions of the absorption spectra further, we performed the TD-DFT calculation. For each complex, we considered thirty singlet excited states. Transitions that have oscillator strengths larger than 0.001 are listed in Table 3. To compensate the energy offset between the experimental and the calculation results, 1000 cm^{-1} was equally added to the calculation results and co-plotted with the experimentally

obtained results (Figure 3b). The calculation result mirrors well the experimental observations. It predicts four ground-to-MQCT transitions (S1-S4 states, Table 3) for **TQ_T** near 19000 cm^{-1} with combined oscillator strength (*f*) of only 0.0024. The same is true for **TQ_TPh** in that the total *f* of four predicted ground-to-MQCT transitions is only 0.0015 (S1-S3, and S5 states, Table 3). It should be noted that S8 state of **TQ_TPh** has a large 4'-phenylterpyridine-to-Q CT (LQCT) character in addition to MQCT and MLCT characters. The S4 state of **TQ_T** also has such a character but its oscillator strength is negligible (0.0001) and thus would not contribute to the spectral envelope. Oscillator strength of S8 state of **TQ_TPh** is, however, 0.0031, which cannot be ignored. The S8 state is a result of mixing among MLCT, LQCT and MQCT. The electronic transition to this state contributes the shoulder in the spectral envelope near 520 nm, which was noted earlier. Despite the existence of such a band that possesses a high degree of MQCT character, Mulliken-Hush analysis cannot be easily performed because not only is the character of the state the result of a high degree of mixing among different types of transitions but it also overlaps with other states. These results clearly show that MQCT transitions in these complexes are, if any, not available for the Mulliken-Hush analysis and thus probing H_{DA} through such an approach is not feasible.

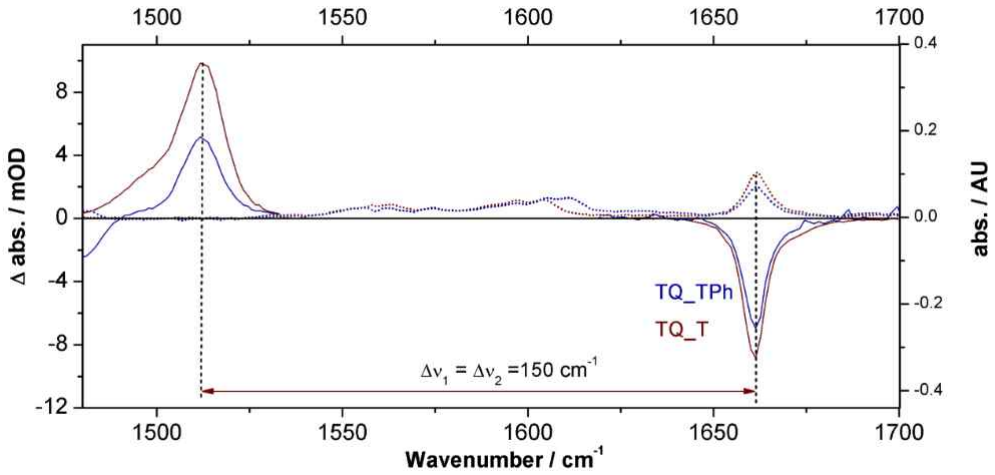

Figure 4. TrIR spectra of **TQ_T** (solid red), **TQ_TPh** (solid blue), and **T_TPh$_2$Q** (solid green) at time delays of 1.8, 1.8, and 10 ps, respectively. FTIR spectra are shown in dotted lines with corresponding colors. Note that TrIR spectra of 1530-1620 cm^{-1} region are not shown. (Experimental conditions: λ_{ex} = 575 nm, solvent = CD_3CN. Temp = 23 ± 1 °C).

Table 4. Ground (ν_Q) and CT (ν_Q^-) state CO stretching frequencies along with absolute ($\Delta\nu_Q$) and relative (ξ) frequency differences, ground-state Mulliken population of acceptor (q_Q), and electronic coupling between G and CT states (H_{DA}).

	ΔE^a cm^{-1}	ν_Q cm^{-1}	ν_Q^- cm^{-1}	$\Delta\nu_Q$ cm^{-1}	$\Delta\nu_Q°$ cm^{-1}	ξ %	$\Delta q_Q{}^b$ *e*	H_{DA} cm^{-1}
TQ_T	9257	1661±1	1511±1	150±2	159.1[c]	5.7±1.3	0.078	1600±190
TQ_TPh	9104	1661±1	1511±1	150±2	159.1[c]	5.7±1.3	0.074	1580±190
1a_Zn[d]		1656	1504	152	163.7	7.3	0.110	2330

[a]See ref. 26. [b]Δq_Q is the charge built on the Q moiety at the G state computed by $\Delta q_Q = \sum_{i\in QH_2} q_{QH_2} - \sum_{j\in Q} q_Q$. q_A is the net atomic charge on atom A as $q_A = Z_A - \sum_{r\in A} N_r$,

where N_r is the gross population. Therefore $\sum_{i \in QH_2} q_{QH_2}$ represents the charge summed over all atoms that belong to hydroquinone moiety in **TQH₂_T** or **TQH₂_TPh** and $\sum_{j \in Q} q_Q$ does that belong to Q moiety in **TQ_T** or **TQ_TPh**. [c]Based on the linear Hammett plot with data listed in Ref. 53.[54] [d]From Ref. 23.

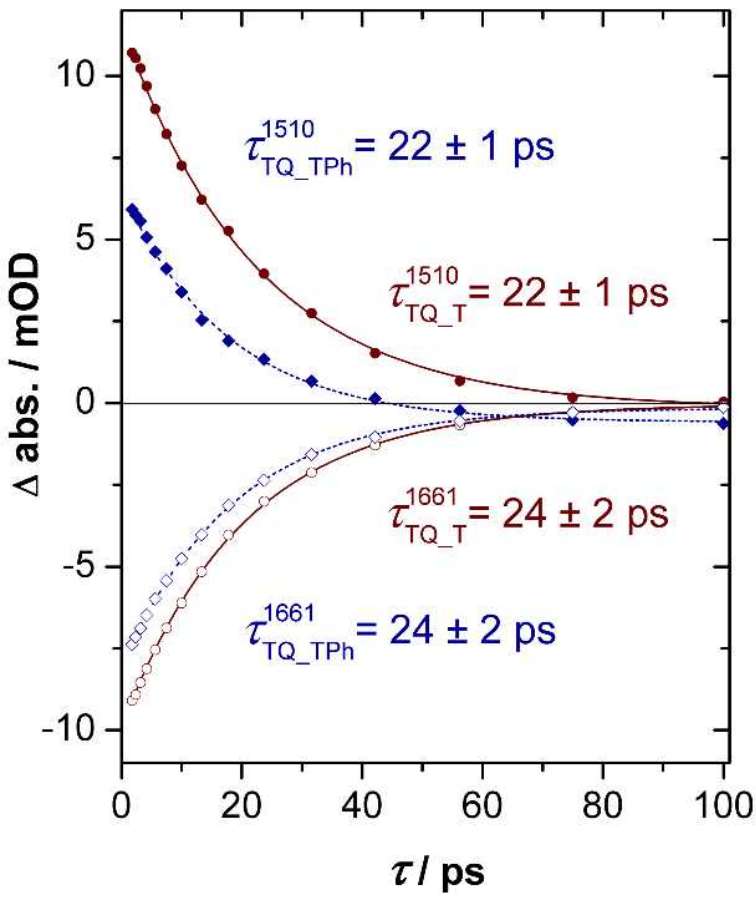

Figure 5. Decay kinetics of Q^- (top) and Q (bottom) CO stretching mode. (Experimental conditions: λ_{ex} = 575 nm, solvent = CD_3CN. Temp = 23 ± 1 °C).

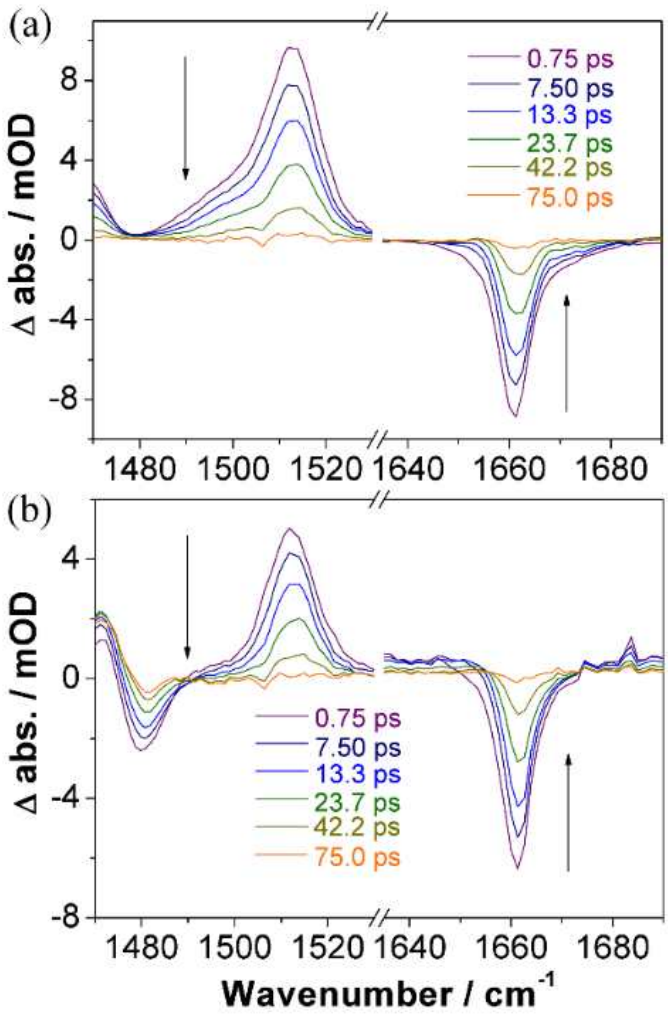

Figure 6. Time-resolved transient spectra of **TQ_T** (a) and **TQ_TPh** (b). (Experimental conditions: λ_{ex} = 575 nm, solvent = CD_3CN. Temp = 23 ± 1 °C).

In order to determine the magnitude of H_{DA} between the ground and MQCT states of these complexes, we attempted to utilize the TrIR method. The ground-state FTIR spectrum in the carbonyl (CO) stretching mode frequency domain of both **TQ_T** and **TQ_TPh** shows a clear absorption band at 1661 cm^{-1} (Figure 4). Upon electronic

excitation at 575 nm in which low energy MLCT tailing or possibly MQCT traces prevail for both **TQ_T** and **TQ_TPh** complexes, the characteristic Q^- mode appeared at 1511 cm^{-1} almost instantly with concomitant bleaching at 1661 cm^{-1} (Table 4, Figure 4). The resulting $\Delta\nu_Q$ value (150 cm^{-1}) is surprisingly similar to that measured in a cofacially aligned porphyrin-Q system (1a_Zn) reported by Rubtsov et al.[23] The correlation between transient absorption and bleaching bands was further confirmed by their time-resolved kinetic behaviors (Figure 5). The TrIR decay kinetics of **TQ_T** and **TQ_TPh** Q^- modes were fit by monoexponential function with $\tau = 22 \pm 1$ ps for both systems. Those of Q mode gave $\tau = 24 \pm 2$ ps for both, which are in good agreement with Q^- mode kinetics. Therefore, two transient IR band at 1661 and 1510 cm^{-1} can be unambiguously assigned to the CO stretching mode of ground and CT states, respectively.

Determination of the benchmark reference value of $\Delta\nu_Q°$ is of foremost important in the accurate evaluation of H_{DA}. Although Rubtsov et al. have reported $\Delta\nu_Q° = 164$ cm^{-1} with the cofacially aligned porphyrin-phenylene spacers-Q system, general use of this value appears to be risky because a carbonyl stretching frequency of one electron reduced Q anion radical should be critically dependent on the chemical environment. Even if an absolute value of $\Delta\nu_Q$ in this work is similar to that in their work, it is likely coincidental and thus a simple adoption of $\Delta\nu_Q° = 164$ cm^{-1} should be avoided.

Clark and Evans have reported the IR spectra of the anion radicals of a series of 1,4-benzoquinones.[53] The characteristic carbonyl stretching frequency decreases

upon one electron reduction from neutral quinone to radical anion for six benzoquinones. The degree of frequency shift varies by the number and the chemical property of the substituent(s) (148-169 cm^{-1}). They found a linear relationship between the IR frequencies of either a neutral or an anion radical of 6 different 1,4-benzoquinones and their corresponding $\Sigma\sigma_p$ values, where σ_p is a Hammett substituent constant. Most probable $\Delta\nu_Q°$ value was obtained from the difference between y-intercepts of two linear trend lines. The $\Delta\nu_Q°$ was 159.1 cm^{-1}.[54] This value is slightly smaller than that reported in the work of Rubstov et al (164 cm^{-1}) yet reasonable in magnitude. With this value along with the verified Q and Q^- mode CO stretching frequencies measured by TrIR spectroscopic method, we were able to determine ξ and the corresponding H_{DA} values (Table 4). The calculated H_{DA} values for **TQ_T** and **TQ_TPh** are found to be 1600 ± 190 and 1580 ± 190 cm^{-1}, respectively (Table 4). A slightly larger H_{DA} in **TQ_T** relative to **TQ_TPh** is due to the larger ΔE.

Since $\xi \cong 2C_2^2$ and C_2 is expected to scale with the Mulliken population and thus the partial charge built on the acceptor in the ground state,[23] we have calculated such values by following equation

$$\Delta q_Q = \sum_{i \in QH_2} q_i - \sum_{j \in Q} q_j \quad \text{(eq. 3)}$$

$$q_i = Z_i - \sum_{r \in i} N_r \quad \text{(eq. 4)}$$

where q_i is the net atomic charge on atom i, Z_i is the atomic number of atom i, and N_r is the gross population. For proper evaluation, we first calculated the charge built on the hydroquinone moiety (q_i) of **TQH_2_T** and **TQH_2_TPh**, where Q is replaced with

hydroquinone and thus a charge resonance between **T_T** and Q is not allowed. Each atomic charge was summed over all atoms that belong to the hydroquinone moiety ($\sum_{i \in QH_2} q_i$). We then calculated the charge built on the Q moiety (q_j) of **TQ_T** and **TQ_TPh** by the same procedure. The difference (Δq_Q) between summed charges of QH_2 ($\sum_{i \in QH_2} q_i$) and Q ($\sum_{j \in Q} q_j$) is listed in Table 4. We also listed the value calculated for 1a_Zn system[23] for comparison. In the ground state, the Q moieties of **TQ_T** and **TQ_TPh** have 0.078 *e* and 0.074 *e*, respectively. Q in1a-Zn reference system has 0.11 *e*. Given that the H_{DA} value of 1a-Zn was reported to be 2330 cm^{-1} with 0.11 *e* of Δq_Q, 0.078 *e* of Δq_Q in **TQ_T** is expected to scale 1650 cm^{-1} of H_{DA}. This result is in excellent agreement with the experimentally determined H_{DA} (~1600 cm^{-1}, Table 2). Moreover, Δq_Q in **TQ_TPh** (0.074 *e*) corresponds to 1570 cm^{-1} of H_{DA}, which is also consistent with the experimental result (~1580 cm^{-1}, Table 4). These results clearly indicate that the TrIR spectroscopic method provides physically acceptable H_{DA} value with a fair degree of accuracy.

3. Experimental Section

All manipulations were carried out under a nitrogen atmosphere. Standard Schlenk techniques were employed to manipulate air-sensitive solutions, while workup procedures were done in air. All solvents utilized in this work were obtained from Fisher Scientific (HPLC grade) and dried and distilled according to standard procedures prior to use. Tetrahydrofuran (THF) was dried over Na/benzophenone, while CH_2Cl_2 as dried over CaH_2 under nitrogen. Absolute methyl alcohol, ethyl alcohol, acetone (HPLC grade), and triethylamine (Aldrich, 99.5%) were used without any further purification. 2,6-dibromopyridine (98%), 2-bromopyridine (98%), 2,5-dimethoxyphenylboronic acid, tributyltin chloride (96%), 2,2':6',2''-terpyridine, 1-bromo-4-iodobenzene (98%), ammonium hexafluorophosphate (NH_4PF_6) were purchased from Aldrich Chemical Co. Triisopropyl borate (98%) and 2,3-dichloro-5,6-dicyano-1,4-benzoquinone(DDQ) were purchased from Acros Chemical Co. Tetrakis(triphenylphosphine)palladium(0) was purchased from Pressure Chemical Co. All deuterated solvents were purchased from Cambridge Isotope Laboratories, Inc. (Tributyl tin)-2,2'-bipyridine,[30] (2,2':6',2''-tepyridine)(trichloro)Ru(III) ($Ru(tpy)Cl_3$),[31] (4'-phenyl-2,2':6'2''-terpyridine)(trichloro)Ru(III)[32] and 4'-(2',5'-dimethoxyterphenyl)-2,2':6',2''-terpyridine)[33] were prepared by literature method. Chromatographic purification (Silica Gel 60, 230-400 mesh, Merck) of all compounds was performed on the benchtop. ^1H and ^{13}C NMR spectra were recorded with Bruker (300 MHz and 75 MHz for ^1H and ^{13}C NMR, respectively) and VARIAN Mercury (500 MHz and 125 MHz for ^1H and ^{13}C NMR, respectively) spectrometers.

^{1}H NMR spectra were taken in $CDCl_3$, DMSO-d_6, and CD_3CN and were referenced to residual TMS (0 ppm). Chemical shifts of the ^{13}C NMR spectra were measured relative to $CDCl_3$ (77.00 ppm) or DMSO-d_6 (39.52). High-resolution mass spectrometry (HRMS) data were obtained at the Korea Basic Science Institute (Daegu). Electronic absorption spectra were recorded on a Beckman Du-650 spectrophotometer. Cyclic voltammograms and differential pulse voltammetry were obtained with a CH Instrument voltammetric analyzer. Measurements were performed after the acetonitrile (spectroscopic grade) solution was purged with dry nitrogen gas for 30 min. The supporting electrolyte was 0.1 M tetrabutylammonium hexafluorophosphate ($TBAPF_6$). Glassy carbon and Ag/Ag^+ (0.01M $AgNO_3$) were used as working and reference electrodes, respectively. The scan rate was maintained at 50 mV/s.

Pump-Probe Transient Absorption Spectroscopic Measurements. The details of the time-resolved vibrational spectrometer are described elsewhere.[34-36] Briefly, two identical home-built optical parametric amplifiers (OPA), pumped by a commercial Ti:sapphire regenerative amplifier (Hurricane, Spectra Physics) with a repetition rate of 1 kHz, are used to generate a visible pump pulse and a mid-IR probe pulse. Pump pulse at 575 nm with 3.0 μJ of energy was generated by frequency doubling of a signal pulse of one OPA. Tunable mid-IR probe pulse was generated by difference frequency mixing of the signal and idler pulse of the other OPA. The polarization of the pump pulse was set at the magic angle (54.7°) relative to the probe

pulse to recover the isotropic absorption spectrum. The broadband transmitted probe pulse was detected with a 64-elements $N_2(l)$-cooled HgCdTe array detector. The array detector is mounted in the focal plane of a 320 mm monochromator with a 120 *l*/*mm* grating, resulting in a spectral resolution of ca. 1.3 cm^{-1}/pixel at 1600 cm^{-1}. The signals from each of the detector elements were amplified with a homebuilt 64-channel amplifier and digitized by a 12-bit analog-to-digital converter. Chopping the pump pulse at half the repetition frequency of the laser and computing the difference between the pumped and the unpumped absorbance determine the pump-induced change in the absorbance of the sample, ΔA. Due to the excellent short-term stability of the IR light source (< 0.5% rms), less than 1×10^{-4} rms in absorbance units after 0.5 sec of signal averaging is routinely obtained without single shot referencing with an independent detector. The pump spot was made sufficiently larger than the probe spot to ensure spatially uniform photoexcitation across the spatial dimensions of the probe pulse. The instrument response function was typically 180 fs.

Computational Method. All calculations were performed using the Gaussian 09 program package.[37] All the results were obtained using a spin-restricted formalism at the DFT level of theory[38] using the B3LYP hybrid functional.[39-43] The ruthenium atom was described by using the LANL2DZ basis set, which includes the relativistic effective core potential (ECP) of Hay and Wadt[44-46] for the inner electrons and a double-ζ basis set for the outer electrons. The standard 6-31G(d)[47] basis set was used for the remaining atoms. All geometry optimization procedure was done without any

symmetry restriction. Frequency calculations were performed to confirm the natures of the optimized stationary points and to extract the IR frequencies and intensities. The excitation energies and oscillator strengths for the three complexes at the optimized geometry in the ground state are obtained by TD-DFT calculations with the same basis sets as those for the ground state.[48,49]

Synthesis

2-Bromo-6-(2,5-dimethoxyphenyl)pyridine (1). To a flask containing 2,6-dibromopyridine (2.36 g, 10 mmol), 2,5-dimethoxyphenylboronic acid (2.18 g, 12 mmol) and tetrakis(triphenylphosphine)palladium(0) (0.58 g, 5 mol%) in 30 mL of THF solution, sodium carbonate (1.27 g, 12 mmol) in H_2O (5 mL) was added. The solution was refluxed overnight. After cooling, solvent was removed by rotary evaporator. Extraction with diethyl ether, and then purification with silica-gel column chromatography (n-hexane:ethyl acetate = 21:1) gave white solids (yield: 2.47 g, 84%). ^{1}H NMR (300 MHz, CD_3CN) δ 3.81 (s, 3 H), 3.83 (s, 3 H), 7.02 (dd, J = 3.0, 9.0 Hz, 1 H), 7.08 (d, J = 9.0 Hz, 1 H), 7.35 (d, J = 3.0 Hz, 1 H), 7.49 (d, J = 7.7 Hz, 1 H), 7.69 (t, J = 7.7 Hz, 1 H), 7.95 (d, J = 7.7 Hz, 1 H) ppm; ^{13}C NMR (75 MHz, $CDCl_3$) δ 55.9, 56.3, 113.1, 115.9, 116.3, 123.9, 126.0, 127.9, 138.1, 141.4, 151.4, 153.9, 156.7 ppm

6-(2,5-Dimethoxyphenyl)-2,2':6',2''-terpyridine (2). 6-(Tributyl tin)-2,2'-bipyridine (2.67 g, 6 mmol) in 5 mL toluene was added to 2-bromo-6-(2,5-

dimethoxyphenyl)pyridine (1.47 g, 5 mmol) and tetrakis(triphenylphosphine) palladium(0) (0.29 g, 5 mol%) in 15 mL of toluene solution. The solution was refluxed for 36 h. After cooling, solvent was removed by rotary evaporator. Crude mixture was diluted with 80 mL of CH_2Cl_2. The organic layer was washed three times with saturated aqueous KF solution to quench any residual organo-tin compounds, dried over Na_2SO_4, and then concentrated. A crude product was purified by column chromatography in neutral alumina. (*n*-hexane:ethyl acetate = 15:1) After evaporating solvent, the remaining solids were washed three times with n-hexane. White solids were obtained (yield: 0.83 g, 45%). ^{1}H NMR (500 MHz, $CDCl_3$) δ 3.37 (s, 3 H), 3.90 (s, 3 H), 6.97(d, *J* = 8.5 Hz, 1 H), 6.99 (dd, *J* = 3.0 Hz, 8.5 Hz, 1 H), 7.35 (dd, *J* = 5.0 Hz, 7.5 Hz, 1 H), 7.67 (d, *J* = 3.0 Hz, 1 H), 7.87 (dd, *J* = 5.0 Hz, 7.5 Hz, 1 H), 7.89(t, *J* = 7.5 Hz, 1 H), 7.96(t, *J* = 8.0 Hz, 1 H), 7.98(d, *J* = 7.5 Hz, 1 H), 8.45 (d, *J* = 7.5 Hz, 1 H), 8.57 (d, *J* = 8.0 Hz, 1 H), 8.62 (d, *J* = 7.5 Hz, 1 H), 8.67 (d, *J* = 8.0 Hz, 1 H), 8.72 (d, *J* = 5.0 Hz, 1 H) ppm; ^{13}C NMR (125 MHz, $CDCl_3$) δ 56.1, 56.7, 113.5, 115.4, 116.8, 119.4, 121.1, 121.4, 123.9, 125.4, 130.2, 136.8, 137.1, 138.0, 149.4, 151.9, 154.2, 154.9, 155.4, 155.9, 155.9, 156.6 ppm; HRMS(ESI), *m/z* found (calc): 369.1475 (369.1477)

6-(2,5-Dihydroxyphenyl)-2,2':6,2''-terpyridine (3). 6-(2,5-dimethoxyphenyl)-terpyridine (0.37 g, 1 mmol) was heated at reflux in 30 mL of 48 wt% hydrobromic acid. The solvent was distilled from the reaction mixture until solid began to precipitate. Then, the mixture was cooled and neutralized with solid $NaHCO_3$. The

resulting orange solid was filtered and was washed with water and was recrystallized from ethanol to give light yellow solids (yield: 0.29 g, 85%). ^{1}H NMR (500MHz, DMSO-d_6) δ 6.82 (dd, J = 2.0 Hz, 9.0 Hz, 1 H), 6.85 (d, J = 9.0 Hz, 1 H), 7.45 (d, J = 2.0 Hz, 1 H), 7.52 (t, J = 5.0 Hz, 1 H), 8.02 (t, J = 6.5 Hz, 1 H), 8.19 (m, 3 H), 8.26 (d, J = 8.0 Hz, 1 H), 8.53 (m, 2 H), 8.68 (d, J = 7.5 Hz, 1 H), 8.74 (d, J = 5.0 Hz, 1 H), 9.01 (s, 1 H), 13.31 (s, 1 H); ^{13}C NMR (75 MHz, DMSO-d_6) δ 112.9, 118.4, 119.2, 119.6, 120.8, 121.0, 121.2, 124.7, 137.9, 139.1, 139.5, 149.1, 149.7, 151.5, 152.4, 153.5, 154.6, 155.0, 156.4 ppm; HRMS(ESI), *m/z* found (calc): 341.1164 (341.1164)

[Ru(6-(2,5-dihydroxyphenyl)-2,2':6',2"-terpyridine)(2,2':6',2"-terpyridine)][PF_6]$_2$ (4). Ru(tpy)Cl_3 (88 mg, 0.2 mmol) and **3** (69 mg, 0.2 mmol) were refluxed in a mixture of ethanol (10 mL), water (1 mL), and triethylamine (5 drops) for 18 h. After cooling, solvent was removed and the resulting reaction mixture was purified by gel permeation chromatography (Sephadex LH20; methanol). The bright red band was collected and was precipitated by addition of excess aqueous NH_4PF_6 solution to give red solids. Excess NH_4PF_6 was removed by washing with water (yield: 152 mg, 79%). ^{1}H NMR (500MHz, DMSO-d_6) δ 4.86 (d, J = 3.0 Hz, 1 H), 6.13 (d, J = 8.5 Hz, 1 H), 6.29 (d, J = 8.0 Hz, 1 H), 6.30 (dd, J = 3.0 Hz, 8.5 Hz, 1 H), 7.11 (d, J = 8.0 Hz, 1 H), 7.21 (t, J = 5.5 Hz, 1 H), 7.22 (t, J = 5.5 Hz, 1 H), 7.28 (t, J = 8.0 Hz, 1 H), 7.32 (d, J = 5.5 Hz, 1 H), 7.53 (d, J = 5.5 Hz, 1 H), 7.87 (t, J = 8.0 Hz, 1 H), 7.93 (t, J = 8.0 Hz, 1 H), 8.01 (t, J = 8.0 Hz, 1 H), 8.10 (t, J = 8.0 Hz, 1 H), 8.11

(d, J = 8.0 Hz, 1 H), 8.15 (t, J = 8.0 Hz, 1 H), 8.30 (s, 1 H), 8.53(t, J = 8.0 Hz, 1 H), 8.57 (d, J = 8.0 Hz, 1 H), 8.59 (d, J = 8.0 Hz, 1 H), 8.67 (d, J = 8.0 Hz, 1 H), 8.68 (s, 1 H), 8.69 (d, J = 8.0 Hz, 1 H), 8.9 1(d, J = 8.0 Hz, 1 H), 8.97 (d, J = 8.0 Hz, 1 H), 9.20 (d, J = 8.0 Hz, 1 H) ppm; ^{13}C NMR (125 MHz, DMSO-d_6) δ 119.2, 121.3, 122.6, 128.0, 128.5, 128.7, 129.2, 129.4, 129.6, 129.7, 129.8, 129.9, 132.2, 132.5, 133.2, 134.2, 140.0, 141.0, 142.8, 142.9, 143.3, 143.6, 151.3, 153.5, 154.9, 156.9, 157.3, 159.4, 159.6, 159.8, 160.3, 162.8, 163.19, 163.23, 163.6, 168.4 ppm; HRMS(FAB), m/z $[M]^{2+}$ found (calc): 676.1164 (676.1171)

[Ru(6-(2-cyclohexa-2',5'-diene-1,4-dionyl)-2,2':6',2"-terpyridine)(2,2':6',2"-terpyridine)][PF_6]$_2$ (5, TQ_T). **4** (97 mg, 0.1 mmol) and 10 equivalents of DDQ were dissolved in 5 mL of distilled acetone and stirred at rt under argon overnight. The solution was dropped in 100 mL of diethyl ether. Brown solids were filtered and were washed with diethyl ether several times (yield: quantitative). ^{1}H NMR (500MHz, DMSO-d_6) δ 5.56 (d, J = 2.6 Hz, 1 H), 6.41 (d, J = 5.8 Hz, 1 H), 6.46 (d, J = 10.2 Hz, 1 H), 6.68 (dd, J = 2.6 Hz, 10.2 Hz, 1 H), 7.23 (dd, J = 5.8 Hz, 7.5 Hz, 1 H), 7.33 (dd, J = 5.5 Hz, 7.4 Hz, 1 H), 7.34 (dd, J = 4.7 Hz, 7.4 Hz, 1 H), 7.35 (d, J = 7.9 Hz, 1 H), 7.38 (d, J = 4.7 Hz, 1 H), 7.62 (d, J = 5.5 Hz, 1 H), 7.93 (dd, J = 5.5 Hz, 7.5 Hz, 1 H), 8.04 (dd, J = 5.5 Hz, 7.4 Hz, 1 H), 8.10 (dd, J = 4.7 Hz, 7.4 Hz, 1 H), 8.23 (t, J = 7.9 Hz, 1 H), 8.36 (t, J = 8.1 Hz, 1 H), 8.59 (t, J = 8.2 Hz, 1 H), 8.68 (d, J = 7.4 Hz, 1 H), 8.70 (d, J = 7.4 Hz, 1H), 8.73 (d, J =7.5 Hz, 1 H), 8.90 (d, J = 8.1 Hz, 2 H), 9.03 (d, 7.9 Hz, 1 H), 9.04 (d, J = 8.2 Hz, 1 H), 9.27 (d, J = 8.2 Hz, 1 H) ppm;

^{13}C NMR (125 MHz, DMSO-d_6) δ 125.03, 125.04, 125.06, 125.08, 135.3, 135.4, 136.25, 136.26, 136.27, 136.37, 136.41, 136.43, 136.44, 136.45, 136.48, 136.49, 136.6, 138.14, 138.15, 138.16, 138.17, 138.5, 139.0, 140.9, 154.23, 154.24, 154.6, 154.8, 155.5, 157.1, 157.3, 157.7, 157.8, 158.0, 184.8, 186.6 ppm; HRMS(FAB), *m/z* $[M]^{2+}$ found (calc): 674.1008 (674.1014)

[Ru(6-(2,5-dihydroxyphenyl)-2,2':6',2"-terpyridine)(4'-phenyl-2,2':6',2"-terpyridine)][PF_6]$_2$ (6). Ru(tpy-Ph)Cl_3 (104 mg, 0.2 mmol) and **3** (69 mg, 0.2 mmol) were refluxed in a mixture of ethanol (10 mL), water (1 mL), and triethylamine (5 drops) for 18 h. After cooling, solvent was removed and the resulting reaction mixture was purified by gel permeation chromatography (Sephadex LH20; methanol). The bright red band was collected and was precipitated by the addition of excess aqueous NH_4PF_6 solution. The precipitates were washed with water. Red solids were obtained (yield: 185 mg, 89 %). ^{1}H NMR (500MHz, DMSO-d_6) δ 4.91 (d, J = 2.0 Hz, 1 H), 6.13 (d, J = 8.0 Hz, 1 H), 6.20 (dd, J = 2.0 Hz, 8.0 Hz, 1 H), 6.54 (d, J = 5.0 Hz, 1 H), 7.12 (d, J = 7.5 Hz, 1 H), 7.23 (m, 2 H), 7.30 (t, J = 5.0 Hz, 1 H), 7.34 (d, J = 5.0 Hz, 1 H), 7.58 (d, J = 5.0 Hz, 1 H), 7.67 (t, J = 7.0 Hz, 1 H), 7.77 (m, 2 H), 7.91 (t, J = 7.5 Hz, 1 H), 7.98 (t, J = 7.5 Hz, 1 H), 8.06 (t, J = 7.5 Hz, 1 H), 8.11 (t, J = 7.5 Hz, 1 H), 8.15 (s, 1 H), 8.26 (s, 1 H), 8.28 (s, 1 H), 8.56 (t, J = 7.5 Hz, 1 H), 8.70 (s, 1 H), 8.72 (d, J = 8.0 Hz, 1 H), 8.85 (m, 2 H), 8.94 (d, J = 8.0 Hz, 1 H), 9.02 (m, 3 H), 9.23 (d, J = 8.0 Hz, 1 H) ppm; ^{13}C NMR (125 MHz, DMSO-d_6) δ 121.3, 123.54, 123.55, 123.56, 124.3, 124.9, 125.0, 127.9, 128.0, 128.1, 128.3, 129.32, 129.33, 129.34, 129.4,

130.4, 131.1, 132.0, 135.8, 136.8, 137.2, 137.6, 137.7, 138.1, 138.3, 138.4, 140.6, 142.5, 146.2, 146.52, 146.53, 146.6, 146.9, 148.5, 149.0. 150.1, 154.7, 154.8, 155.2, 156.3, 158.7, 159.3 ppm; HRMS(FAB), *m/z* $[M+PF_6]^+$ found (calc): 897.1112 (897.1127)

[Ru(6-(2-cyclohexa-2',5'-diene-1,4-dionyl)- 2,2':6',2"-terpyridine)(4'-phenyl-2,2':6',2"-terpyridine)][PF_6]$_2$ (7, TQ_TPh). **6** (104 mg, 0.1 mmol) and 10 equivalents of DDQ were dissolved in 5 mL of distilled acetone and were stirred at rt under argon overnight. The solution was dropped in 100 mL of diethyl ether. Brown solid was filtered and was washed with diethyl ether several times (yield: quantitative). ^{1}H NMR (500MHz, DMSO-d_6) δ 5.63 (d, J = 2.5 Hz, 1 H), 6.45 (dd, J = 2.5 Hz, 10.2 Hz, 1 H), 6.52 (d, J = 10.2 Hz, 1 H), 6.66 (d, J = 5.2 Hz, 1 H), 7.22 (dd, J = 5.2 Hz, 8.0 Hz, 1 H), 7.30 (d, J = 7.5 Hz, 1 H), 7.31 (dd, J = 5.0 Hz, 8.0 Hz, 1 H), 7.32 (dd, J = 5.0 Hz, 8.0 Hz, 1 H), 7.41 (d, J = 5.0 Hz, 1 H), 7. 61 (d, J = 5.0 Hz, 1 H), 7.69 (t, J = 7.7 Hz, 1 H), 7.76 (t, J = 7.7 Hz, 2 H), 7.91 (dd, J = 8.0 Hz, 8.3 Hz, 1H), 8.04(dd, J = 5.0, 8.0 Hz, 1 H), 8.09 (dd, J = 5.0 Hz, 8.0 Hz, 1 H), 8.20 (t, J = 7.0 Hz, 1 H), 8.28 (d, J = 7.7 Hz, 2 H), 8.56 (t, J = 8.2 Hz, 1 H), 8.70 (d, J = 8.3 Hz, 1 H), 8.89 (d, J = 8.0 Hz, 1 H), 8.94 (d, J = 8.0 Hz, 1 H), 8.98 (d, J = 8.2 Hz, 1 H), 9.00 (d, J = 8.2 Hz, 1 H), 9.18 (s, 1H), 9.20(s, 1 H), 9.22 (d, J = 8.2 Hz, 1 H) ppm; ^{13}C NMR (125 MHz, DMSO-d_6) δ 128.1, 128.80, 128.81, 128.82, 128.83, 128.84, 128.86, 128.87, 128.89, 128.90, 128.91, 131.73, 131.74, 131.75, 131.76, 131.77, 131.79, 131.81, 131.82, 131.91, 131.92, 136.2, 138.16, 138.17, 138.18, 141.2, 148.03,

148.04, 154.4, 154.7, 155.2, 155.83, 155.85, 157.5, 157.7, 157.8, 157.9, 158.0, 158.2, 158.3, 184.9, 186.7 ppm; HRMS(FAB), *m/z* $[M+H]^+$ found (calc): 751.1387 (751.1407)

4. Reference

(1) Mulliken, R. S. *J. Am. Chem. Soc.* **1952,** *74*, 811-824.

(2) Hush, N. S. *Prog. Inorg. Chem.* **1967,** *8*, 391-444.

(3) Sutin, N. *Prog. Inorg. Chem.* **1983,** *30*, 441-498.

(4) Creutz, C.; Newton, M. D.; Sutin, N. *J. Photochem. Photobiol. A: Chem.* **1994,** *82*, 47-59.

(5) Brunschwig, B. S.; Creutz, C.; Sutin, N. *Chem. Soc. Rev.* **2002,** *31*, 168-184.

(6) Demadis, K. D.; Hartshorn, C. M.; Meyer, T. J. *Chem. Rev.* **2001,** *101*, 2655-2685.

(7) Sauvage, J. P.; Collin, J. P.; Chambron, J. C.; Guillerez, S.; Coudret, C.; Balzani, V.; Barigelletti, F.; Decola, L.; Flamigni, L. *Chem. Rev.* **1994,** *94*, 993-1019.

(8) Newton, M. D. *Chem. Rev.* **1991,** *91*, 767-792.

(9) Richardson, D. E.; Taube, H. *Coord. Chem. Rev.* **1984,** *60*, 107-129.

(10) Creutz, C. *Prog. Inorg. Chem.* **1983,** *30*, 1-73.

(11) Sun, D.; Rosokha, S. V.; Kochi, J. K. *J. Am. Chem. Soc.* **2004,** *126*, 1388-1401.

(12) Bailey, S. E.; Zink, J. I.; Nelsen, S. F. *J. Am. Chem. Soc.* **2003,** *125*, 5939-5947.

(13) Cooley, L. F.; Han, H.; Zimmt, M. B. *J. Phys. Chem. A* **2002,** *106*, 884-892.

(14) Bixon, M.; Jortner, J.; Verhoeven, J. W. *J. Am. Chem. Soc.* **1994,** *116*, 7349-7355.

(15) Gould, I. R.; Young, R. H.; Mueller, L. J.; Albrecht, A. C.; Farid, S. *J. Am. Chem. Soc.* **1994,** *116*, 3147-3148.

(16) Reimers, J. R.; Hush, N. S. *Inorg. Chem.* **1990,** *29*, 3686-3697.

(17) Oevering, H.; Verhoeven, J. W.; Paddonrow, M. N.; Warman, J. M. *Tetrahedron* **1989,** *45*, 4751-4766.

(18) Desbois, M. H.; Astruc, D.; Guillin, J.; Mariot, J. P.; Varret, F. *J. Am. Chem. Soc.* **1985,** *107*, 5280-5282.

(19) Cave, R. J.; Newton, M. D. *Chem. Phys. Lett.* **1996,** *249*, 15-19.

(20) Cave, R. J.; Newton, M. D. *J. Chem. Phys.* **1997,** *106*, 9213-9226.

(21) Zheng, J. R.; Kang, Y. K.; Therien, M. J.; Beratan, D. N. *J. Am. Chem. Soc.* **2005,** *127*, 11303-11310.

(22) Voityuk, A. A. *Chem. Phys. Lett.* **2006,** *422*, 15-19.

(23) Rubtsov, I. V.; Kang, Y. K.; Redmore, N. P.; Allen, R. M.; Zheng, J. R.; Beratan, D. N.; Therien, M. J. *J. Am. Chem. Soc.* **2004,** *126*, 5022-5023.

(24) In this two state model, the overlap integral S is neglected.

(25) $\Delta n_Q^\circ = n_Q^\circ - n_Q^{-\circ}$, where n_Q° and $n_Q^{-\circ}$ are diabatic ground and CT state CO frequencies, respectively. Similarly, $\Delta n_Q = n_Q - n_Q^-$, where n_Q and n_Q^- are corresponding adiabatic parameters.

(26) Calculated by the equation $\Delta E = e(E_{red} - E_{ox}) + \frac{e^2}{4\pi\varepsilon_0\varepsilon_S R_{DA}}$, where E_{red} and E_{ox} are the respective acceptor (Q) and donor ($[Ru(tpy)_2]^{2+}$) redox potentials, ε_s is the solvent dielectric constant, R_{DA} is the Ru-to-quinonyl centroid distance.

(27) Creutz, C.; Brunschwig, B. S.; Sutin, N. *J. Phys. Chem. B* **2005,** *109*, 10251-10260.

(28) Creutz, C.; Brunschwig, B. S.; Sutin, N. *Chem. Phys.* **2006,** *324*, 244-258.

(29) Creutz, C.; Brunschwig, B. S.; Sutin, N. *J. Phys. Chem. B* **2006,** *110*, 25181-25190.

(30) Heuberger, B. D.; Shin, D.; Switzer, C. *Org. Lett.* **2008,** *10*, 1091-1094.

(31) Sullivan, B. P.; Calvert, J. M.; Meyer, T. J. *Inorg. Chem.* **1980,** *19*, 1404-1407.

(32) Taher, D.; Thibault, M. E.; Di Monde, D.; Schlaf, M. *Chem. Eur. J.* **2009,** *15*, 10132-10143.

(33) Aleman, E. A.; Shreiner, C. D.; Rajesh, C. S.; Smith, T.; Garrison, S. A.; Modarelli, D. A. *Dalton Trans.* **2009,** 6562-6577.

(34) Kim, J.; Park, J.; Lee, T.; Lim, M. *J. Phys.Chem.B.* **2009,** *113*, 260-266.

(35) Lee, T.; Park, J.; Kim, J.; Joo, S.; Lim, M. *Bull. Kor. Chem. Soc.* **2009,** *30*, 177-182.

(36) Kim, S.; Jin, G.; Lim, M. *J. Phys.Chem.B.* **2004,** *108*, 20366-20375.

(37) Frisch, M. J. e. a. *Gaussian 09, Revision B.01; Gaussian, Inc.: Wallingford, CT, 2010.*

(38) Kohn, W.; Sham, L. J. *Phys. Rev.* **1965,** *140*, A1133-A1138.

(39) Becke, A. D. *J. Chem. Phys.* **1993,** *98*, 5648-5652.

(40) Stephens, P. J.; Devlin, F. J.; Chabalowski, C. F.; Frisch, M. J. *J. Phys. Chem.* **1994,** *98*, 11623-11627.

(41) Hertwig, R. H.; Koch, W. *Chem. Phys. Lett.* **1997,** *268*, 345-351.

(42) Pietro, W. J.; Francl, M. M.; Hehre, W. J.; DeFrees, D. J.; Pople, J. A. *J. Am. Chem. Soc.* **1982,** *104*, 5039-5048.

(43) Lee, C. T.; Yang, W. T.; Parr, R. G. *Phys. Rev. B* **1988,** *37*, 785-789.

(44) Hay, P. J.; Wadt, W. R. *J. Chem. Phys.* **1985,** *82*, 270-283.

(45) Wadt, W. R.; Hay, P. J. *J. Chem. Phys.* **1985,** *82*, 284-298.

(46) Hay, P. J.; Wadt, W. R. *J. Chem. Phys.* **1985,** *82*, 299-310.

(47) Hehre, W. J.; Ditchfield, R.; Pople, J. A. *J. Chem. Phys.* **1972,** *56*, 2257-2261.

(48) Runge, E.; Gross, E. K. U. *Phys. Rev. Lett.* **1984,** *52*, 997-1000.

(49) Bartolotti, L. J. *Phys. Rev. A* **1982,** *26*, 2243-2244.

(50) Iovine, P. M.; Kellett, M. A.; Redmore, N. P.; Therien, M. J. *J. Am. Chem. Soc.* **2000,** *122*, 8717-8727.

(51) Iovine, P. M.; Veglia, G.; Furst, G.; Therien, M. J. *J. Am. Chem. Soc.* **2001,** *123*, 5668-5679.

(52) All electrochemical potentials are relative to NHE.

(53) Clark, B. R.; Evans, D. H. *J. Electroanal. Chem.* **1976,** *69*, 181-194.

(54) They reported the average value was 155 cm^{-1}. However, the value has been modified to 159.1 cm^{-1} while we reproduced the plot with data listed in their paper.

5. Supporting Information

Figure 7. 2D-GCosy Spectra of **TQ_T**

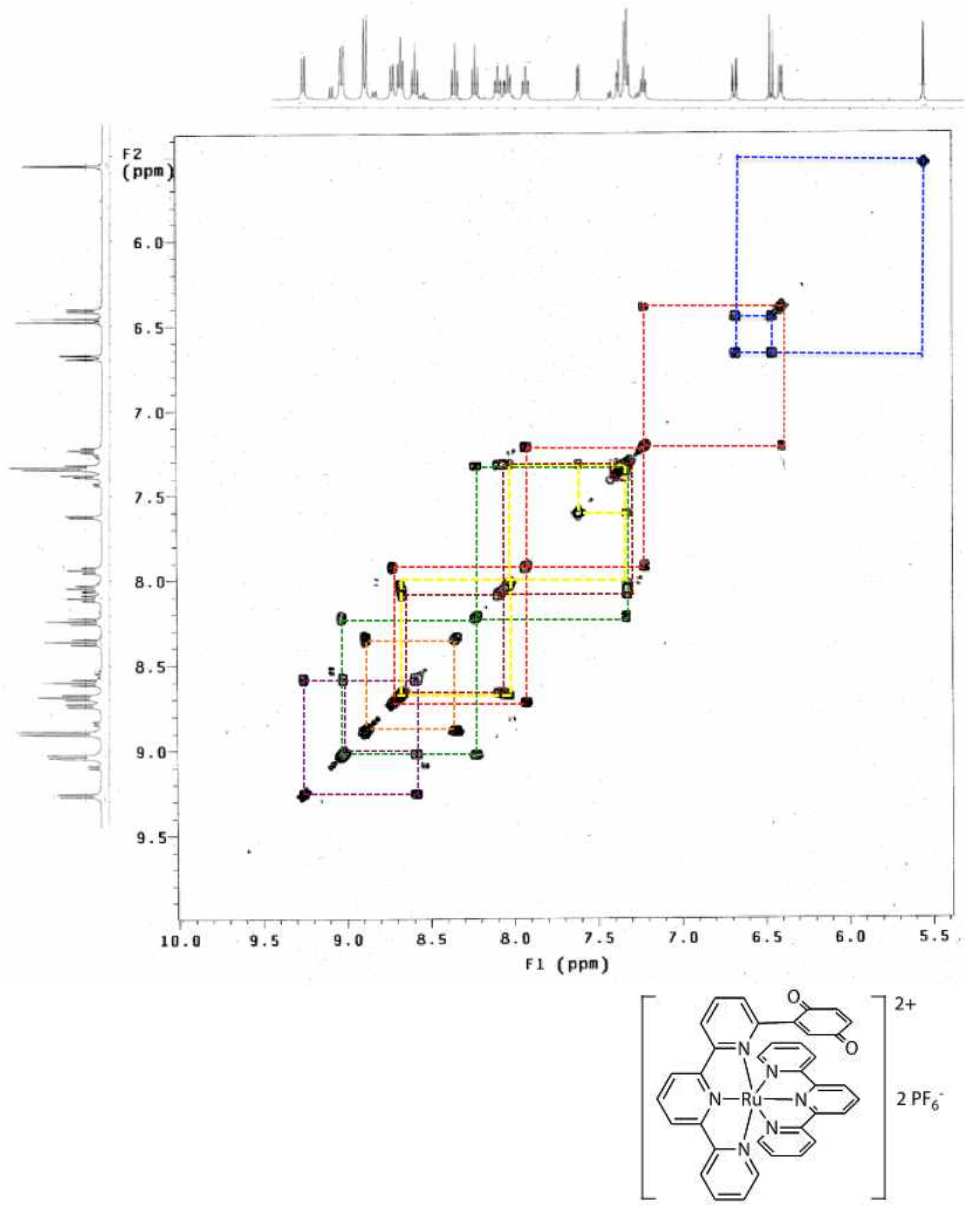

Figure 8. 2D-Cosy Spectra of **TQ_TPh**

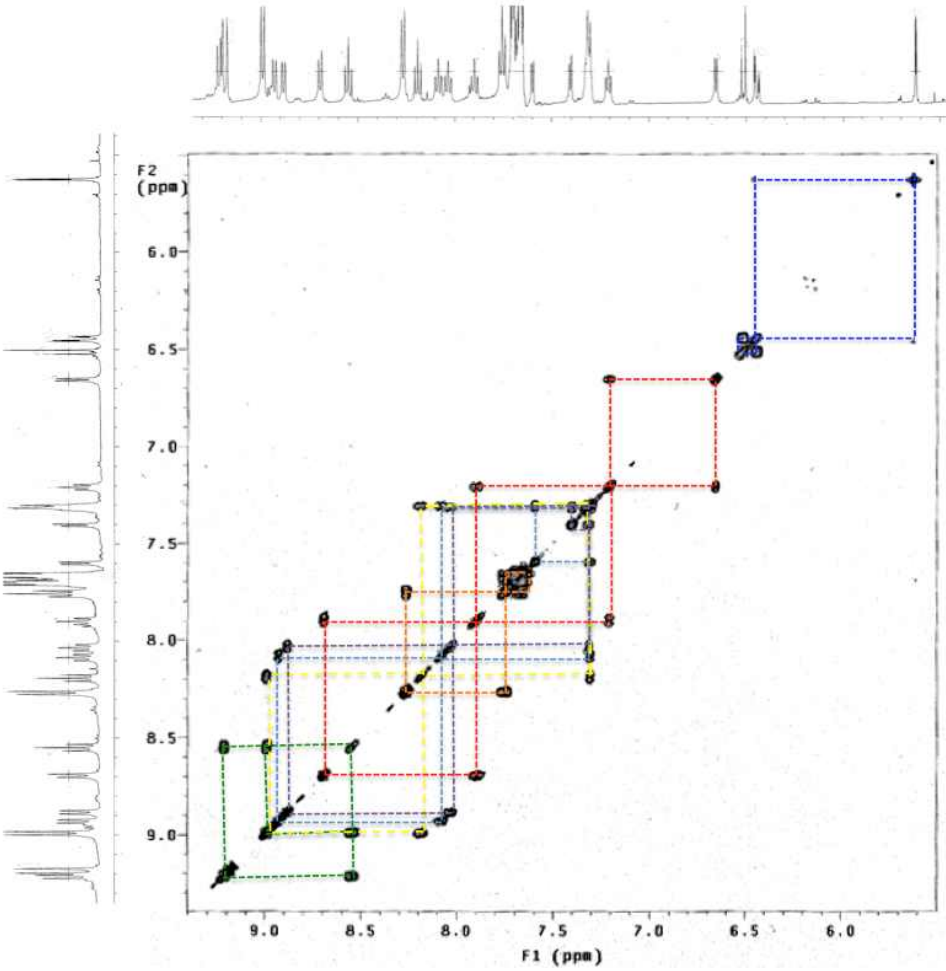

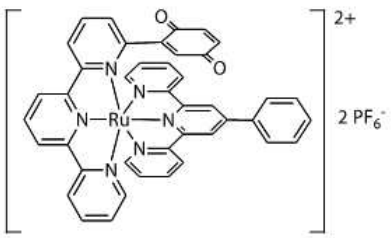

Section 2.

Study on 1-Benzoquinonyl NN^C Type *N*-Heterocyclic Ligand Based on Ru(II) Complexes

1. Introduction

Vectorial electron transfer is of primary interest in artificial photosynthesis.[1-10] The ultimate goal is to generate a long-lived CS state in which an electron donor (D) and acceptor (A) is separated by a controllable distance enough to perform a variety of chemical reactions with the driving force obtained by the CS. In the early event of natural photosynthesis, CS through protein membrane occurs via only one direction (L-branch, *vide infra*) between the macroscopic C_2 symmetric L- and M- branches,; (L) the special pair-bacteriochlorophyll ($BChl_L$)-bacteriopheophytin ($BPheo_L$)-menaquinone (Q_a)-ubiquinone (Q_b) and (M) the special pair-bacteriochlorophyll ($BChl_M$)-bacteriopheophytin ($BPheo_M$)-ubiquinone (Q_b)-menaquinone (Q_a).[11-20] Extensive efforts have been devoted to elucidate the background of this phenomenon; modeling the competition between through-space and through-bond electron transfer is one of those efforts. We have recently reported the photo-induced CS and thermal CR reactions via ultrafast TrIR spectroscopy for the [Ru(6-(2-cyclohexa-2',5'-diene-1,4-dione)-2,2':6',2"-terpyridine)(2,2':6',2"-terpyridine)][PF_6]$_2$ (TQ_T) system where the orthogonal alignment of Q to tpy ligand imposes this unit juxtaposed cofacially on the central pyridyl ring of second tpy ligand (Scheme 1).[21] CS reaction occurs almost instantaneously and CR reaction does with time constant of 22 ps. Due to the fact that the CS reaction is ultrafast in nature, and the authentic generation of Ru-to-tpy_1 MLCT state was not available, the detailed elucidation of electron transfer pathway could not be determined. The major question is whether ET reaction undergoes through the Ru-tpy_2-Q pathway via π-stacked D-A manifold or through

Ru-tpy$_1$-Q via through-bond mechanism (Scheme 1). In order to decipher this fundamental question, we have newly designed and synthesize ImQ_T, in which D and A topology is as same as TQ_T but the methylene bridge between bpy and imidazolyl moiety blocks the electronic delocalization of the ligand and thus an efficient charge transfer through this unit is inherently inhibited. The design of ImQ_T is largely indebted to its archetype, [Ru(3-(2,2'-bipyridine-6-yl-methyl)-1-methyl-1*H*-imidazole)(2,2':6',2"-terpyridine)] $[PF_6]_2$ (Ru(tpy)(b^im)).[22] The characteristic feature of Ru(tpy)(b^im) is its electronic structure where the imidazolyl-Ru moiety constitutes HOMO and the tpy moiety does LUMO. Due to this spatial separation of frontier orbitals, selective excitation toward a particular ligand, *e.g.* tpy, became available, from which a consecutive CS reaction can be manipulated. Here we report synthesis and geometry, ground- and excited state electronic structures, and CS and CR reaction dynamics of ImQ_T molecule.

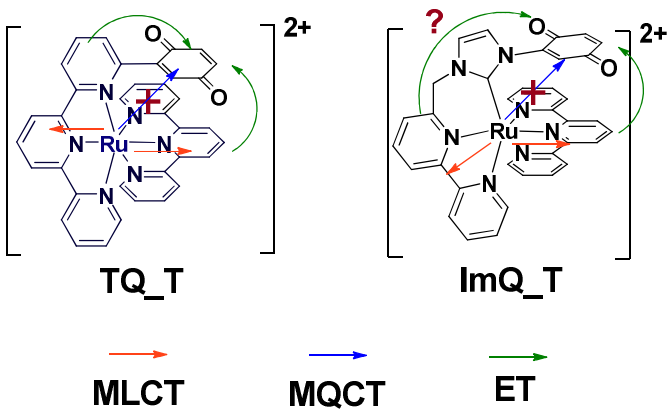

Scheme 1.

2. Results and Discussion

(1) Synthesis and Structure.

The design strategy of ImQ_T complex was inspired by the TQ_T topology[21] that satisfies two conditions; (1) electron acceptor, Q, should be placed juxtaposed to the primary ligand (tpy) to facilitate $\pi-\pi$ interaction, (2) the direct conjugation between the secondary ligand (bpy) and the electron acceptor moiety should be minimized. In our previous work, we observed that the electronic population of the LUMO of $[Ru(bip)_2]^{2+}$ (bip = 2,6-bis(3-methylimidazol-1-yl)pyridine) is mainly localized in the central pyridyl ring indicating that the electron is not delocalized over the whole bip ligand but is confined within the central pyridyl ring.[40] Furthermore, we observed that LUMO energy levels were leveled in the series of heteroleptic $[Ru(tpy)L]^{2+}$ complexes in which L is either NNC or NN^C structural motif.[22] These works demonstrate that an electronic delocalization between the pyridyl ring and the imidazolyl one in bip ligand or that between the bipyridyl ring and the imidazolyl one in NNC or NN^C type ligands is inherently blocked regardless the presence of a methylene bridge between two units. Thus the electronic population in the Ru-to-bpy MLCT state of ImQ_T can be segregated from the Q moiety. The photo-induced CS as well as thermal CR reaction pathways would be determined by the competition between through-space Ru-tpy-Q route and through-bond Ru-bpy-methylene bridge-imidazole-Q counterpart if the laser excitation generates mixed Ru-to-tpy/Ru-to-bpy MLCTs. However, if a selective preparation of either one of such MLCTs is possible, the elucidation of electron transfer dynamics for a particular pathway becomes

available.

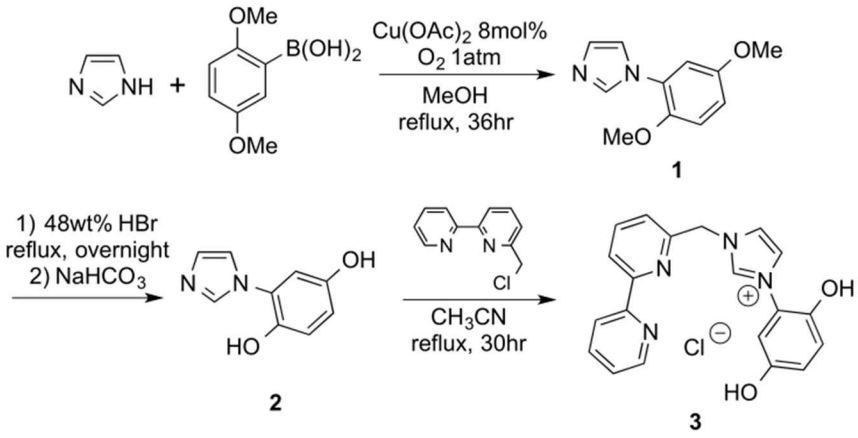

Scheme 2. Synthesis of ligand.

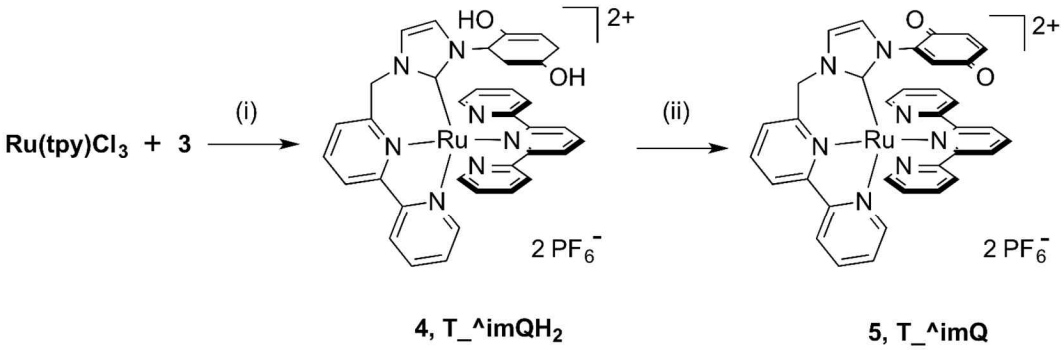

(i) ethylene glycol, 160°C, 4 hr, NH_4PF_6, (ii) 10eq DDQ, acetone, rt, 12 hr

Scheme 3. Synthesis of Ru-Q complex.

The synthesis of 1-([2,2'-bipyridine]-6-yl-methyl)-3-(2,5-dihydroxyphenyl)-1*H*-imidazol-3-ium chloride (3) was accomplished by the reaction sequence shown in Scheme 2. In the presence of catalytic amount of copper acetate, the coupling reaction between imidazole and 2,5-dimethoxyphenylboronic acid was performed in methanol under oxygen atmosphere, which affords 1-(2,5-dimethoxypheny)-1*H*-limidazole (1) in 82% yield. A subsequent demethylation of 1 with HBr gave 2 in 94% yield. Reaction of 2 with 6-(chloromethyl)-2,2'-bipyridine in refluxing acetonitrile gave the hydroquinonyl substituted imidazolium compound, 3, in 92% yield.

In order to attach the prepared ligand to the Ru metal, we employed [Ru(tpy)Cl_3] for the metallating agent. The reaction requires high temperature; 4 hours of the reaction in ethylene glycol at 160°C followed by the anion exchange with NH_4PF_6 afforded the heteroleptic ruthenium complex, ImQH_2_T (4) in 69% yield. The subsequent oxidation of hydroquinone to 1,4-benzoquinone was done by using DDQ as an oxidizing agent. The desired final complex was obtained quantitatively.

Figure 1 illustrates the geometry of ImQ_T optimized by DFT calculation at B3LYP/6-31g(d)-LANL2DZ level. The geometry of TQ_T benchmark reported in our previous work[21] is also displayed for the comparison. Due to the methylene bridge, bpy and imidazolyl ring is not coplanar. Imidazolyl ring is distorted from the bpy plane and thus the Q ring is directed outward from the vertical plane that bisects the tpy ligand. As a result, the centroid of Q ring plane is laterally shifted toward the peripheral pyridyl ring from the top of the central pyridyl ring of the tpy ligand. The distance between Ru metal and the centroid of Q ring is 4.81Å, which is 0.12Å longer

than that of TQ_T. The distances between the Q centroid and tpy ring plane of ImQ_T and TQ_T are, however, similar each other; 3.54 and 3.58Å, respectively. The slightly shorter plane-to-plane distance observed in ImQ_T is due to the larger bite angle of N_{pyr}-Ru-C_{im}[41] compared to that of N_{pyr}-Ru- N_{pyr} in TQ_T.

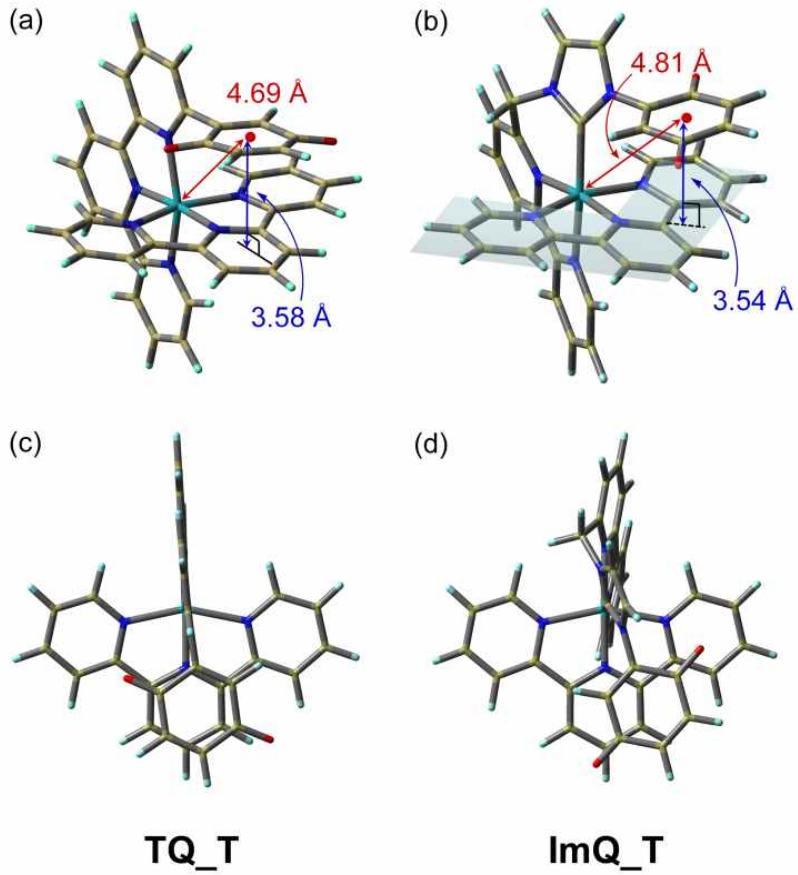

Figure 1. Geometries of TQ_T (a) and ImQ_T (b) with their top views (c and d). Metal-to-quinonyl plane centroid distances are shown in red. Quinonyl plane-to-terpyridyl plane distances are shown in blue.

The degree of π–π stacking interaction can be scaled by the chemical shifts of ^{1}H-NMR spectra of corresponding proton peaks.[42,43] The characteristic splitting patterns of Q ring protons unambiguously displays their peak positions at 6.79, 6.63, and 6.20 ppm. Considering the fact that chemical shifts of corresponding TQ_T Q proton peaks were observed at 6.68, 6.41. and 5.56 ppm, the π–π stacking interaction between tpy and Q of ImQ_T is seemingly less than that of TQ_T. Since the Q plane-to-tpy plane distance of ImQ_T is slightly shorter than that of TQ_T according to the calculated geometry, the concomitant down field shifts of Q proton peaks of ImQ_T relative to TQ_T are contradictory. The background of this result can be explained by the characteristic structural feature of ImQ_T; the Q ring is not exactly cofacial with the central pyridyl ring of tpy ligand. Therefore, the Q protons are less affected by the ring current imposed by the aromatic ring of tpy ligand and thus the peak positions of Q protons are going back to their original positions. Accordingly, the D-A electronic coupling in ImQ_T is expected to be decreased relative to TQ_T.

(2) Electrochemistry and Molecular Orbitals.

The electrochemical redox potentials of the ImQ_T in acetonitrile were recorded and their values are listed in Table 1. Both one electron oxidation and reduction occur reversibly at 1.46 and 0.11 V vs. NHE, respectively. The latter is shifted positively by 0.13 V relative to the value observed for TQ_T benchmark (-0.02 V vs. NHE) while the former is 0.18 V shifted negatively. The difference between the oxidation and reduction potentials of ImQ_T is 0.31 V smaller than that of TQ_T, and thus the

energy level of charge separated state of ImQ_T is expected to be lower by the same amount than that of TQ_T. This difference gives rise to the change of the driving force of electron transfer reaction.

Table 1. Spectroscopic and Voltammetric Data.

Complex	λ_{max} [a]		ε	$E_{1/2}^{ox}$ [b]	$E_{1/2}^{red}$ [b]
	nm	cm^{-1}	$M^{-1}cm^{-1}$	V vs. NHE	
TQ_T	473	21,142	13,400	1.64	-0.02
ImQ_T	477	20,964	9,000	1.46	0.11

[a]Experimental conditions: solvent = acetonitrile, temperature = 23 ± 1°C. [b]Experimental conditions: [compound] = 5 mM; [$TBAPF_6$] = 0.1 M; solvent = acetonitrile; temperature = 23 ± 1°C; scan rate = 50 mV/s; reference electrode = Ag/Ag+; working electrode = glassy carbon. All potentials are referenced to a ferrocene/ferrocenium redox couple as an internal standard and converted to NHE by the relation ferrocene/ferrocenium vs. NHE = +0.64 V.

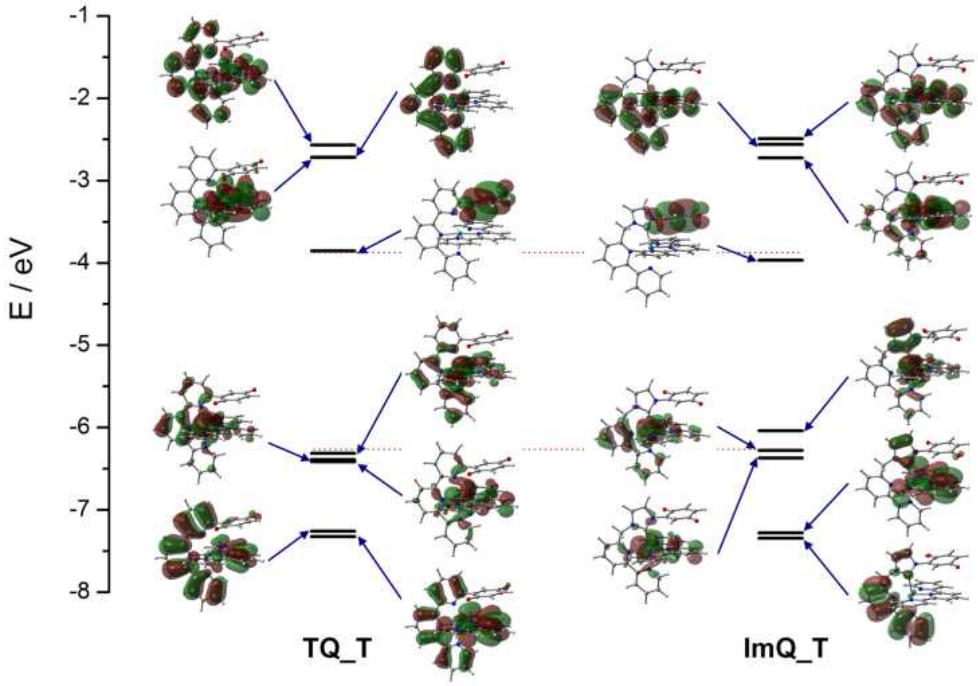

Figure 2. 3-Dimensional representations of frontier molecular orbital isosurfaces calculated at the B3LYP/LANL2DZ level. The MO isosurfaces of TQ_T molecule is from ref. 21.

The DFT calculation result supports the electrochemical data. The calculated frontier molecular orbital energies and their corresponding isosurfaces are shown in Figure 2. The electronic populations of LUMOs of both ImQ_T and TQ_T are confined in Q moieties. On the other hand, those of HOMOs of two systems are mainly localized in Ru metal with a small amount being spread over the ligand system. For TQ_T, the electronic population of HOMO at Ru metal is ca. 75% and the rest 25% is equally distributed in two tpy ligands (Table 2). However, the electronic population of HOMO at Ru metal in ImQ_T is only 64.4% and those at tpy and imidazolyl ring are 10.5 and 20.3%, respectively. More specifically, HOMO is

constituted of Ru *d* orbitals and ligand π orbitals implying that the imidazol group provides a strong π-donation effect besides a σ-donation effect. As a result, the HOMO energy level of ImQ_T is destabilized compared to TQ_T, which gives rise to the negative shift of electrochemical oxidation potential. The calculated HOMO energy levels of ImQ_T and TQ_T are –6.04 and -6.31 eV; the difference of 0.27 eV is similar to that observed in the electrochemical oxidation potentials of two systems (0.18V). The calculated value of LUMO energies of ImQ_T and TQ_T are -3.97 and -3.85 eV, respectively. Considering the fact that the electrochemical reduction potentials of two systems were 0.11 and -0.02 V, which differ by 0.13 V, 0.12 V of difference obtained from the calculation is in excellent agreement with the experimental result.

Table 2. Energies and Percent Compositions of Frontier MOs of TQ_T, and ImQ_T.

TQ_T						ImQ_T						
MO		Electron Population (%)				MO		Electron Population (%)				
No.	E (eV)	Ru	Tpy_1[a]	Tpy_2[b]	Q	No.	E (eV)	Ru	Tpy	Bpy	^Im	Q
3[c] (159)	-2.72	8.2	4.9	85.9	1.0	3[c] (160)	-2.56	3.4	41.5	52.2	2.3	0.6
2[c] (158)	-2.72	8.7	85.8	3.9	1.6	2[c] (159)	-2.72	7.5	80.7	9.3	1.8	0.6
1[c] (157)	-3.85	0.3	2.9	2.0	94.9	1[c] (158)	-3.97	0.4	1.9	0.1	1.8	95.8
0[c] (156)	-6.31	74.5	13.2	12.3	0.1	0[c] (157)	-6.04	64.4	10.5	3.8	20.3	1.0
-1[c](155)	-6.39	74.0	12.3	13.4	0.3	-1[c](156)	-6.28	76.8	13.4	9.1	0.7	0.0
-2[c](154)	-6.42	74.5	14.5	10.9	0.2	-2[c](155)	-6.37	77.6	14.5	4.6	3.0	0.3
-3[c](153)	-7.26	0.4	25.0	72.0	2.7	-3[c](154)	-7.28	1.0	88.6	0.5	8.8	1.1
-4[c](152)	-7.33	4.5	71.0	22.9	1.5	-4[c](153)	-7.35	0.7	1.2	91.0	6.7	0.4

[a]Tpy ligand coplanar to Q. [b]Tpy ligand where Q is attached. [c]0 and 1 indicate HOMO and LUMO, respectively. –1, –2, ..., -4 correspond to HOMO-1, HOMO-2, …, HOMO-4, respectively while 2 and 3 represent LUMO+1 and LUMO+2, respectively.

(3) Steady State Absorption Spectrum.

The UV-vis absorption spectrum of ImQ_T is depicted in Figure 3. The spectral feature resembles that of TQ_T benchmark; major MLCT bands appear in the visible region with λ_{max} value of 477 nm and, importantly, there was no MQCT signature. Further examination using TD-DFT method demonstrates the nature of the electronic transitions of the absorption spectra. We calculated fifty singlet excited states and lower energy transitions (S_1-S_{19}) are listed in Table 3. These transitions (S_1-S_{17}) are

co-plotted with the experimentally obtained results (Figure 3). Due to the intrinsic under-estimation of excited state energies by solvation-corrected TD-DFT calculation, we multiplied a correction factor of 1.1 to the calculated values.

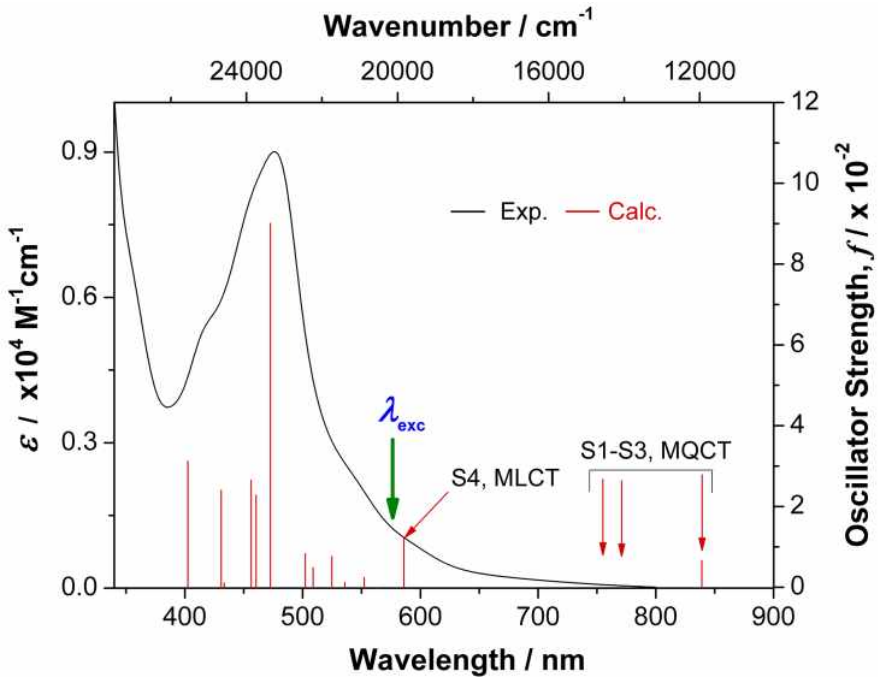

Figure 3. Steady state absorption spectra of ImQ_T in CH_3CN at 25 °C. Calculated transition energies and their corresponding oscillator strengths, *f*, of singlet → singlet transitions by TD-DFT method are depicted as vertical lines in wavenumber (top abscissa). MQCT transitions are emphasized by red arrows. The wavelength corresponding to the laser excitation (575 nm) is marked by green arrow. Note that the S_4 state having MLCT in character is expected to reside near λ_{exc}. The abscissa on top was shifted to its value multiplied by 1.1 to match with the experimental spectrum.

Table 3. Compositions of the CT-state wave functions of ImQ_T in terms of the linear combination coefficients in the configuration expansion.[a]

State	Energy		f^b	Wavefunction	Character	Transition Dipole Moment		
h^b	eV	cm^{-1}				au		
						x	y	z
S1	1.479	11932	0.0069	$0.7049\Psi_{0\to1}$	MQCT	-0.4287	0.0358	0.0749
S2	1.742	14046	0.0006	$0.1470\Psi_{-2\to1} + 0.6905\Psi_{-1\to1}$	MQCT	-0.1084	0.0349	-0.0182
S3	1.809	14588	0.0003	$0.6905\Psi_{-2\to1} + 0.1476\Psi_{-1\to1}$	MQCT	-0.0797	0.0280	-0.0215
S4	2.457	19817	0.0127	$0.1154\Psi_{-2\to2} + 0.6774\Psi_{0\to2}$	MLCT	-0.0106	-0.4445	0.1182
S5	2.543	20506	0.0001	$0.6771\Psi_{-6\to1} - 0.1010\Psi_{-5\to1} + 0.1458\Psi_{-3\to1}$	π-π* + MQCT	-0.0455	0.0023	0.0160
S6	2.587	20866	0.0027	$-0.2190\Psi_{-2\to2} 0.6401\Psi_{-1\to2} + 0.1344\Psi_{-1\to3}$	MLCT	0.1499	-0.0374	0.1361
S7	2.651	21380	0.0014	$-0.1205\Psi_{-9\to1} - 0.1102\Psi_{-8\to1} + 0.3248\Psi_{-7\to1}$	π-π* + MQCT	-0.1136	0.0254	0.0922
				$0.3709\Psi_{-5\to1} - 0.1060\Psi_{-4\to1} + 0.4567\Psi_{-3\to1}$				
S8	2.693	21721	0.0079	$-0.1304\Psi_{0\to2} + 0.5945\Psi_{0\to3} - 0.3247\Psi_{0\to4}$	MLCT	-0.2670	-0.0226	0.2185
S9	2.755	22219	0.0051	$0.1040\Psi_{-9\to1} - 0.3061\Psi_{-7\to1} - 0.1468\Psi_{-6\to1}$	π-π* + MQCT + MLCT	-0.2703	0.0310	0.0397
				$-0.2730\Psi_{-5\to1} + 0.5066\Psi_{-3\to1} - 0.1293\Psi_{0\to4}$				
S10	2.780	22423	0.0086	$-0.1003\Psi_{-7\to1} + 0.3645\Psi_{-2\to2} + 0.1227\Psi_{-1\to2}$	π-π* + MQCT + MLCT	0.2516	-0.2065	0.1447
				$0.2405\Psi_{0\to3} + 0.5053\Psi_{0\to4}$				
S11	2.895	23345	0.0904	$0.4251\Psi_{-2\to2} + 0.1937\Psi_{-1\to2} - 0.1095\Psi_{-1\to3}$	MLCT	0.9344	0.6321	0.0534
				$0.3604\Psi_{-1\to4} - 0.2245\Psi_{0\to3} - 0.2610\Psi_{0\to4}$				
S12	2.942	23727	0.0231	$0.5535\Psi_{-2\to3} - 0.3421\Psi_{-2\to4} + 0.1009\Psi_{-1\to2}$	MLCT	0.5332	0.1827	-0.0477
				$-0.2159\Psi_{-1\to3}$				
S13	2.958	23856	0.0268	$0.1081\Psi_{-2\to3} - 0.1599\Psi_{-2\to4} + 0.5963\Psi_{-1\to3}$	MLCT	-0.6034	-0.0521	-0.0584
				$0.2973\Psi_{-1\to4}$				
S14	2.988	24102	0.0002	$-0.1123\Psi_{-9\to1} - 0.1075\Psi_{-8\to1} + 0.3312\Psi_{-7\to1}$	π-π* + MQCT	-0.0325	-0.0211	-0.0244
				$-0.2170\Psi_{-5\to1} + 0.5569\Psi_{-4\to1}$				
S15	3.047	24572	0.0013	$0.1020\Psi_{-9\to1} - 0.2842\Psi_{-7\to1} + 0.4625\Psi_{-5\to1}$	π-π* + MQCT	0.0308	0.1295	-0.0055
				$0.4005\Psi_{-4\to1}$				
S16	3.056	24650	0.0243	$0.3929\Psi_{-2\to3} + 0.5422\Psi_{-2\to4} + 0.1144\Psi_{-1\to3}$	MLCT	-0.3328	0.3858	-0.2546
S17	3.166	25533	0.0315	$-0.2898\Psi_{-2\to2} + 0.1902\Psi_{-2\to4} - 0.1893\Psi_{-1\to3}$	MLCT	0.1754	-0.1703	-0.5890
				$0.4909\Psi_{-1\to4} + 0.1045\Psi_{0\to3} + 0.1819\Psi_{0\to4}$				
S18	3.505	28268	0.0023	$-0.1319\Psi_{-10\to1} + 0.5077\Psi_{-9\to1} - 0.4594\Psi_{-8\to1}$	π-π* + MQCT	0.1407	-0.0046	0.0807
S19	3.578	28854	0.0008	$0.1973\Psi_{-2\to11} + 0.1811\Psi_{-2\to12} - 0.1264\Psi_{-1\to5}$	MLCT	0.0020	-0.0884	-0.0399

$-0.2499\Psi_{-1\rightarrow 11} - 0.3073\Psi_{-1\rightarrow 12} - 0.1035\Psi_{-1\rightarrow 15}$
$0.1667\Psi_{0\rightarrow 5} + 0.3148\Psi_{0\rightarrow 11} + 0.2263\Psi_{0\rightarrow 12}$

[a]Subscripts correspond to the following orbitals: The highest occupied orbitals have index 0, i.e. 0 = HOMO, while all other occupied orbitals have index -1, -2. …, -n, which correspond to HOMO-1, HOMO-2, …, HOMO-n, respectively. LUMO = 1, LUMO+1 = 2, LUMO+2 = 3, and so on. [b]Oscillator strength.

The calculation results are in good agreement with the experimental data as shown in Figure 3. However, similar to the case of TQ_T, the lowest energy MQCT bands corresponds to Ru based occupied orbitals-to-quinone absorption spectrum. The calculated oscillator strengths (*f*) of these transitions are 0.0069, 0.0006, and 0.0003 for S_1, S_2 and S_3, respectively. The latter two are negligible and thus unlikely to appear in the spectrum. However, 0.0069 of *f* value for the first one is substantial, which is big enough to show up in the spectrum. Nevertheless, this charge transfer band does not appear in the spectrum indicating that the direct optical transition to the Ru^+-Q^- charge separated state is not viable. It is important to note that the transition to the S_4 state has significantly large *f* value (0.0127), which gives rise to the lower energy tailing in the spectral envelope. Interestingly, the peak position corresponding to S_4 state predicted by TD-DFT calculation is at least 730 cm^{-1} separated from its closest neighbor, S_5 state. Moreover, this peak is actually the lowest energy absorption band observable in the experimentally determined absorption spectrum. Thus we choose this wavelength (575 nm) for the laser excitation in order to generate a genuine S_4 state as a reactant state for the photo-induced CS. The compositions of the S_4 state

wavefunction is listed in Table 3. All constituent single electron transitions are Ru-based occupied orbitals (HOMO and HOMO-2)-to-tpy-based virtual orbital (LUMO+1). LUMO+1 orbital has *ca*. 80% of electronic populations at tpy ligand. S_4 transition can thus be regarded as a Ru-to-tpy MLCT.

(4) Photo-induced Ultrafast Charge Separation and Thermal Charge Recombination Reaction Dynamics Probed by Vis-Pump/IR-probe Spectroscopy.

As shown in our previous report, the dynamics of photo-induced CS and thermal CR reaction can be best probed by the CO stretching mode of Q and Q^-.[21,44] The ground-state FTIR spectrum of the CO stretching mode of ImQ_T shows a clear absorption band at 1669 cm^{-1} (Figure 4). Upon electronic excitation at 575 nm in which low energy MLCT tailing prevails, the characteristic Q^- mode appeared at 1518 cm^{-1} instantly with concomitant bleaching at 1669 cm^{-1} (Figure 4). The correlation between transient absorption and bleaching was confirmed by their time-resolved kinetic behaviors (Figure 5). It is important to note that the rise of Q^- mode CO stretching band was too fast to monitor precisely and was beyond our detection limit. Thus we only fit the kinetics of decay component. Contrary to the TQ_T case, the decay kinetics cannot be fitted by the monoexponential function described by eq. 1; only by using a biexponential function could the data be satisfactorily modeled (eq. 2).

$$CS(t) = A_0 + A_1 \exp(-t/\tau_1) \qquad \text{(eq.1)}$$

$$CS(t) = A_0 + A_1 \exp(-t/\tau_1) + A_2 \exp(-t/\tau_2) \qquad \text{(eq.2)}$$

The fitting parameters of TrIR decay kinetics of Q^- mode were $\tau_1 = 1.3 \pm 0.5$ ps with $A_1 = 1.33$ and $\tau_2 = 10.8 \pm 1.1$ ps with $A_2 = 6.72$. Those of Q mode gave $\tau_1 = 3.3 \pm 0.5$ ps with $A_1 = -1.65$ and $\tau_2 = 13.7 \pm 0.9$ ps with $A_2 = -4.47$, which are close to those of Q^- mode kinetics. Therefore, two transient IR band at 1669 and 1518 cm^{-1} can be assigned to the CO stretching mode of ground and CT states, respectively. The background of the biexponential decay kinetics is not clear at this time. We suggest two scenarios: One is that the fast component is for the vibrational relaxation at the CS state and the slower one is for the charge recombination process. Another one is the charge recombination for the fast component and the vibrational relaxation from the hot ground state for the slow component.

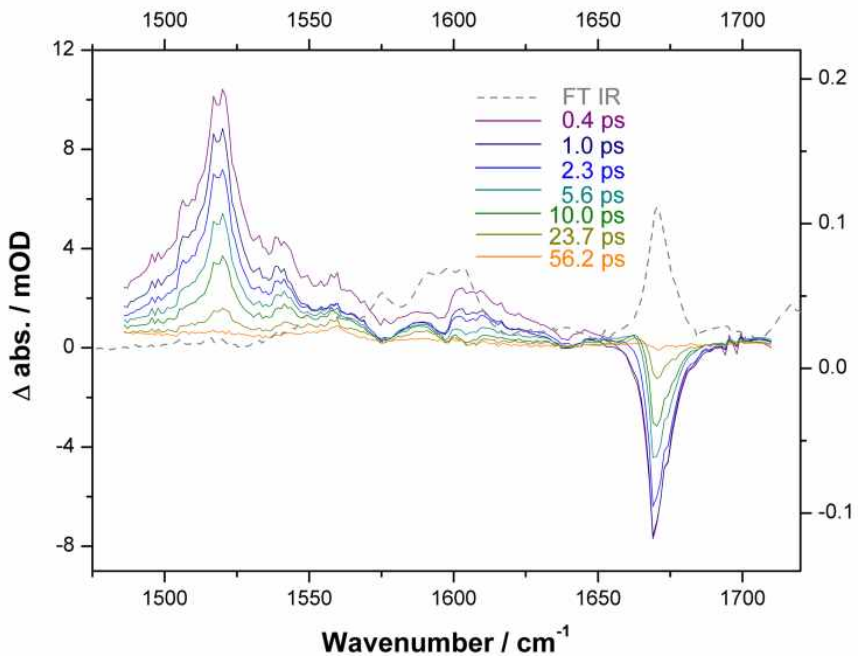

Figure 4. TrIR spectra of ImQ_T. FTIR spectra are shown in dotted lines (grey). Experimental conditions: λ_{ex} = 575 nm, solvent = CD_3CN. Temp = 23 ± 1 °C.

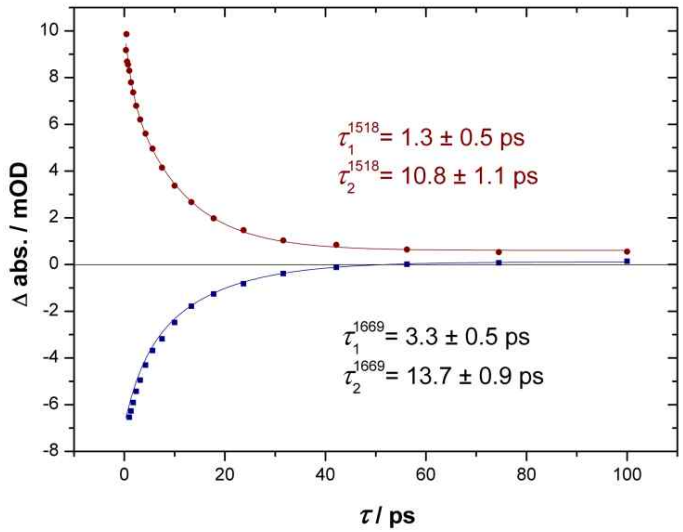

Figure 5. Decay kinetics of Q^- (top) and Q (bottom) CO stretching mode. Experimental conditions: λ_{ex} = 575 nm, solvent = CD_3CN. Temp = 23 ± 1 °C.

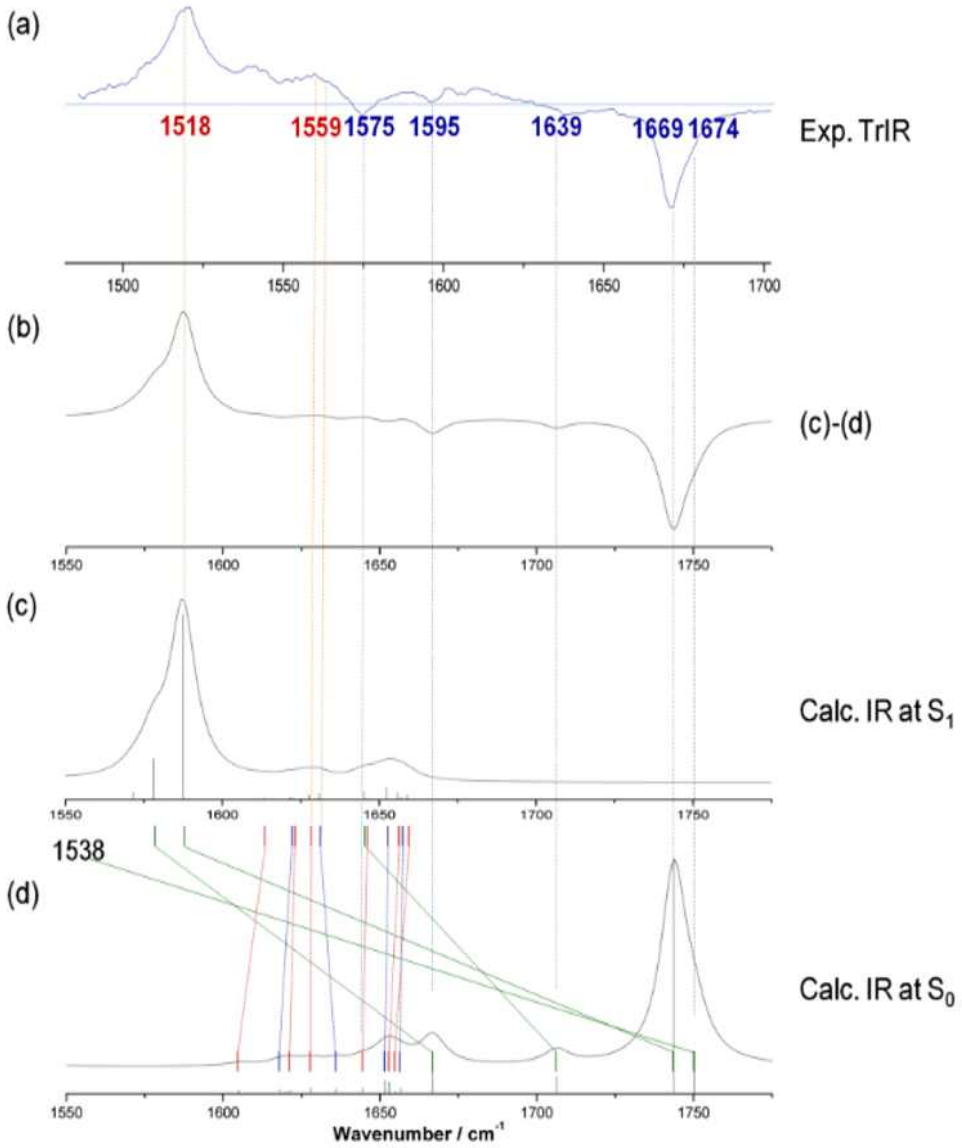

Figure 6-1. Experimental (a) and simulated by TD-DFT calculation (b) TrIR spectra. Simulated S_1 (c) and S_0 (d) state vibrational spectra. Spectrum on (b) was obtained by (c)-(d). Peak positions are guided by blue (bleaching) and orange (transient absorption) dotted lines. Correlations of vibrational modes are connected by green (Q), red (tpy), and blue (bpy) lines..

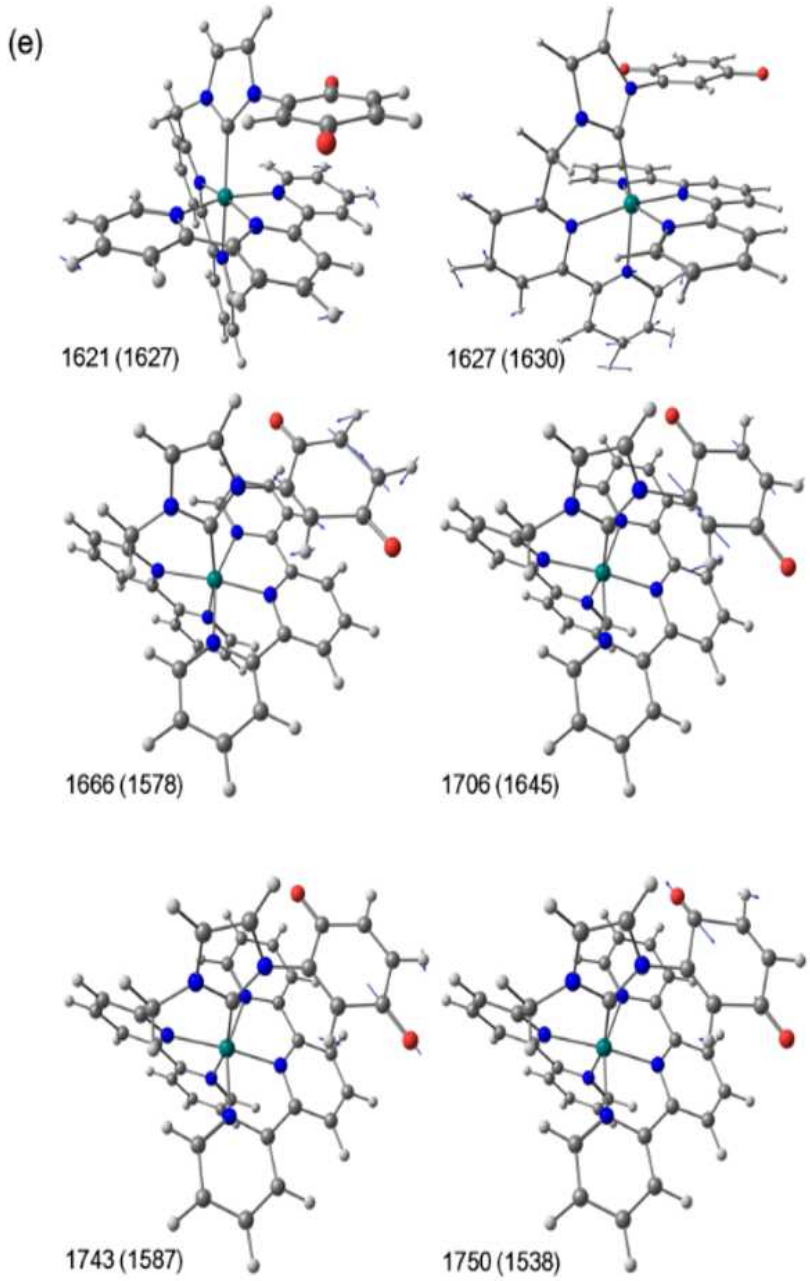

Figure 6-2. Blue Representative vibrational modes are illustrated in (e) with vibrational vectors in blue arrows

In order to analyze TrIR spectrum as well as the electron transfer dynamics further, we calculated vibrational frequencies of both ground- and CS states (S_0 and S_1). In order to reproduce a ground state vibrational spectrum, we performed frequency calculation based on the optimized geometry of ground state by using DFT method. For the spectrum of S_1 state, vibrational frequencies were calculated with the geometry optimized at S_1 state by using TD-DFT method. Simulated vibrational spectra for the S_0 (d) and S_1 (c) with each peak being convoluted with Gaussian function are shown in Figure 6. Full-widths at half maximum (FWHM) of each peak are equally assumed to be 5 cm^{-1}. The difference spectrum of two states (S_1-S_0) (b) is compared with the experimental TrIR spectrum at 1 ps time delay (a). Vibrational modes of representative peaks are illustrated in Figure 6(e). The experimental and simulated spectra are in excellent agreement with the latter being shifted to the red by *ca*. 75 cm^{-1}. With these well matched spectra, we could analyze the experimental TrIR spectrum in more detail.

Two CO stretching modes are predicted to appear at 1743 (asymmetric) and 1750 (symmetric) cm^{-1} with the former having much higher intensity. These two modes were shown in the experimental IR spectrum at 1669 and 1674 cm^{-1} (as a shoulder), respectively. These bands were bleached upon laser excitation at the same positions. In S_1 state, these two stretching modes are shifted to 1587 and 1538 cm^{-1}, respectively. The intense transient absorption appeared at 1518 cm^{-1} in the experimental TrIR spectrum corresponds to the former. The aromatic C-C stretching modes of Q are predicted to appear at 1706 (symmetric) and 1666 (asymmetric) cm^{-1} in the ground

state and 1645 and 1578 cm^{-1} in the S_1 state. In the experimental TrIR spectrum, these two bands were observed as weak bleaches at 1639 and 1595 cm^{-1}, respectively. Transient absorption peaks corresponding to these modes were not exhibited clearly. The fingerprints corresponding to the aromatic stretching modes of the ligands are broadly distributed in the 1610~1660 cm^{-1} region in the simulated spectrum. Among these, notable bands are at 1621 and 1627 cm^{-1} for the stretching modes of tpy and bpy, respectively, which were slightly shifted to the blue in the S_1 state; 1627 cm^{-1} for the former and 1630 for the latter. In the experimental TrIR spectrum, a moderately intense broad transient absorption was monitored at ~1559 cm^{-1}. Given the fact that the excitation wavelength was 575 nm, which corresponds to the Ru-to-tpy MLCT, the origin of such a transient absorption stems most likely from stretching mode of tpy.

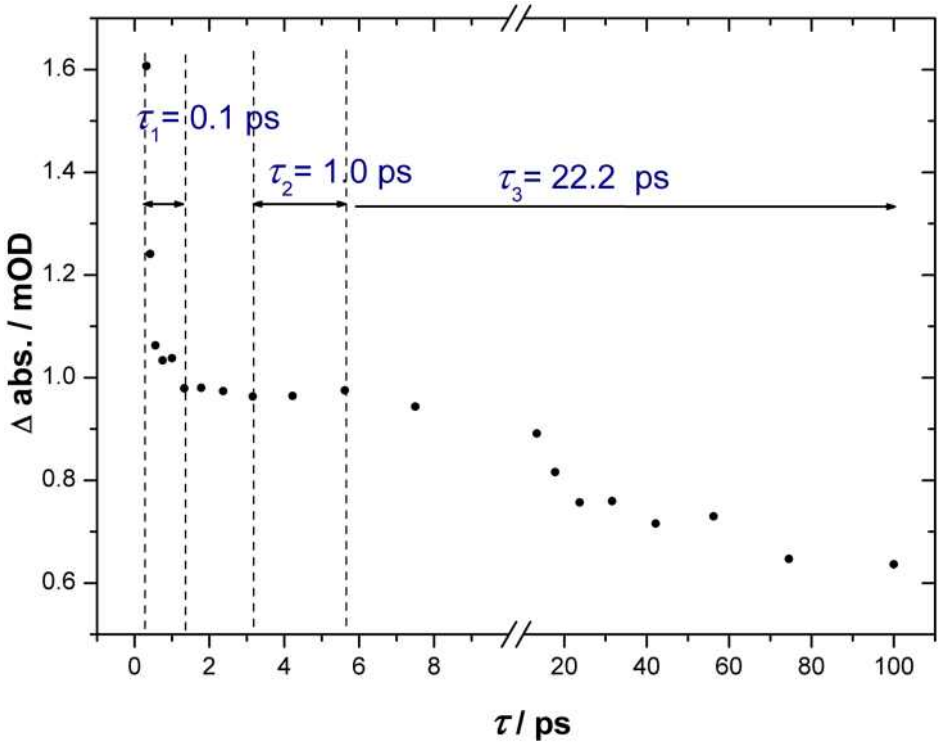

Figure 7. Decay kinetics at 1559 cm^{-1}. Experimental conditions: λ_{ex} = 575 nm, solvent = CD_3CN. Temp = 23 ± 1 °C.

Figure 7 displays a kinetic profile probed at 1559 cm^{-1}. The kinetic trace cannot be fitted with conventional multiexponential function. Thus we fitted the curve by three separate regions. In early time region up to 1 ps, transient absorption decays ultrafast with time constant of ~*ca*. 0.1 ps. The instrumental response function of our laser system is 180 fs. Thus the time constant of this decay cannot be measured precisely and 0.1 ps of time constant is only an estimate. However, it is obvious that transient absorption instantly generated upon laser excitation decays in ultrafast manner indicating that the tpy-located electronic population moves to other place very fast.

We tentatively attribute this component to the tpy-to-Q CS process. More specifically, it is the CS from the MLCT state to MQCT state. The reduced transient absorption peak stays for a while (~2 ps) and slightly rise again with time constant of ~1 ps indicating that the electronic population is rebuilt in the tpy ligand. The time constant of this process coincides with that of the fast component of the charge recombination process probed with Q and Q^- CO stretching modes. Therefore, it is reasonable to assign such a component as a CR process from Q to tpy ligand. Then the decay of transient absorption at longer period with 22 ps of time constant is thus a vibrational cooling in the ground state. This value is well agreement with the longer component of charge recombination process probed with Q and Q^- CO stretching mode.

The time constant of the vibrational cooling process estimated in this work is similar to that observed for the intramolecular CS and the following CR reaction in bis(η^5-cyclopentadienyl)molybdenum coordinated to an ene-1,2-dithiolatenaphthal-enetetracarboxylicdiimide ligand system.[45] Figure 8 displays the normalized spectra in the Q mode bleaching area, which clearly demonstrates the evidence of vibrational cooling. The initial peak position corresponding to the Q mode bleaching at 1669 cm^{-1} gradually blue-shifted with concomitant narrowing of the bandwidth. At 56.2 ps when the CR and the vibrational cooling processes are almost finished, the peak position was 1670.3 cm^{-1}, which was 1.3 cm^{-1} blue-shifted from its original position. This result is surprising because the time scale of CR reaction in TQ_T system was estimated to be ~20 ps. It was not clear whether such a time scale is for the sole CR reaction or for the processes including CR and vibrational cooling. However, the

analysis of electron transfer dynamics with ImQ_T system clearly reveals that the CR reaction takes only 1-3 ps followed by 10-20 ps of vibraitional cooling process.

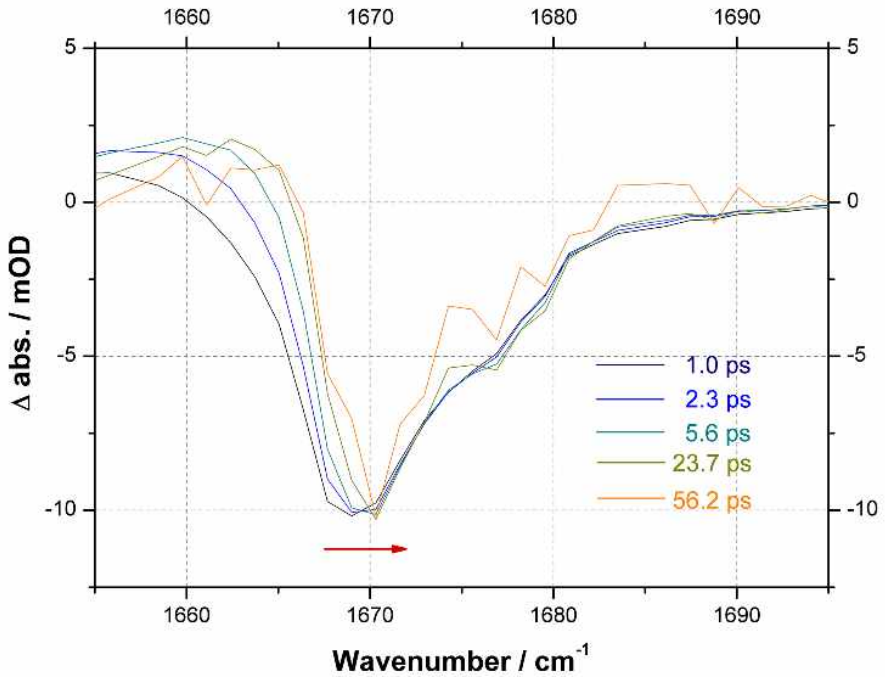

Figure 8. Decay kinetics at 1669 cm^{-1}. Experimental conditions: λ_{ex} = 575 nm, solvent = CD_3CN. Temp = 23 ± 1 °C.

In conclusion, a new D-A system, ImQ_T, in which $[Ru(tpy)(NHC)]^{2+}$ donor and quinone acceptor are juxtaposed in a van-der-Waals contact has been synthesized and characterized. The ground- and excited-state electronic structures were determined by both spectroscopic and electrochemical method and were further confirmed by theoretical calculation by using DFT and TD-DFT method. The photo-induced charge

separation and thermal charge recombination reactions were probed by ultrafast visible-pump/mid-IR-probe spectroscopic method. The transient IR absorption spectrum was analysed by the aid of ground- and excited state frequency calculation. Selective excitation to tpy-localized MLCT state gives rise to the ultrafast charge separation through π-stacked manifold. The time scale of the CS reaction could not be determined precisely and the estimated value is *ca*. 0.1 ps. Thermal CR reaction takes place within 1-3 ps range and the following vibrational cooling process takes 10-20 ps. This work demonstrates that the intramolecular photo-induced CS reaction can take place via π-stacked manifold of van der Waals contact in ultrafast manner. Detailed time constant of CS, CR and vibrational cooling processes were also determined.

3. Experimental

All reactions were carried out under a nitrogen atmosphere unless otherwise noted. Standard Schlenk techniques were employed to manipulate air-sensitive solutions, while workup procedures were done in air. Tetrahydrofuran (THF) were purchased from Fischer Scientific (HPLC grade) and dried over Na/benzophenone and were subsequently distilled under nitrogen prior to use. Acetone (Kanto, HPLC) and acetonitrile (Samchun, 99.5%) were distilled over CaH_2 prior to use. Methanol (Fischer Scientific, absolute), ethylene glycol (Aldrich) and hydrobromic acid (Samchun, 48 wt%) were used without further purification. Imidazole (99%), 2,5-dimethoxyphenylboronic acid, 2-hydroxy-6-methylpyridine (97%), *n*-butyllithium solution (2.5 M in hexane), diisopropylamine, trifluoromethanesulfonic anhydride (99%), chlorotrimethylsilane (97%), hexachloroethane (99%), copper(II) acetate (98%), lithium chloride, 2,2':6',2''-terpyridine (98%), ammonium hexafluorophosphate (NH_4PF_6) and 2,3-dichloro-5,6-dicyano-p-benzoquinone (DDQ) were purchased from Aldrich Chemical Co. Tetrakis(triphenylphosphine)palladium(0) was purchased from Pressure Chemical Co. Sodium bicarbonate (98%) was purchased from Samchun Chemical Co. 6-Chloromethyl-2,2'-bipyridine[23] and (2,2':6',2''-tepyridine)(trichloro)Ru (III) ($Ru(tpy)Cl_3$)[24] were prepared according to literature procedures. Column chromatography was performed on silica gel 60 (230-400 Mesh, Merck).

^1H and ^{13}C NMR spectra were recorded with Bruker (75 MHz for ^{13}C NMR), Agilent (400 MHz and 100 MHz for ^1H and ^{13}C NMR, respectively) and Agilent (500

MHz and 125 MHz for ^{1}H and ^{13}C NMR, respectively) spectrometers. ^{1}H NMR spectra were taken in $CDCl_3$ and DMSO-d_6 and were referenced to residual $CDCl_3$ (7.26 ppm) and DMSO-d_6 (2.50 ppm), respectively. Chemical shifts of the ^{13}C NMR spectra were measured relative to $CDCl_3$ (77.16 ppm) or DMSO-d_6 (39.52). High-resolution mass spectrometry (HRMS) data were obtained at the Korea Basic Science Institute (Daegu). Electronic absorption spectra were recorded on a Beckman Du-650 spectrophotometer. Cyclic voltammograms were obtained with a CH Instrument voltammetric analyzer. Measurements were performed after the acetonitrile (spectroscopic grade) solution was purged with dry nitrogen gas for 30 min. The supporting electrolyte was 0.1 M tetrabutylammonium hexafluorophosphate ($TBAPF_6$). Glassy carbon and Ag/Ag^{+} (0.01M $AgNO_3$) were used as working and reference electrodes, respectively. The scan rate was maintained at 100 mV/s.

Synthesis

1-(2,5-Dimethoxyphenyl)-1*H*-imidazole (1): Imidazole (0.68 g, 10 mmol) and 2,5-dimethoxyphenylboronic acid (2.18 g, 12 mmol) were added to a solution of copper(II) acetate (0.15 g, 8 mol%) in 20 mL methanol and the mixture was allowed to stirred at 65℃ for 36 h under an oxygen atmosphere. The reaction mixture was concentrated by rotary evaporation and extracted with dichloromethane. Purification of the resulting residue by silica-gel chromatography (dichloromethane:methanol = 24:1) provided orange oil. (Yield: 82 %, 1.68 g) ^{1}H NMR (500 MHz, $CDCl_3$) δ 7.74 (s, 1 H), 7.16 (s, 1 H), 7.10 (s, 1 H), 6.92 (d, J = 8.8 Hz, 1 H), 6.83 – 6.79 (m, 2 H), 3.73

(s, 3 H), 3.71 (s, 3 H); ^{13}C NMR (125 MHz, $CDCl_3$) δ 153.7, 146.5, 137.7, 128.8, 127.0, 120.1, 113.6, 113.1, 111.7, 56.4, 55.8; HRMS(FAB+), *m/z* $[M+H]^+$ found (calc): 205.0976 (205.0977).

2-(1*H*-imidazol-1-yl)benzene-1,4-diol (2): To a schlenk flask containing 1 (1.02 g, 5 mmol), 30 mL of 48 wt% hydrobromic acid was added. The reaction mixture was refluxed overnight. The solvent was removed by distillation and concentrated to 5 mL. Solid $NaHCO_3$ was added until the solution was neutralized. Precipitate was filtered and dissolved with methanol. Purification of the resulting residue by silica-gel chromatography (dichloromethane:methanol = 15:1) gave white solid. (Yield: 94 %, 0.82 g) ^{1}H NMR (400 MHz, DMSO) δ 9.42 (br, 2 H), 7.95 (s, 1 H), 7.43 (t, J = 1.2 Hz, 1 H), 7.04 (s, 1 H), 6.89 (d, J = 8.7 Hz, 1 H), 6.74 (d, J = 2.8 Hz, 1 H), 6.67 (dd, J = 8.7, 2.8 Hz, 1 H); ^{13}C NMR (100 MHz, DMSO) δ 150.3, 142.5, 137.4, 128.0, 124.9, 120.3, 117.8, 115.1, 111.7; HRMS(FAB+), *m/z* $[M+H]^+$ found (calc): 177.0665 (177.0664).

1-([2,2'-Bipyridine]-6-yl-methyl)-3-(2,5-dihydroxyphenyl)-1*H*-imidazol-3-ium chloride (3): A solution of 2 (0.35 g, 2.0 mmol) and 6-(chloromethyl)-2,2'-bipyridine (0.49 g, 2.4 mmol) in 10 mL of acetonitrile was refluxed for 36 h. After cooling to room temperature, solvent was removed by rotary evaporator. Resulting solid was dissolved by minimum amount of dichloromethane and dropped to 100 mL of diethyl

ether and stirred for 30 min. White precipitate was filtered and dried. (Yield: 92%, 0.70 g) ^{1}H NMR (400 MHz, DMSO) δ 10.31 (s, 1 H), 9.80 (s, 1 H), 9.56 (s, 1 H), 8.70 – 8.66 (m, 1 H), 8.37 (d, J = 7.9 Hz, 1 H), 8.24 (d, J = 7.9 Hz, 1 H), 8.10 (s, 1 H), 8.05 (dd, J = 8.9, 6.7 Hz, 2 H), 7.96 (td, J = 7.6, 1.2 Hz, 1 H), 7.60 (d, J = 7.7 Hz, 1 H), 7.46 (dd, J = 7.5, 4.8 Hz, 1 H), 7.08 (d, J = 8.8 Hz, 1 H), 6.96 (d, J = 2.7 Hz, 1 H), 6.88 (dd, J = 8.8, 2.4 Hz, 1 H), 5.78 (s, 2 H); ^{13}C NMR (100 MHz, DMSO) δ 155.0, 154.5, 153.1, 150.3, 149.4, 143.0, 138.7, 138.1, 137.5, 124.5, 123.4, 123.1, 122.5, 122.1, 120.6, 120.0, 118.0, 117.9, 112.0, 53.1; HRMS(FAB+), *m/z* $[M]^{+}$ found (calc): 345.1353 (345.1352).

[Ru(1-([2,2'-Bipyridine]-6-yl-methyl)-3-(2,5-dihydroxyphenyl)-1*H*-imidazole)(2,2':6',2"-terpyridine)][PF_6]$_2$ ($ImQH_2$_T, 4): A mixture of Ru(tpy)Cl_3 (132 mg, 0.3 mmol) and 3 (114 mg, 0.3 mmol) in 5 mL of ethylene glycol was heated at 160 ℃ for 4 h. The reaction mixture was allowed to cool slowly to room temperature. The solution was dropped to a saturated NH_4PF_6 aqueous solution. The brown precipitate was filtered and purified with silica-gel column chromatography. Elution with CH_3CN/0.5 M $NaNO_3$ (9:1) gave a product as an orange band. The collected orange band was concentrated to ca. 5 mL and was triturated in a saturated NH_4PF_6 aqueous solution. The precipitated orange solid was filtered and washed several times with ether, water and dried in vacuo. (Yield: 69%, 200 mg) ^{1}H NMR (400 MHz, DMSO) δ 8.90 (d, J = 8.0 Hz, 1 H), 8.81 (s, 1 H, –OH), 8.68 (d, J = 8.2 Hz, 1 H), 8.50 (s, 1 H, –OH), 8.47 – 8.38 (m, 5 H), 8.18 (d, J = 7.8 Hz, 1 H), 8.05 –

7.88 (m, 4 H), 7.76 (d, *J* = 5.2 Hz, 1 H), 7.65 (d, *J* = 1.8 Hz, 1 H), 7.54 (d, *J* = 5.3 Hz, 1 H), 7.32 – 7.23 (m, 3 H), 6.91 (d, *J* = 1.8 Hz, 1 H), 6.68 (d, *J* = 5.1 Hz, 1 H), 6.48 (dd, *J* = 8.8, 2.9 Hz, 1 H), 6.24 (d, *J* = 8.8 Hz, 1 H), 6.04 (d, *J* = 3.2 Hz, 2 H), 5.18 (d, *J* = 2.8 Hz, 1 H); ^{13}C NMR (100 MHz, DMSO) δ 178.6, 158.3, 157.9, 157.2, 155.9, 155.4, 155.3, 154.7, 153.3, 152.4, 149.1, 147.2, 145.2, 137.7, 137.7, 137.5, 137.4, 134.5, 127.5, 127.1, 127.1, 126.3, 125.7, 124.8, 123.8, 123.7, 123.5, 123.5, 123.4, 123.0, 122.6, 117.4, 116.2, 113.5, 53.5; HRMS(FAB+), *m/z* $[M+PF_6]^+$ found (calc): 824.0914 (824.0921).

[Ru(1-([2,2'-Bipyridine]-6-yl-methyl)-3-(2-cyclohexa-2',5'-diene-1,4-dionyl)-1*H*-imidazole)(2,2':6',2"-terpyridine)] $[PF_6]_2$ (ImQ_T, 5): 4 (145 mg, 0.15 mmol) and 10 equivalents of DDQ (0.34 g) were dissolved in 10 mL of distilled acetone and stirred under nitrogen for 12 h. The solution was dropped to 100 mL of diethyl ether. Brown solids were filtered and washed with diethyl ether several times. (Yield: Quantitative) ^{1}H NMR (400 MHz, DMSO) δ 8.93 (d, *J* = 8.0 Hz, 1 H), 8.77 (d, *J* = 8.1 Hz, 1 H), 8.69 (dd, *J* = 16.6, 8.1 Hz, 3 H), 8.47 (dd, *J* = 17.2, 8.3 Hz, 2 H), 8.18 (dd, *J* = 13.4, 7.7 Hz, 2 H), 8.05 (t, *J* = 7.8 Hz, 1 H), 7.95 (t, *J* = 7.2 Hz, 3 H), 7.70 (s, 1 H), 7.45 (d, *J* = 5.4 Hz, 1 H), 7.37 (t, *J* = 8.0 Hz, 1 H), 7.31 (t, *J* = 8.0 Hz, 1 H), 7.26 (t, *J* = 8.0 Hz, 1 H), 7.07 (s, 1 H), 6.86 (dd, *J* = 10.2, 2.3 Hz, 1 H), 6.79 (d, *J* = 5.1 Hz, 1 H), 6.63 (d, *J* = 10.2 Hz, 1 H), 6.20 (d, *J* = 2.4 Hz, 1 H), 6.05 (dd, *J* = 54.6, 16.3 Hz, 2 H); ^{13}C NMR (100 MHz, DMSO) δ 187.1, 180.2, 179.4, 157.8, 157.5, 157.1, 157.0, 156.9, 156.0, 155.0, 154.3, 153.2, 147.9, 142.4, 138.6, 138.6, 138.2,

137.2, 136.3, 136.2, 132.3, 128.8, 128.4, 127.7, 126.9, 125.0, 125.0, 124.8, 124.5, 124.3, 124.2, 124.1, 124.1, 124.0, 53.8; HRMS(FAB+), *m/z* $[M+H]^+$ found (calc): 678.1190 (678.1201).

Pump-Probe Transient Absorption Spectroscopic Measurements. The details of the time-resolved vibrational spectrometer are described elsewhere.[25-27] Briefly, two identical home-built optical parametric amplifiers (OPAs), pumped by a commercial Ti:sapphire regenerative amplifier (Hurricane, Spectra Physics) with a repetition rate of 1 kHz, are used to generate a visible pump pulse and a mid-IR probe pulse. Pump pulse at 575 nm with 3.0 μJ of energy was generated by frequency doubling of a signal pulse of one OPA. Tunable mid-IR probe pulse was generated by difference frequency mixing of the signal and idler pulse of the other OPAs. The polarization of the pump pulse was set at the magic angle (54.7°) relative to the probe pulse to recover the isotropic absorption spectrum. The broadband transmitted probe pulse was detected with a 64-elements $N_2(l)$-cooled HgCdTe array detector. The array detector is mounted in the focal plane of a 320 mm monochromator with a 120 *l*/*mm* grating, resulting in a spectral resolution of ca. 1.3 cm^{-1}/pixel at 1600 cm^{-1}. The signals from each of the detector elements were amplified with a homebuilt 64-channel amplifier and digitized by a 12-bit analog-to-digital converter. Chopping the pump pulse at half the repetition frequency of the laser and computing the difference between the pumped and the unpumped absorbance determine the pump-induced change in the absorbance of the sample, ΔA. Due to the excellent short-term stability

of the IR light source (< 0.5% rms), less than 1×10^{-4} rms in absorbance units after 0.5 sec of signal averaging is routinely obtained without single shot referencing with an independent detector. The pump spot was made sufficiently larger than the probe spot to ensure spatially uniform photoexcitation across the spatial dimensions of the probe pulse. The instrument response function was typically 180 fs.

Computational Method. All calculations were performed using the Gaussian 09 program package.[28] All the results were obtained using a spin-restricted formalism at the DFT level of theory[29-33] using the B3LYP hybrid functional.[34] The ruthenium atom was described by using the LANL2DZ basis set, which includes the relativistic effective core potential (ECP) of Hay and Wadt[35,36] for the inner electrons and a double-ζ basis set for the outer electrons. The standard 6-31G(d) basis set[37] was used for the remaining atoms. All geometry optimization procedure was done without any symmetry restriction. Frequency calculations were performed to extract the IR frequencies and intensities with the optimized geometries of both ground- and S_1 excited-states. The excitation energies and oscillator strengths at the optimized geometry in the ground state are obtained by TD-DFT calculations with the same basis sets as those for the ground state.[38,39]

4. Reference

(1) Alstrum-Acevedo, J. H.; Brennaman, M. K.; Meyer, T. J. *Inorg. Chem.* **2005**, *44*, 6802.

(2) Wasielewski, M. R. *J. Org. Chem.* **2006**, *71*, 5051.

(3) Gust, D.; Moore, T. A.; Moore, A. L. *Acc. Chem. Res.* **2009**, *42*, 1890.

(4) El-Khouly, M. E.; Ju, D. K.; Kay, K. Y.; D'Souza, F.; Fukuzumi, S. *Chem.-Eur. J.* **2010**, *16*, 6193.

(5) Fukuzumi, S.; Ohkubo, K.; Saito, K.; Kashiwagi, Y.; Khoury, T.; Crossley, M. J. *J. Porphyr. Phthalocya.* **2011**, *15*, 1292.

(6) Bottari, G.; Trukhina, O.; Ince, M.; Torres, T. *Coord. Chem. Rev.* **2012**, *256*, 2453.

(7) Concepcion, J. J.; House, R. L.; Papanikolas, J. M.; Meyer, T. J. *Proc. Natl. Acad. Sci.* **2012**, *109*, 15560.

(8) Feng, L.; Rudolf, M.; Wolfrum, S.; Troeger, A.; Slanina, Z.; Akasaka, T.; Nagase, S.; Martín, N.; Ameri, T.; Brabec, C. J.; Guldi, D. M. *J. Am. Chem. Soc.* **2012**, *134*, 12190.

(9) Happ, B.; Winter, A.; Hager, M. D.; Schubert, U. S. *Chem. Soc. Rev.* **2012**, *41*, 2222.

(10) Frischmann, P. D.; Mahata, K.; Wűrthner, F. *Chem. Soc. Rev.* **2013**, *42*, 1847.

(11) The Photosynthetic Reaction Center; Academic: San Diego, 1993; Vol. Vol. II.

(12) Kluwer Academic Publishers: Dordrecht, The Netherlands., 1995.

(13) Springer Berlin-Heidelberg, 1996.

(14) Kirmaier, C.; Holten, D. *Photosynth. Res.* **1987**, *13*, 225.

(15) Breton, J.; Martin, J. L.; Fleming, G. R.; Lambry, J. C. *Biochemistry* **1988**, *27*, 8276.

(16) Holzapfel, W.; Finkele, U.; Kaiser, W.; Oesterhelt, D.; Scheer, H.; Stilz, H. U.; Zinth, W. *Chem. Phys. Lett.***1989**, *160*, 1.

(17) Kirmaier, C.; Gaul, D.; DeBey, R.; Holten, D.; Schenck, C. C. *Science* **1991**, *251*, 922.

(18) Heller, B. A.; Holten, D.; Kirmaier, C. *Science* **1995**, *269*, 940.

(19) Gray, H. B.; Winkler, J. R. **1996**; Vol. 65, p 537.

(20) Kirmaier, C.; Weems, D.; Holten, D. *Biochemistry* **1999**, *38*, 11516.

(21) Kim, H. M.; Park, J.; Lee, Y. T.; Lim, M.; Chung, Y. K.; Kang, Y. K. *J. Phys. Chem.* C **2011**, *115*, 22557.

(22) Kim, H. M.; D., J.; Noh, H. C.; Kang, Y. K.; Chung, Y. K. *Bull. Kor. Chem. Soc.* in press.

(23) Savage, S. A.; Smith, A. P.; Fraser, C. L. *J. Org. Chem.* **1998**, *63*, 10048.

(24) Sullivan, B. P.; Calvert, J. M.; Meyer, T. J. *Inorg. Chem.* **1980**, *19*, 1404.

(25) Kim, J.; Park, J.; Lee, T.; Lim, M. *J. Phys. Chem. B*. **2009**, *113*, 260.

(26) Lee, T.; Park, J.; Kim, J.; Joo, S.; Lim, M. *Bull. Kor. Chem. Soc.* **2009**, *30*, 177.

(27) Kim, S.; Jin, G.; Lim, M. J. Phys.Chem.B. **2004**, *108*, 20366.

(28) Frisch, M. J. e. a. Gaussian 03, Revision C.02; Gaussian, Inc.: Wallingford, CT, **2004**.

(29) Kohn, W.; Sham, L. *J. Phys. Rev*. **1965**, *140*, A1133.

(30) Becke, A. D. *Journal of Chemical Physics* **1993**, *98*, 5648.

(31) Stephens, P. J.; Devlin, F. J.; Chabalowski, C. F.; Frisch, M. J. *J. Phys. Chem.* **1994**, *98*, 11623.

(32) Hertwig, R. H.; Koch, W. *Chem. Phys. Lett*. **1997**, *268*, 345.

(33) Pietro, W. J.; Francl, M. M.; Hehre, W. J.; DeFrees, D. J.; Pople, J. A. *J. Am. Chem. Soc*. **1982**, *104*, 5039.

(34) Lee, C. T.; Yang, W. T.; Parr, R. G. *Physical Review B* **1988**, *37*, 785.

(35) Hay, P. J.; Wadt, W. R. *J. Chem. Phys.* **1985**, *82*, 299.

(36) Wadt, W. R.; Hay, P. J. *J. Chem. Phys.* **1985**, *82*, 284.

(37) Hehre, W. J.; Ditchfield, R.; Pople, J. A. *J. Chem. Phys*. **1972**, *56*, 2257.

(38) Bartolotti, L. J. *Physical Review A* **1982**, *26*, 2243.

(39) Runge, E.; Gross, E. K. U. *Phys. Rev. Lett.* **1984**, *52*, 997.

(40) Son, S. U.; Park, K. H.; Lee, Y. S.; Kim, B. Y.; Choi, C. H.; Lah, M. S.; Jang, Y. H.; Jang, D. J.; Chung, Y. K. *Inorg. Chem.* **2004**, *43*, 6896.

(41) Dinda, J.; Liatard, S.; Chauvin, J.; Jouvenot, D.; Loiseau, F. *Dalton Trans.* **2011**, *40*, 3683.

(42) Iovine, P. M.; Kellett, M. A.; Redmore, N. P.; Therien, M. J. *J. Am. Chem. Soc.* **2000**, *122*, 8717.

(43) Iovine, P. M.; Veglia, G.; Furst, G.; Therien, M. J. *J. Am. Chem. Soc.* **2001**, *123*, 5668.

(44) Rubtsov, I. V.; Kang, Y. K.; Redmore, N. P.; Allen, R. M.; Zheng, J. R.; Beratan, D. N.; Therien, M. J. *J. Am. Chem. Soc.* **2004**, *126*, 5022.

(45) Taylor, A. J.; Davies, E. S.; Weinstein, J. A.; Sazanovich, I. V.; Bouganov, O. V.; Tikhomirov, S. A.; Towrie, M.; McMaster, J.; Garner, C. D. *Inorg. Chem.* **2012**, *51*, 13181.

Part II.

Manipulation of Absorption Maxima by Controlling Oxidation Potentials in Bis(tridentate) Ru(II) *N*-Heterocyclic Carbene Complexes

1. Introduction

Manipulation of absorption maxima (λ_{max}) as well as oscillator strengths of light harvesting chromophores is crucial in solar energy conversion-related applications.[1] In many organic and inorganic systems, λ_{max} values are strongly correlated with HOMO and LUMO levels. Destabilization and stabilization of HOMO and LUMO, respectively, are common approaches to increase λ_{max} values. Such approaches can be applied to Ru(II) polypyridyl complexes, in which the nature of the electronic transitions in low energy region is characteristic of Ru-based occupied molecular orbitals (MOs)-to-ligand-based virtual MOs charge transfer (MLCT). A strategy for stabilizing virtual MOs includes expanding conjugation of the ligand or incorporating electron withdrawing groups to the periphery of the ligand. And one of the representative methods of destabilizing occupied MOs involves applying a strong ligand field.[2] Toward these ends, a huge numbers of new ligand systems that include N,[3] C,[4] or S[5] donor moiety have been developed in addition to the conventional polypyridyl ligands such as 2,2'-bipyridine (bpy) and 2,2';6'2"-terpyridine (tpy) derivatives.[6]

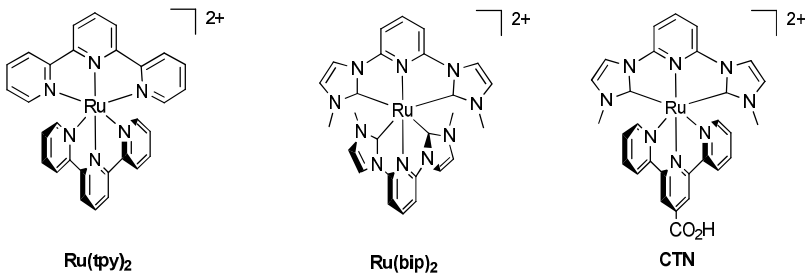

Scheme 1.

We have previously exploited *N*-heterocyclic carbene (NHC) compounds, 2-(3-methylimidazolium-1-yl)pyridine (mip) or 2,6-bis-(3-methylimidazolium-1-yl)pyridine (bip), as bidentate or tridentate ligands, respectively, for a new type of ruthenium chromophore.[7(a)] Electrochemical data as well as theoretical calculation data of $[Ru(bip)_2]^{2+}$, for example, indicate that HOMO of this complex is *ca.* 0.2 V more destabilized relative to that of $[Ru(tpy)_2]^{2+}$ benchmark, as intended to bring a strong ligand field. However, the degree of destabilization of LUMO is even larger due to a confined electronic delocalization within the pyridyl ring. When one bip ligand is replaced with 2,2';6'2"-terpyridine-4'-carboxylic acid (**CTN**, Scheme 1), the tpy-localized virtual orbital becomes the LUMO of the molecule, while a Ru-based occupied orbital whose energy is destabilized by the bip ligand still remains a HOMO.[7(b)] The λ_{max} value was brought back to visible region (463 nm). Dinda et al. reported that using 1,1'-[2,6-pyridinediylbis(methylene)]bis[3-methylimidazolyl] ligand to augment the ligand field gave rise to 0.44 and 0.24 V destabilization of HOMO levels for homoleptic $[RuL_2]^{2+}$ and heteroleptic $[Ru(tpy)L]^{2+}$ (L=1,1'-[2,6-pyridinediylbis(methylene)]-bis[3-methylimidazolyl]), respectively, relative to that of $[Ru(tpy)_2]^{2+}$.[8(a)] The λ_{max} values were 429 and 500 nm and molar extinction coefficient (ε) were 12000 and 5200 $M^{-1}cm^{-1}$, respectively. These results highlight the capacity of NHC compound as a versatile ligand for strong ligand field effects.

Although the heteroleptic approach mentioned above works for manipulating the λ_{max} values of Ru complexes to some extent, there is a need to find the factors that govern the λ_{max} values of Ru(NHC) complexes to exploit such systems further. Under

this background, combined with the lack of information regarding systematic structure-property relationships of Ru(NHC) systems, we have newly synthesized seven Ru complexes that possess a heteroleptic $[Ru(tpy)(NHC)]^{2+}$ or a homoleptic $[Ru(NHC)_2]^{2+}$ topology and feature NNC- or NN^C-type NHC structural motif (NN = bipyridyl, C = azolyl, and ^ = methylene). The structures of series complexes are shown in Scheme 2.

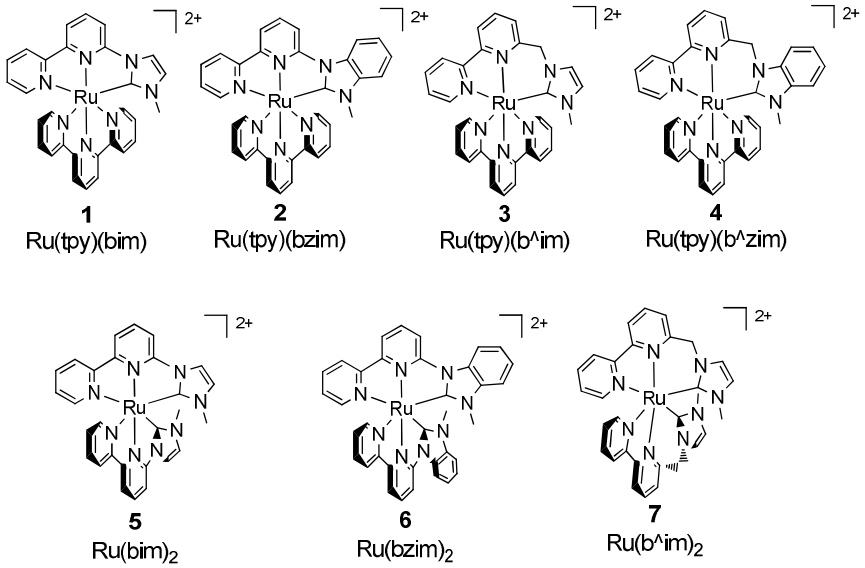

Scheme 2.

The synthesis of NNC- or NN^C-type ligands and their transition metal complexes have been reported in a handful of literature.[8] However, the background for employing such ligand systems to build a new series of Ru complexes deserves comments as follow; (1) NHC moiety is connected to bpy with or without a methylene bridge and thus lies at the corner of the tridentate ligand. Due to the presence of bpy

moiety in both NNC- and NN^C-type ligands, a minimum conjugation is ensured of at least up to two pyridyl rings. This structural motif prevents an ultimate destabilization of the unoccupied MO energy level derived from the confined electronic delocalization in the single pyridyl ring observed in the bip example.[7(a)] (2) The presence of the methylene bridge is manipulated to vary the strength of a ligand field induced by NHC moiety. With a methylene bridge, the $N_{pyridine}$-Ru-$C_{carbene}$ bite angle becomes near orthogonal, thus inducing an augmented ligand field.[8(a)] (3) Employing a benzimidazolyl group in place of a simple imidazolyl one has multi purposes; one of which is to reduce energy mismatch between bpy and NHC thus extends the conjugation over the entire ligand, and the other is to delicately tune the σ-donating power of the NHC moiety. And the last one is to increase the absorption intensity of the complex by increasing the light absorbing cross section.

During our analyses of experimental and theoretical calculation data of these series complexes, we found that λ_{max} values are strongly correlated to electrochemical oxidation potentials ($E_{1/2}^{2+/3+}$) rather than the commonly accepted HOMO-LUMO gaps. Here we communicate these results.

2. Result and Discussion

(1) Synthesis

The syntheses of NNC- and NN^C-type ligands are shown in Scheme 3 and 4, respectively. The synthesis of NNC-type ligands, 3-([2,2'-bipyridin]-6-yl)-1-methyl-1*H*-imidazol-3-ium hexafluorophosphate (bim) and 3-([2,2'-bipyridin]-6-yl)-1-methyl-1H-benzimidazol-3-ium hexafluorophosphate (bzi), was carried out via copper- catalyzed Ullmann coupling between 6-bromo-2,2'-bipyridine and imidazole or benzimidazole in DMF at 150°C followed by methylation with iodomethane in refluxing acetonitrile. The two-step reactions were facile and straightforward providing the desired NNC ligands (bim, bzim) in near quantitative yields. The reaction of 6-bromo-2,2'-bipyridine with excess amount of 1-methylimidazole or 1-methylbenzimidazole as solvents attempting to generate bim or bzim directly only gave products in poor yield (ca. 20%).

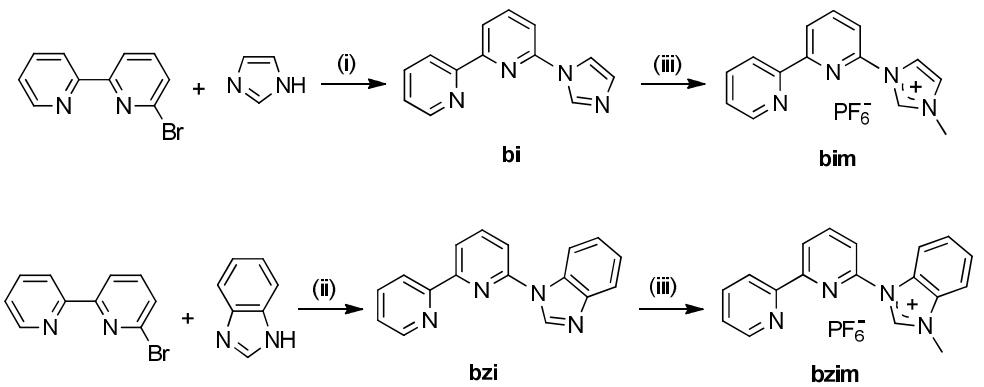

(i) 10 mol% CuO, 1.2 eq K_2CO_3, DMF, 150°C, 36h; (ii) 10 mol% CuO, 1.2 eq K_2CO_3, DMF, 150°C, 48h; (iii) CH_3I, CH_3CN, reflux, 4h, NH_4PF_6

Scheme 3. Synthesis of NNC ligands, **bim** and **bzim**

The synthesis of NN^C-type ligands was even more straightforward; reaction of 6-chloromethyl-2,2'-bipyridine with 1-methylimidazole or 1-methylbenzimidazole in refluxing acetonitrile gave b^im and b^zim, respectively, in quantitative yields.

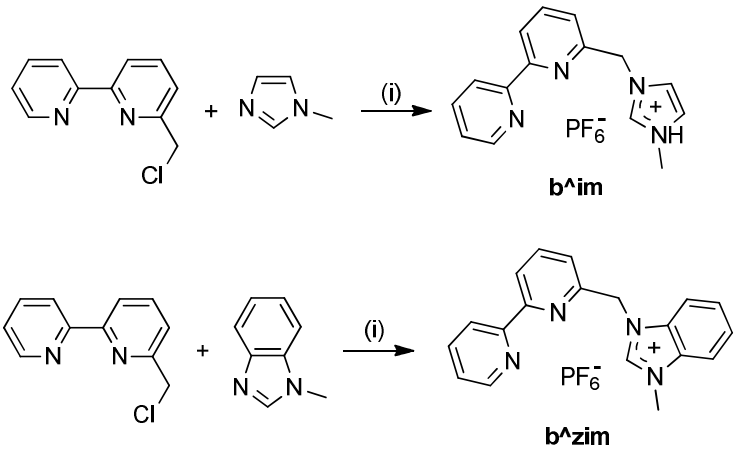

Scheme 4. Synthesis of NN^C ligands, **b^im** and **b^zim**

Heteroleptic Ru complexes ($[Ru(tpy)L]^{2+}$) were synthesized by a reaction between $[Ru(tpy)Cl_3]$ and a slight excess amount of ligand L in a refluxing ethylene glycol solution for 4 hrs. For homoleptic Ru complexes (RuL_2), $RuCl_3$ and ligand L were heated as the same procedures of Ru(tpy)L. All complexes were obtained in moderate yields (52-71%). Meanwhile, other synthetic approaches, such as Ag(I) transmetalation also provided the target products, but yields were poor (ca. 15%).

(2) Absorption Spectroscopy and Electrochemistry

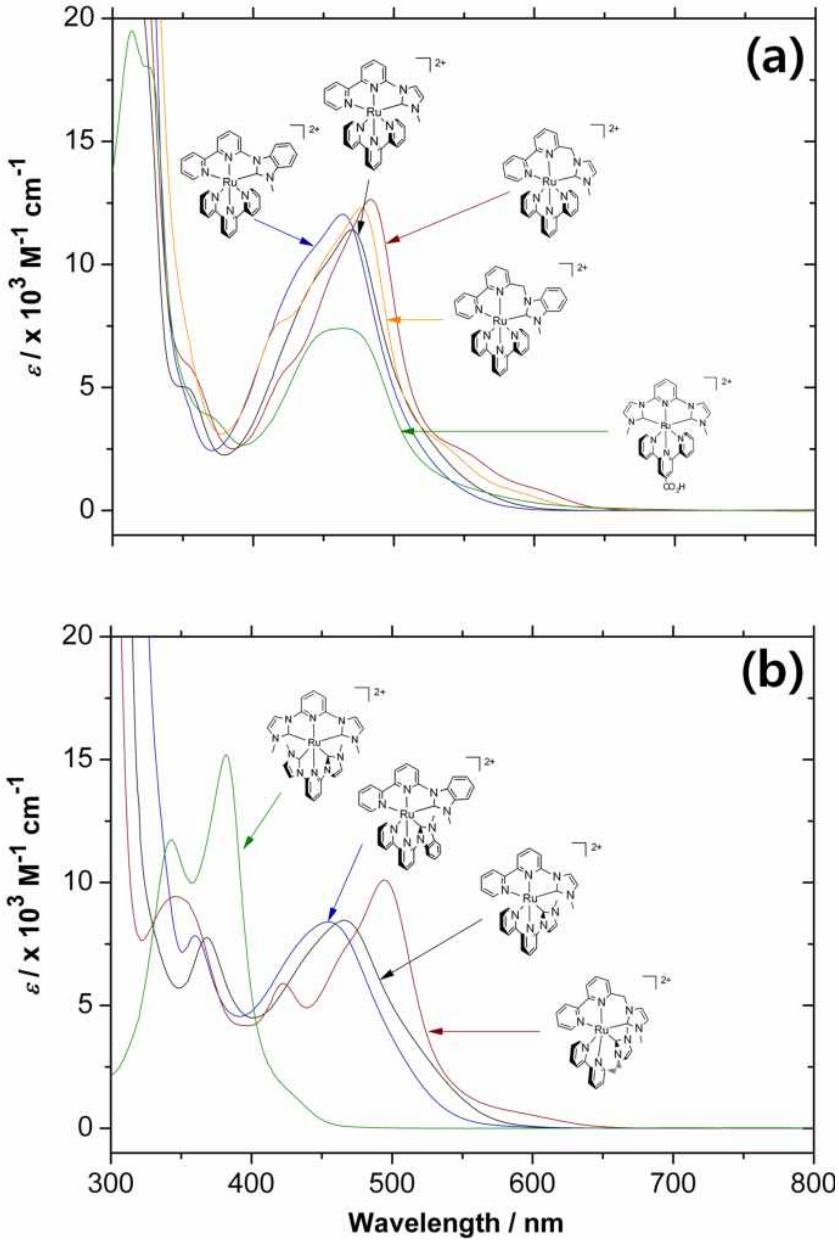

Figure 1. Electronic absorption spectra heteroleptic (a) and homoleptic (b) complexes along with benchmark molecules, $[Ru(bip)_2]^{2+}$ (b, green) and **CTN** (a, green)**.** Experimental conditions: solvent = acetonitrile, temperature = 25 ± 1°C.

Figure 1. displays electronic absorption spectra of seven complexes as well as their archetypal benchmark molecules, $[Ru(bip)_2]^{2+}$ and CTN for homoleptic and heteroleptic series, respectively. The corresponding λ_{max} and ε values are listed in Table 1. All complexes exhibit conventional absorption signatures characteristic of intense bands in the ultraviolet region (250-330 nm) for π-π* ligand centered (LC) transitions and moderately intense bands in the visible region (400-600 nm) for metal-to-ligand charge transfer (MLCT) bands. Further examination using the time-dependent density functional theory (TD-DFT) confirms these attributions, except for the fact that a mixed-metal-ligand-to-ligand CT is more suitable for describing the latter case. Figure 4 displays important frontier orbitals of seven complexes responsible for the lower energy electronic transitions. The relative energy levels and the spatial electron population of these orbitals are summarized in Figure 5 and Table 2, respectively. The three highest occupied orbitals of these complexes have their majority of electron populations (56-84%) at Ru metal. However, it is important to note that most of the electron population of HOMO is delocalized over Ru and azolyl ring plane highlighting the significant contribution of NHC group to the shape and energy of the HOMO. In case of complexes bearing 3-([2,2'-bipyridin]-6-yl)-1-methyl-1*H*-benzimidazol-3-ium (bzim) or 3-(2,2'-bipyridine-6-ylmethyl)-1-methyl-1*H*-benzimidazol-3-ium (b^zim) ligands, the electronic population of HOMO is more delocalized over the entire benzimidazolyl ring, thus decreasing the ligand field.

Table 1. Spectroscopic and voltammetric data.

Complex	λ_{max}	ε	$E_{1/2}^{2+/3+,\,a}$	$E_{1/2}^{1+/2+}$, $E_{1/2}^{0/1+,\,a}$
	nm	$\times 10^4$ $M^{-1}cm^{-1}$	V	V
1, Ru(tpy)(bim)	470	1.14	1.46	-1.07, -1.34
2, Ru(tpy)(bzim)	464	1.20	1.53	-1.04, -1.35
3, Ru(tpy)(b^im)	484	1.26	1.34	-1.06, -1.33
4, Ru(tpy)(b^zim)	477	1.23	1.45	-1.02, -1.30
5, $Ru(bim)_2$	466	0.85	1.43	-1.12, -1.36
6, $Ru(bzim)_2$	455	0.84	1.52	-1.08, -1.35
7, $Ru(b\hat{}im)_2$	495	1.01	1.15	-1.08, -1.45
$[Ru(bip)_2]^{2+,\,b}$	382	1.52	1.38	
$[Ru(tpy)_2]^{2+,\,b}$	474	1.72	1.55	-0.99

[a]Experimental conditions: [compound] = 5 mM; [$TBAPF_6$] = 0.1 M; solvent = acetonitrile; temperature = 25 ± 1 °C; scan rate = 100 mV/s; reference electrode = Ag/Ag^+; working electrode = glassy carbon. All potentials are referenced to a ferrocene/ferrocenium redox couple as an internal standard and converted to NHE by the relation ferrocene/ferrocenium vs. NHE = +0.64 V. [b]From ref. 7(a).

The λ_{max} values in the lower energy region reside between 464-484 nm for the heteroleptic series and 455-494 nm for the homoleptic series. The λ_{max} values for the homoleptic series span wider than those for the homoleptic one, whose background will be discussed in the later part of this paper. Interestingly, the absorption signatures

of these series complexes display clear trends as follow: (1) Complexes possessing NN^C-type ligand have lower energy λ_{max} values than those possessing NNC-type ligand. (2) Complexes possessing imidazole group in their respective NNC- or NN^C-type ligands have lower energy λ_{max} values than those possessing benzimidazolyl group. (3) Heteroleptic complexes have larger ε values compared to homoleptic counterparts. (4) Complexes possessing NN^C-type ligand have larger ε values relative to those possessing NNC-type ligand within the respective heteroleptic and homoleptic series. Trend (1) is contrary to our anticipation because if a conjugation is disrupted in NN^C-type ligand, the λ_{max} values would shift to the blue. This behaviour can be found in the literature by comparing two separate examples reported in ref. 7(a) and 8(a), respectively. In ref 7(b), λ_{max} of $[Ru(tpy\text{-}CO_2H)(CNC)]^{2+}$ (CTN) is 463 nm while that of $[Ru(tpy)(C^N^C)]^{2+}$ in ref 8(a) is ~500 nm. Although a direct comparison might not be appropriate because of a presence of carboxylic acid group in the tpy ligand in CTN, these two systems roughly indicate that whether the extent of electronic delocalization includes NHC moiety is not a major factor in determining the λ_{max} of Ru(NHC) complexes. Trend (2) combined with the results described above regarding trend (1) indicate that λ_{max} values are more affected by the σ-donating power induced by NHC moiety. This analysis drives us to examine the relationship between λ_{max} and σ-donating power more closely. Since the magnitude of σ-donating power is best indicated by electrochemical redox potentials, we considered the dependence of these values on λ_{max}.

Electrochemical oxidation potentials of the seven complexes in acetonitrile at 23 °C were recorded and their values are listed in Table 1. The one-electron reversible reductions of heteroleptic series occur within 0.05 V range (-1.02~-1.07 V vs. NHE) while those of homoleptic ones do within 0.04 V range (-1.08~-1.12 V vs. NHE). These confinements of reduction potentials originate the fact that LUMOs of these series are located either tpy or bpy ligand, both of which have very similar energy levels. We will show the shapes and energies of frontier orbitals of new complexes in the later part of this paper. On the contrary, the one-electron reversible oxidation potentials of complexes significantly differ each other according to the nature of the ligand. The values of heteroleptic series are 1.34, 1.45, 1.46, and 1.53 V vs. NHE for complexes **3**, **4**, **1**, and **2**, respectively. Those of homoleptic series are 1.15, 1.43, and 1.52 V vs. NHE for complexes **6**, **7**, and **5**, respectively. The maximum difference of the values is ca. 0.4 V. The trend of oxidation potential values is similar to that of absorption maxima. NN^C-type ligand gave more s-donating effect than NNC-type one and the imidazole group provide more s-donating effect than the benzimidazolyl group. As a result, HOMO-LUMO gaps of the series measured by electrochemical method are appeared to be dependent only on the oxidation potential values phenominologically.

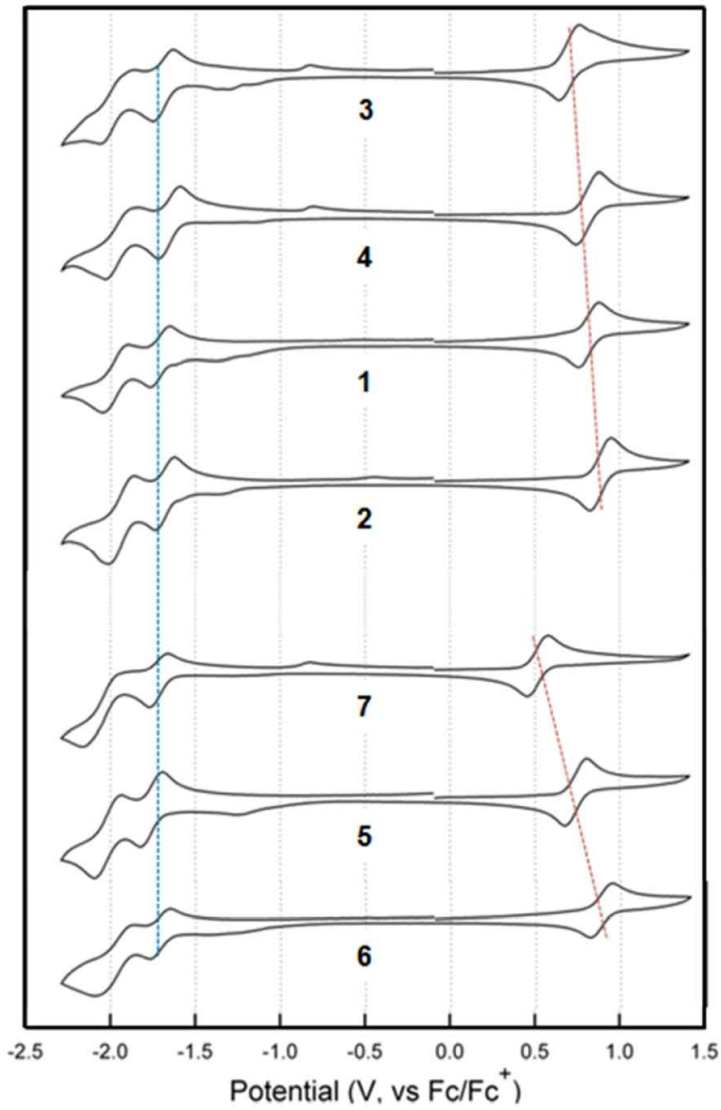

Figure 2. Cyclic voltammogram of seven complexes. Gradual shift of oxidation potential is guided by red dot line. Invariant reduction potential is guided by blue dot line. Experimental conditions: [compound] = 5 mM; [$TBAPF_6$] = 0.1 M; solvent = acetonitrile; temperature = 23 °C; scan rate = 100 mV/s; reference electrode = Ag/Ag+; working electrode = glassy carbon. All potentials are referenced to a ferrocene/ferrocenium redox couple as an internal standard and converted to NHE by the relation ferrocene/ferrocenium vs NHE = +0.64 V.

Figure 3 displays the relationship between the oxidation potential values and λ_{max}. As mentioned earlier, only $E_{1/2}{}^{2+/3+}$ values are strongly dependent on λ_{max} for both homoleptic and heteroleptic series. The degrees of correlation between $E_{1/2}{}^{2+/3+}$ and λ_{max} values for both homoleptic and heteroleptic series are very similar to each other as manifested by the virtually same slopes of each trend line.

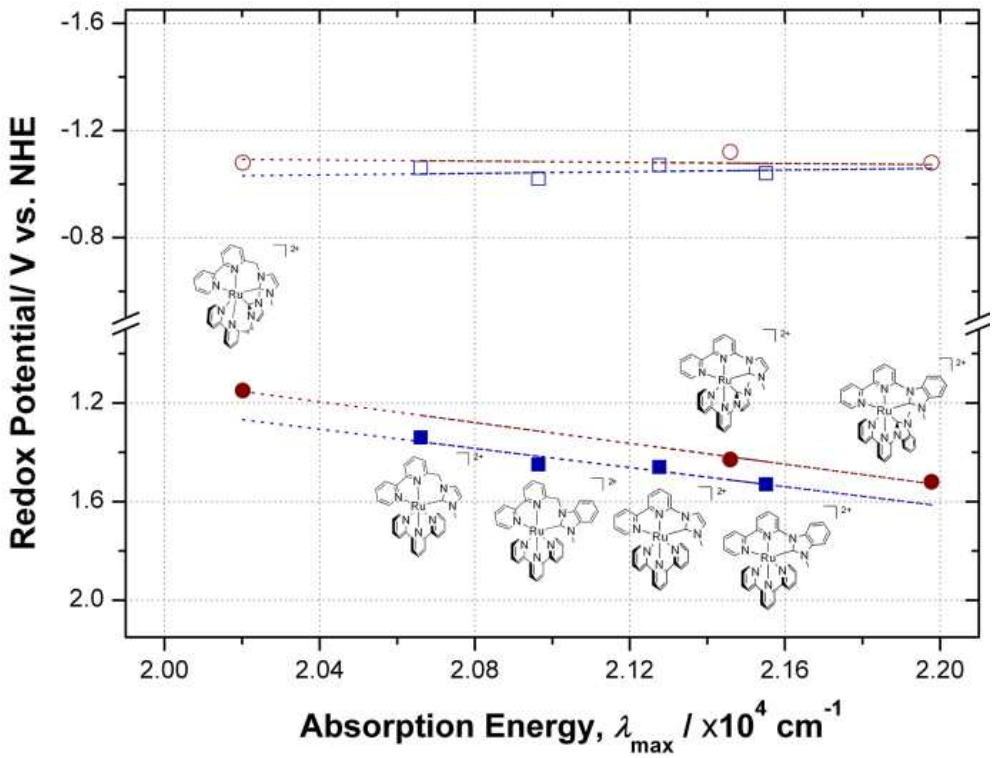

Figure 3. Dependence of the electrochemically determined $E_{1/2}{}^{2+/3+}$ (filled) and $E_{1/2}{}^{1+/2+}$ (open) values on λ_{max}, for heteroleptic (blue rectangles) and homoleptic (red circles) series. All these redox potentials are relative to the NHE. Experimental condition for electrochemical measurement: See footnote of Table 1.

In general, λ_{max} values scale with HOMO-LUMO gap; a gradual increase of λ_{max} coincides with a concomitant destabilization of HOMO and a stabilization of LUMO. Therefore, a strong dependence of $E_{1/2}^{2+/3+}$ values on λ_{max} is perhaps natural. The prominent dependence of λ_{max} only on $E_{1/2}^{2+/3+}$ values is phenomenological behaviour embossed by the silent dependence of λ_{max} values on $E_{1/2}^{2+/3+}$ ones. The background of levelling effect of $E_{1/2}^{1+/2+}$ values can be rationalized as follow: (1) In the heteroleptic series, most of the electronic population in LUMO is localized at tpy ligand regardless of a second ligand. The LUMO energy is primarily determined by the tpy energy level, which is not affected by Ru(NNC) or Ru(NN^C) moiety. 2) In the homoleptic series, most of the electronic population in LUMO is localized at bpy moiety of one of two NNC-type ligands (**5**) or equally at two bpy moieties of each ligand (**6** and **7**). As a result, the LUMO energies of each series are levelled. The absolute level of trend line of the $E_{1/2}^{1+/2+}/\lambda_{max}$ dependences for a homoleptic series is slightly higher than that for a heteroleptic one. This pattern mirrors the LUMO energies of bpy and tpy of their own, which are determined by DFT calculation.[9] While the slopes of two trend lines of both homoleptic and heteroleptic series are virtually the same, the absolute levels of those two differ by 0.1 V; it is quite natural that the destabilization of HOMO with two NHC ligands is more pronounced than that with only one unit.

The significant destabilization of HOMO level in homoleptic $[Ru(b\text{^}im)_2]^{2+}$ is worth noting. Considering the fact that the oxidation potential of $[Ru(bip)_2]^{2+}$ in which four NHC moieties are coordinated to the Ru center is only 1.38 V, an observed

value of 1.15 V $[Ru(b\hat{}im)]^{2+}$ is remarkable. Due to this substantial negative shift of oxidation potential, λ_{max} values of $[Ru(b\hat{}im)_2]^{2+}$ exhibit substantial bathochromic shift up to 495 nm, thus causing widely spread λ_{max} values of homoleptic series.

(3) Computational Study

The geometry optimizations and electronic structure calculations of seven new complexes were performed via using density functional theory (DFT). The nature of each MO is characterized by percent contribution of each atom summed into several classes; Ru, tpy, bpy, and imidazolyl or benzimidazolyl part for heteroleptic series, and Ru, bpy, and imidazolyl or benzimidazolyl part for homoleptic series (Table 2).

The 3-dimensional representations of the isosurfaces of each MO clearly confirm the character of the MO (Figure 4). For all seven complexes, the three highest occupied orbitals of these complexes have their majority of electron populations (56-84%) at Ru metal while three lowest unoccupied MOs have those in tpy or bpy ligands indicating that the lowest energy absorption bands are metal- to-ligand charge transfer in character. It is important to note that substantial amount of the electron population of HOMO is delocalized over azolyl ring plane (18-30%) highlighting the significant contribution of NHC group to the shape and energy of the HOMO. The degree of s-donation can be modulated by the type of NHC ligands as well as their geometries. Complexes with NN^C-type ligand have geometries more close to the perfect octahedron in terms of N-Ru-C bite angle compared to those with NNC-type one.[8(a)]

Table 2. Energies and Percent Compositions of Frontier MOs of **Ru(tpy)L** and **RuL$_2$.**

MO		Electron Population (%)					MO		Electron Population (%)				
1, Ru(tpy)(bim)							**5, Ru(bim)$_2$**						
No.		E (eV)	Ru	im[a]	tpy	bpy[c]	No.		E (eV)	Ru	im[a]	bpy[c]	
3^d	(133)	-2.43	2.1	0.3	95.3	2.3	3^d	(134)	-1.78	5.2	18.0	76.8	
2^d	(132)	-2.53	5.4	1.0	4.9	88.6	2^d	(133)	-2.48	7.0	2.0	91.0	
1^d	(131)	-2.60	9.7	1.4	85.6	3.3	1^d	(132)	-2.51	5.8	1.6	92.6	
0^d	(130)	-6.06	64.8	18.4	10.0	6.8	0^d	(131)	-5.92	59.5	28.5	12.0	
-1^d	(129)	-6.19	69.8	6.6	15.8	7.9	-1^d	(130)	-6.17	68.8	11.8	19.4	
-2^d	(128)	-6.28	73.3	3.8	11.6	11.3	-2^d	(129)	-6.19	68.8	11.4	19.8	
-3^d	(127)	-7.18	1.0	9.8	69.3	19.9	-3^d	(128)	-7.05	2.2	51.2	46.6	
2, Ru(tpy)(bzim)							**6, Ru(bzim)$_2$**						
No.		E (eV)	Ru	zim[b]	tpy	bpy[c]	No.		E (eV)	Ru	zim[b]	bpy[c]	
3^d	(146)	-2.46	2.1	0.4	94.6	2.9	3^d	(160)	-1.84	5.4	24.6	70.0	
2^d	(145)	-2.54	5.5	1.4	5.8	87.3	2^d	(159)	-2.53	6.6	3.0	90.4	
1^d	(144)	-2.63	9.5	1.5	85.7	3.3	1^d	(158)	-2.56	6.0	2.2	91.8	
0^d	(143)	-6.14	63.2	19.4	9.9	7.5	0^d	(157)	-6.08	56.4	30.6	13.0	
-1^d	(142)	-6.26	69.5	7.0	15.5	8.0	-1^d	(156)	-6.29	66.2	15.0	18.8	
-2^d	(141)	-6.32	69.8	8.4	11.2	10.6	-2^d	(155)	-6.30	64.8	16.8	18.4	
-3^d	(140)	-6.92	3.9	65.6	1.6	28.9	-3^d	(154)	-6.87	0.0	67.4	32.6	
3, Ru(tpy)(b^im)							**7, Ru(b^im)$_2$**						
No.		E (eV)	Ru	im[a]	tpy	bpy[c]	No.		E (eV)	Ru	im[a]	bpy[c]	
3^d	(137)	-1.66	4.8	1.4	64.2	29.6	3^d	(142)	-2.44	2.8	11.6	85.6	
2^d	(136)	-2.44	3.7	2.4	41.3	52.6	2^d	(141)	-2.51	5.6	4.8	89.6	
1^d	(135)	-2.55	7.7	1.9	78.7	11.7	1^d	(140)	-2.66	5.2	5.4	89.4	
0^d	(134)	-5.69	63.4	23.1	9.9	3.6	0^d	(139)	-5.88	62.0	29.0	9.0	
-1^d	(133)	-5.90	76.8	0.8	13.3	9.1	-1^d	(138)	-6.17	70.0	14.4	15.6	
-2^d	(132)	-6.17	77.6	3.0	14.6	4.8	-2^d	(137)	-6.25	83.4	4.4	12.2	
-3^d	(131)	-6.99	4.0	28.0	65.9	2.1	-3^d	(136)	-7.18	10.8	83.4	5.8	
4, Ru(tpy)(b^zim)							**Ru(tpy)$_2$**						
No.		E (eV)	Ru	zim[b]	tpy	bpy[c]	No.		E (eV)	Ru	tpy	tpy'	
3^d	(150)	-2.47	4.6	1.8	63.7	29.9	3^d	(132)	-2.49	0.0	50.0	50.0	
2^d	(149)	-2.54	3.5	2.5	40.5	53.3	2^d	(131)	-2.64	8.8	4.0	87.2	
1^d	(148)	-2.69	7.6	2.0	80.1	10.3	1^d	(130)	-2.64	8.8	87.2	4.0	
0^d	(147)	-6.00	61.4	25.2	9.9	3.5	0^d	(129)	-6.23	75.2	12.4	12.4	
-1^d	(146)	-6.24	76.7	1.0	13.2	9.1	-1^d	(128)	-6.30	73.7	11.8	14.5	
-2^d	(145)	-6.33	77.5	3.2	14.5	4.8	-2^d	(127)	-6.30	73.7	14.5	11.8	
-3^d	(144)	-6.82	0.3	97.3	0.6	1.8	-3^d	(126)	-7.22	0.0	49.7	50.3	

[a]Methylimidazole part of ligand. [b]Methylbenzimidazole part of ligand. [c]Bipyridyl part of NNC

or NN^C ligand. ^{d}0 and 1 indicate HOMO and LUMO, respectively. –1, –2, -3 correspond to HOMO-1, HOMO-2, HOMO-3, respectively while 2 and 3 represent LUMO+1 and LUMO+2, respectively.

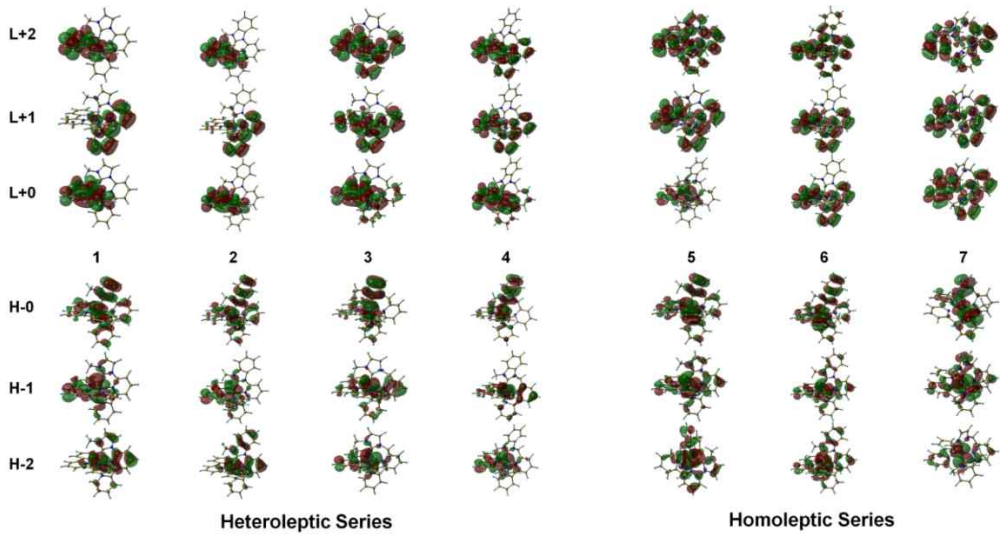

Figure 4. Frontier molecular orbitals calculated at the B3LYP/LANL2DZ level.

For heteroleptic series, the ligand field applied by the NHC moiety is thus more prominent in complex 3 and 4 than in complex 1 and 2. Accordingly, the degree of destabilization of HOMO energy level is thus more prevailing in complex 3 and 4. The same is true for the homoleptic series; complex 7 has higher HOMO energy level compared to complex 5 and 6. When we focus on the nature of NHC ligand, imidazolyl group provide stronger ligand field than benzimidazolyl group since the electronic populations are far more delocalized over the aromatic ring in

benzimidazolyl ring, thus weaken the s-donating effect. As a result, the energy levels of HOMOs with benzimidazolyl group are less destabilized compared to those with simple imidazolyl group. These analyses clearly show how the structure and geometry NHC moiety affect the shapes and energies of HOMOs.

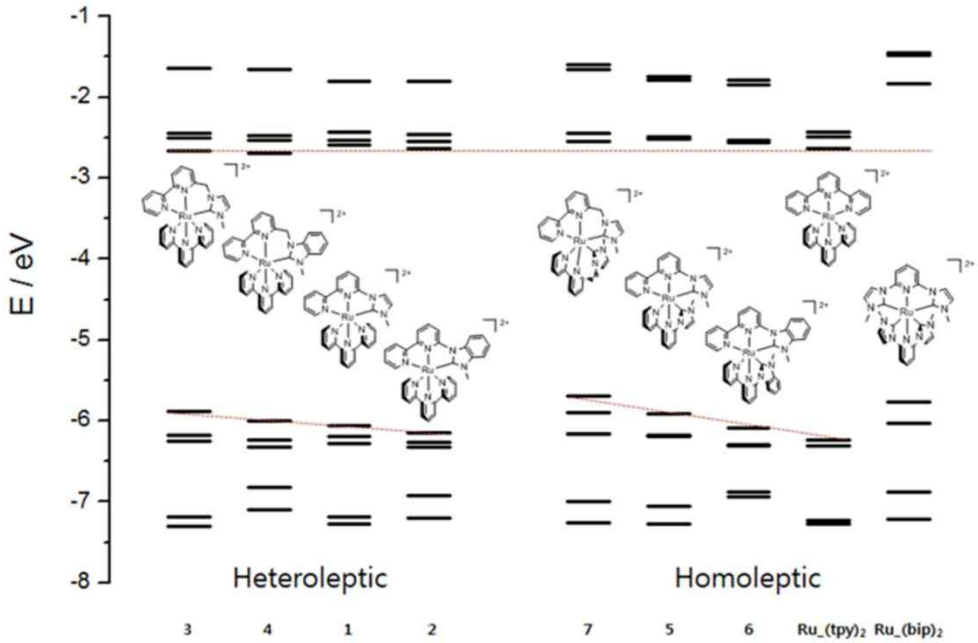

Figure 5. Frontier molecular orbital (five highest occupied and four lowest unoccupied) energy diagram of complex 1-7, $[Ru(tpy)_2]^{2+}$, and $[Ru(bip)_2]^{2+}$ calculated at the B3LYP/LANL2DZ level. Gradual stabilization of HOMO energy levels and levelling of LUMO energy levels are guided by red dotted lines.

As shown in Figure 4, the electronic populations in the LUMOs of heteroleptic series are apparently localized in the whole tpy ligand, while those of homoleptic

series are separately localized n the two bpy ligands. As mentioned earlier, the energy levels of LUMOs of tpy or bpy are similar each other. No matter what the LUMO is localized in one tpy ligand or two bpy ones, the resulting reduction potentials of such complexes are thus appear to be similar. In the case of HOMOs, however, electronic populations are shared by Ru metal and NHC moiety of NNC or NN^C-type ligands.

In conclusion, we have newly synthesized seven Ru complexes that possess a heteroleptic $[Ru(tpy)(NHC)]^{2+}$ or a homoleptic $[Ru(NHC)_2]^{2+}$ topology and feature NNC- or NN^C-type NHC structural motif. These complexes have varying degrees of oxidation potentials induced by different ligand field of NHC moiety, yet have levelled reduction potential due to the similar LUMO energy localized in bpy or tpy moiety. We observed that the lmax values of these series complexes are correlated with only the oxidation potentials. Given the structure-property relationship obtained in this study, we could modulate lmax values of Ru(NHC) complexes to some extent.

3. Experimental Section

All reactions were carried out under a nitrogen atmosphere unless otherwise noted. Standard Schlenk techniques were employed to manipulate air-sensitive solutions, while workup procedures were done in air. Tetrahydrofuran (THF) were purchased from Fischer Scientific (HPLC grade) and dried over Na/benzophenone and were subsequently distilled under nitrogen prior to use. Toluene was purchased from Samchun Chemicals and dried over Na/benzophenone and were subsequently distilled under nitrogen prior to use. *N,N*-dimethylformamide (DMF) and acetonitrile were distilled over CaH_2 prior to use. Ethylene glycol (Aldrich) was used without further purification. Tetrakis(triphenylphosphine)palladium(0) was purchased from Pressure Chemical Co. Copper(II) oxide was purchased from Daejung Chemical Co. 2-Bromopyridine, 2,6-dibromopyridine (98%), tributyltin chloride (96%), *n*-butyl lithium (2.0 M solution in *n*-hexane), imidazole, 1-methylimidazole, benzimidazole, 1-methylbenzimidazole, iodomethane, 2,2':6',2''-terpyridine, ammonium hexafluorophosphate (NH_4PF_6) were purchased from Aldrich Chemical Co. 6-Bromo-2,2'-bipyridine,[1] 6-chloromethyl-2,2'-bipyridine,[2] (2,2':6',2''-tepyridine)(trichloro)Ru(III) ($Ru(tpy)Cl_3$)[3] were prepared according to literature procedures. Column chromatography was performed on silica gel 60 (230-400 Mesh, Merck).

^1H and ^{13}C NMR spectra were recorded with Bruker (75 MHz for ^{13}C NMR), Aglient (400 MHz and 100 MHz for ^1H and ^{13}C NMR, respectively) and Aglient (500 MHz and 125 MHz for ^1H and ^{13}C NMR, respectively) spectrometers. ^1H NMR

spectra were taken in $CDCl_3$ and DMSO-d_6 and were referenced to residual $CDCl_3$ (7.26 ppm) and DMSO-d_6 (2.50 ppm), respectively. Chemical shifts of the ^{13}C NMR spectra were measured relative to $CDCl_3$ (77.16 ppm) or DMSO-d_6 (39.52). Elemental analyses were done at the National Center for Inter-University Research Facilities located in the Seoul National University. High-resolution mass spectrometry (HRMS) data were obtained at the Korea Basic Science Institute (Daegu). Electronic absorption spectra were recorded on a Beckman Du-650 spectrophotometer. Cyclic voltammograms were obtained with a CH Instrument voltammetric analyzer. Measurements were performed after the acetonitrile (spectroscopic grade) solution was purged with dry nitrogen gas for 30 min. The supporting electrolyte was 0.1 M tetrabutylammonium hexafluorophosphate ($TBAPF_6$). Glassy carbon and Ag/Ag^+ (0.01M $AgNO_3$) were used as working and reference electrodes, respectively. The scan rate was maintained at 100 mV/s.

Synthesis of ligands

6-(1*H*-imidazol-1-yl)-2,2'-bipyridine (**bi**): To a flask containing 6-bromo-2,2'-bipyridine (0.47 g, 2 mmol), imidazole (0.16 g, 2.4 mmol), potassium carbonate (0.33 g, 2.4 mmol) in 6 mL DMF solution, copper(II) oxide (16 mg, 10 mol%) was added. The solution was heated at 150℃ for 36 h. After the solution was cooled to room temperature, the solvent was removed under reduced pressure and extracted with CH_2Cl_2 (3 × 30 mL). The organic layer was washed with brine and dried with

Na_2SO_4. Purification with silica gel column chromatography (DCM:MeOH = 20:1) gave white solid in 95% yield (0.43 g). ^{1}H NMR (400 MHz, $CDCl_3$) δ 8.67 (ddd, J = 4.8, 1.8, 0.9 Hz, 1 H), 8.45 (s, 1 H), 8.40 (dt, J = 8.0, 1.0 Hz, 1 H), 8.34 (dd, J = 7.8, 0.7 Hz, 1 H), 7.89 (t, J = 7.9 Hz, 1 H), 7.84 – 7.79 (m, 1 H), 7.72 (t, J = 1.3 Hz, 1 H), 7.34 – 7.30 (m, 2 H), 7.23 (s, 1 H); ^{13}C NMR (100 MHz, $CDCl_3$) δ 155.5, 154.7, 149.1, 148.3, 139.9, 136.9, 134.9, 130.6, 124.2, 121.1, 118.9, 116.1, 111.9; HRMS(FAB+), *m/z* $[M+H]^+$ found (calc): 223.0986 (223.0984)

3-([2,2'-Bipyridin]-6-yl)-1-methyl-1*H*-imidazol-3-ium hexafluorophosphate (bim): To a flask containing **bi** (0.22 g, 1 mmol) in dry acetonitrile, methyl iodide (0.13 mL, 2 mmol) was added and heated reflux for 4 h. After the solution was cooled to room temperature, the solvent was removed by rotary evaporator. Crude mixture was dissolved with minimum amount of methanol and dropped to diethyl ether. White precipitate was filtered and redissolved in 10 mL of water. Excess NH_4PF_6 was added and the resulting solution was stirred for 10 min. White precipitate was filtered, washed with water and dried by vacuo (yield: quantitative). ^{1}H NMR (400 MHz, DMSO) δ 10.21 (s, 1 H), 8.75 (d, J = 8.0 Hz, 1 H), 8.65 (t, J = 2.0 Hz, 1 H), 8.63 (d, J = 8.0 Hz, 1 H), 8.53 (d, J = 8.0 Hz, 1 H), 8.33 (t, J = 8.0 Hz, 1 H), 8.04 (dt, J = 7.0, 2.0 Hz, 2 H), 7.98 (t, J = 1.8 Hz, 1 H), 7.55 (ddd, J = 7.5, 4.8, 1.1 Hz, 1 H), 4.01 (s, 3 H); ^{13}C NMR (100 MHz, DMSO) δ 155.0, 153.4, 149.7, 146.1, 141.9, 137.7, 135.8, 125.3, 124.9, 121.4, 121.2, 119.2, 113.9, 36.5; HRMS(FAB+), *m/z* $[M]^+$ found (calc): 237.1141 (237.1140)

1-([2,2'-Bipyridin]-6-yl)-1*H*-benzimidazole (**bzi**): Prepared as described for **bi,** from benzimidazole (0.28 g, 2.4 mmol), 6-bromo-2,2'-bipyridine (0.47 g, 2 mmol), potassium carbonate (0.33 g, 2.4 mmol) and copper(II) oxide(16 mg, 10 mol%) in 6 mL of DMF. The solution was refluxed for 48 h. After purification on silica gel (DCM:MeOH = 22:1), light yellow solid was obtained (yield: 0.61 g, 94%). ^{1}H NMR (400 MHz, $CDCl_3$) δ 8.64 (dd, J = 4.7, 0.7 Hz, 1 H), 8.59 (s, 1 H), 8.35 (t, J = 8.2 Hz, 2 H), 8.07 (dd, J = 6.6, 2.4 Hz, 1 H), 7.90 – 7.83 (m, 2 H), 7.75 (td, J = 7.8, 1.8 Hz, 1 H), 7.41 (d, J = 7.8 Hz, 1 H), 7.39 – 7.32 (m, 2 H), 7.26 (ddd, J = 7.4, 4.8, 1.0 Hz, 1 H); ^{13}C NMR (100 MHz, $CDCl_3$) δ 155.6, 154.6, 149.0, 148.9, 144.5, 141.2, 139.6, 136.8, 131.9, 124.1, 124.0, 123.1, 120.9, 120.5, 118.6, 113.7, 112.6; HRMS(FAB+), *m/z* $[M+H]^+$ found (calc): 273.1137 (273.1140)

3-([2,2'-Bipyridin]-6-yl)-1-methyl-1*H*-benzimidazol-3-ium hexafluorophosphate (**bzim**): Prepared as described for **1**, from **bzi** (0.27 g, 1 mmol) and methyl iodide (0.13 mL, 2 mmol). Yield: Quantitative. ^{1}H NMR (400 MHz, DMSO) δ 10.57 (s, 1 H), 8.80 (ddd, J = 4.7, 1.7, 0.9 Hz, 1 H), 8.64 (dd, J = 7.8, 0.6 Hz, 1 H), 8.55 (dd, J = 7.5, 1.5 Hz, 1 H), 8.48 (dd, J = 4.9, 4.0 Hz, 1 H), 8.43 (t, J = 8.0 Hz, 1 H), 8.18 (dd, J = 7.4, 1.6 Hz, 1 H), 8.12 – 8.04 (m, 2 H), 7.88 – 7.80 (m, 2 H), 7.58 (ddd, J = 7.5, 4.8, 1.1 Hz, 1 H), 4.24 (s, 3 H); ^{13}C NMR (100 MHz, DMSO) δ 155.5, 153.5, 149.8, 146.9, 143.1, 141.9, 137.8, 132.4, 129.3, 128.0, 127.2, 125.2, 121.3, 121.1, 116.9, 115.5, 114.1, 33.8; HRMS(FAB+), *m/z* $[M]^+$ found (calc): 287.1295 (287.1297)

3-(2,2'-Bipyridine-6-ylmethyl)-1-methyl-1*H*-imidazol-3-ium hexafluorophosphate (**b^im**): A solution of 6-(chloromethyl)-2,2-bipyridine (0.45 g, 2.2 mmol) and 1-methylimidazole (0.16 g, 2.0 mmol) in 10 mL of dry acetonitrile was refluxed for 48 h. After the solution was cooled to room temperature, the solvent was removed by rotary evaporator. Crude mixture was dissolved by 3 mL of dichloromethane and the solution was dropped to diethyl ether. White precipitate was filtered and redissolved in 10 mL of water. Excess NH_4PF_6 was added and the resulting solution was stirred for 10 min. White precipitate was filtered, washed with water and dried by vacuo (yield: 0.79 g, quantitative). ^{1}H NMR (400 MHz, $CDCl_3$) δ 10.58 (s, 1 H), 8.62 (d, J = 4.6 Hz, 1 H), 8.34 (d, J = 7.9 Hz, 1 H), 8.27 (d, J = 7.9 Hz, 1 H), 7.80 (t, J = 7.7 Hz, 2 H), 7.73 (s, 2 H), 7.67 (d, J = 7.5 Hz, 1 H), 7.32 – 7.27 (m, 1 H), 5.81 (s, 2 H), 4.08 (s, 3 H); ^{13}C NMR (100 MHz, DMSO) δ 155.6, 154.9, 153.7, 149.8, 139.2, 137.8, 137.8, 125.0, 124.1, 123.7, 123.0, 121.0, 120.5, 53.4, 36.3; HRMS(FAB+), *m/z* $[M]^+$ found (calc): 251.1295 (251.1297)

3-(2,2'-Bipyridine-6-ylmethyl)-1-methyl-1*H*-benzimidazol-3-ium hexafluorophosphate (**b^zim**): The same procedure as the synthesis of **b^im**. 6-(Chloromethyl)-2,2-bipyridine (0.45 g, 2.2 mmol) and 1-methylbenzimidazole (0.16 g, 2.0 mmol) gave **b^im** in quantitative yield. (0.892 g) ^{1}H NMR (400 MHz, DMSO) δ 9.95 (s, 1 H), 8.66 (ddd, J = 4.8, 1.8, 0.9 Hz, 1 H), 8.35 (dd, J = 7.9, 0.9 Hz, 1 H), 8.10 – 8.02 (m, 4 H), 7.90 – 7.85 (m, 1 H), 7.74 – 7.66 (m, 3 H), 7.44 (ddd, J = 7.5, 4.8, 1.2 Hz, 1 H), 6.01 (s, 2 H), 4.17 (d, J = 0.4 Hz, 3 H); ^{13}C NMR (100 MHz, DMSO)

δ 155.2, 154.4, 152.8, 149.4, 143.6, 138.8, 137.4, 131.9, 131.3, 126.7, 126.5, 124.5, 122.9, 120.4, 120.2, 113.9, 113.7, 50.8, 33.4; HRMS(FAB+), *m/z* $[M]^+$ found (calc): 301.1455 (301.1453)

General Procedure for Ru Complexes

Ru(tpy)L: $Ru(tpy)Cl_3$ (132 mg, 0.3 mmol) and L (0.3 mmol) in 5 mL of ethylene glycol was heated at 180℃ for 4 h. After the solution was cooled to room temperature, the solution was added dropwisely to a saturated aqueous solution of NH_4PF_6, causing to precipitation of the compound. After the precipitate was filtered, it was purified by silica gel column chromatography (CH_3CN:0.5M $NaNO_3$ = 9:1) gave the desired product.

Ru(tpy)(bim) (**1**): Orange solid; Yield: 59%. ^{1}H NMR (400 MHz, DMSO) δ 9.01 (s, 1 H), 8.99 (s, 1 H), 8.88 – 8.82 (m, 2 H), 8.78 (s, 1 H), 8.77 (s, 1 H), 8.59 (d, J = 2.3 Hz, 1 H), 8.55 (dd, J = 8.3, 1.1 Hz, 1 H), 8.53 – 8.49 (m, 1 H), 8.47 (t, J = 8.1 Hz, 1 H), 8.07 (td, J = 7.9, 1.5 Hz, 1 H), 8.02 (td, J = 7.9, 1.5 Hz, 2 H), 7.52 (dd, J = 5.1, 1.0 Hz, 1 H), 7.36 (dd, J = 5.6, 0.8 Hz, 2 H), 7.32 (ddd, J = 7.5, 5.5, 1.2 Hz, 1 H), 7.28 – 7.22 (m, 3 H), 2.76 (s, 3 H); ^{13}C NMR (100 MHz, DMSO) δ 184.5, 157.0, 155.2, 154.5, 154.4, 152.3, 151.9, 150.3, 138.7, 138.2, 137.6, 134.9, 134.9, 127.6, 124.5, 124.5, 124.4, 123.8, 119.6, 118.5, 111.8, 34.9; HRMS(FAB+), *m/z* $[M+PF_6]^+$ found (calc): 716.0695 (716.0708); Anal. calcd for $C_{29}H_{23}F_{12}N_7P_2Ru$: C, 40.48; H,

2.69; N, 11.39. Found: C, 40.36; H, 2.82; N, 11.27.

Ru(tpy)(bzim) (**2**): Light orange solid; Yield: 52%. ^{1}H NMR (400 MHz, CD_3CN) δ 8.72 (d, J = 8.2 Hz, 2 H), 8.59 (dd, J = 17.0, 8.8 Hz, 3 H), 8.48 (t, J = 8.2 Hz, 3 H), 8.41 (t, J = 8.2 Hz, 1 H), 8.25 (d, J = 8.2 Hz, 1 H), 8.01 (td, J = 8.0, 1.5 Hz, 1 H), 7.92 (td, J = 8.0, 1.4 Hz, 2 H), 7.50 (t, J = 7.3 Hz, 1 H), 7.42 (dd, J = 9.1, 6.5 Hz, 2 H), 7.28 (dt, J = 7.4, 4.2 Hz, 4 H), 7.16 – 7.09 (m, 2 H), 2.98 (s, 3 H); ^{13}C NMR (75 MHz, CD_3CN) δ 199.7, 158.2, 156.5, 156.3, 155.9, 154.3, 153.5, 151.2, 139.9, 139.2, 138.8, 136.7, 136.4, 133.0, 128.5, 128.3, 125.7, 125.4, 125.3, 124.8, 120.0, 118.3, 113.6, 112.3, 111.7, 33.4; HRMS(FAB+), *m/z* $[M+PF_6]^+$ found (calc): 766.0859 (766.0866); Anal. calcd for $C_{33}H_{25}F_{12}N_7P_2Ru$: C, 43.53; H, 2.77; N, 10.77; Found: C, 43.48; H, 2.89; N, 10.69.

Ru(tpy)(b^im) (**3**): Red solid; Yield: 56%. ^{1}H NMR (400 MHz, DMSO) δ 8.93 (t, J = 8.3 Hz, 3 H), , 8.72 (t, J = 8.3 Hz, 3 H), 8.43 (td, J = 8.0, 4.4 Hz, 2 H), 8.16 (d, J = 7.4 Hz, 1 H), 8.02 (td, J = 7.9, 1.4 Hz, 2 H), 7.97 (td, J = 8.0, 1.4 Hz, 1 H), 7.67 (d, J = 4.9 Hz, 2 H), 7.50 (d, J = 1.8 Hz, 1 H), 7.35 – 7.28 (m, 3 H), 7.02 (d, J = 1.9 Hz, 1 H), 7.01 (d, J = 5.7 Hz, 1 H), 5.94 (s, 2 H), 2.54 (s, 3 H); ^{13}C NMR (100 MHz, DMSO) δ 176.8, 157.4, 157.1, 156.5, 155.8, 154.6, 153.0, 147.7, 138.0, 137.9, 137.7, 135.2, 128.0, 127.2, 126.3, 124.3, 124.3, 124.0, 123.8, 123.5, 122.9, 53.5, 35.4; HRMS(FAB+), *m/z* $[M+PF_6]^+$ found (calc): 730.0862 (730.0865); Anal. calcd for

$C_{33}H_{25}F_{12}N_7P_2Ru$: C, 43.53; H, 2.77; N, 10.77; Found: C, 43.45; H, 2.91; N, 10.67.

Ru(tpy)(b^zim) (**4**): Dark orange solid; Yield: 63%. ^{1}H NMR (400 MHz, DMSO) δ 9.00 – 8.94 (m, 3 H), 8.75 (t, J = 8.3 Hz, 3 H), 8.50 (dd, J = 12.0, 4.3 Hz, 2 H), 8.42 (dd, J = 7.7, 1.1 Hz, 1 H), 8.04 (d, J = 1.5 Hz, 1 H), 8.04 – 7.99 (m, 3 H), 7.76 (dd, J = 5.6, 0.8 Hz, 2 H), 7.39 – 7.34 (m, 3 H), 7.33 – 7.28 (m, 2 H), 7.27 – 7.22 (m, 1 H), 7.04 – 7.00 (m, 1 H), 6.26 (s, 2 H), 2.78 (s, 3 H); ^{13}C NMR (75 MHz, DMSO) δ 192.2, 157.3, 156.9, 156.6, 155.8, 154.5, 153.3, 147.5, 138.3, 138.2, 138.1, 138.0, 135.9, 134.9, 134.2, 128.1, 127.3, 126.6, 124.4, 124.3, 123.8, 123.6, 123.0, 122.8, 109.9, 49.7, 31.6; HRMS(FAB+), *m/z* $[M+PF_6]^+$ found (calc): 780.1010 (780.1022); Anal. calcd for $C_{34}H_{27}F_{12}N_7P_2Ru$: C, 44.17; H, 2.94; N, 10.60; Found: C, 44.11; H, 3.03; N, 10.53

.

RuL$_2$: $RuCl_3 \cdot 3H_2O$ (78 mg, 0.3 mmol) and L (0.6 mmol) in 8 mL of ethylene glycol was heated at 180℃ for 4 h. After cooling to room temperature, crude solution was dropped to saturated aqueous solution of NH_4PF_6 caused precipitation of the compound. After filteration, the solid was purified by silica gel column chromatography (CH_3CN:0.5M $NaNO_3$ = 9:1) gave the desired product.

Ru(bim)$_2$ (**5**): Orange solid; Yield: 71%. ^{1}H NMR (400 MHz, DMSO) δ 8.81 (m, 4 H), 8.55 (d, J = 2.2 Hz, 2 H), 8.51 – 8.43 (m, 4 H), 8.08 (dd, J = 11.2, 4.5 Hz, 2 H),

7.48 (d, *J* = 5.0 Hz, 2 H), 7.34 (t, *J* = 8.0 Hz, 2 H), 7.29 (d, *J* = 2.2 Hz, 2 H), 2.66 (s, 6 H); ^{13}C NMR (100 MHz, DMSO) *δ* 184.5, 154.8, 154.3, 151.8, 150.5, 138.2, 137.2, 127.5, 124.3, 124.3, 119.3, 117.9, 111.2, 34.8; HRMS(FAB+), *m/z* $[M+H]^+$ found (calc): 719.0806 (719.0817); Anal. calcd for $C_{28}H_{24}F_{12}N_8P_2Ru$: C, 38.94; H, 2.80; N, 12.98; Found: C, 38.89; H, 2.83; N, 12.94.

Ru(bzim)$_2$, (**6**): Yellow solid; Yield: 68%. ^{1}H NMR (400 MHz, DMSO) *δ* 8.99 – 8.83 (m, 6 H), 8.58 (t, *J* = 9.4 Hz, 4 H), 8.12 (t, *J* = 7.3 Hz, 2 H), 7.51 (dd, *J* = 13.4, 6.7 Hz, 4 H), 7.48 – 7.40 (m, 4 H), 7.38 – 7.32 (m, 2 H), 2.87 (s, 6 H); ^{13}C NMR (75 MHz, DMSO) *δ* 196.7, 154.7, 154.4, 152.1, 150.4, 138.6, 138.1, 135.2, 131.1, 127.7, 124.6, 124.5, 124.1, 119.4, 112.7, 111.9, 111.1, 32.1; HRMS(FAB+), *m/z* $[M+PF_6]^+$ found (calc): 819.1125 (819.1132); Anal. calcd for $C_{36}H_{28}F_{12}N_8P_2Ru$: C, 44.87; H, 2.93; N, 11.63; Found: C, 44.84; H, 3.01; N, 11.59.

Ru(b^im)$_2$ (**7**): Brown solid; Yield: 66%. ^{1}H NMR (400 MHz, DMSO) *δ* 8.77 (d, *J* = 8.0 Hz, 2 H), 8.55 (d, *J* = 8.0 Hz, 2 H), 8.32 (t, *J* = 7.9 Hz, 2 H), 7.99 (d, *J* = 7.6 Hz, 2 H), 7.94 (t, *J* = 7.5 Hz, 2 H), 7.55 (d, *J* = 1.5 Hz, 2 H), 7.27 (t, *J* = 7.9 Hz, 2 H), 7.10 (d, *J* = 1.6 Hz, 2 H), 6.87 (d, *J* = 5.0 Hz, 2 H), 5.81 (d, *J* = 15.4 Hz, 2 H), 4.97 (d, *J* = 15.2 Hz, 2 H), 2.45 (s, 6 H); ^{13}C NMR (100 MHz, DMSO) *δ* 180.3, 158.1, 156.9, 154.3, 148.5, 138.0, 137.4, 127.2, 125.2, 123.7, 123.3, 123.2, 122.3, 54.0, 35.3; HRMS(FAB+), *m/z* $[M+PF_6]^+$ found (calc): 747.1126 (747.1130); Anal. calcd for

$C_{30}H_{28}F_{12}N_8P_2Ru$: C, 40.41; H, 3.17; N, 12.57; Found: C, 40.38; H, 3.23; N, 12.55.

4. Reference

(1) (a) V. S. Y. Lin, S. G. DiMagno and M. J. Therien, *Science* **1994**, *264***,** 1105-1111. (b) K. Susumu and M. J. Therien, *J. Am. Soc. Chem*. **2002**, *124*, 8550-8552. (c) X. Schultze, J. Serin, A. Adronov and J. M. J. Fréchet, *Chem. Commun.* **2001**, 1160- 1161. (d) N. D. McClenaghan, R. Passalacqua, F. Loiseau, S. Campagna, B. Verheyde, A. Hameurlaine and W. Dehaen, *J. Am. Soc. Chem*. **2003**, *125*, 5356-5365. (e) D. Kim and A. Osuka, *Acc. Chem. Rev*. **2004**, *37*, 735-745. (f) Y. Kobuke, *Eur. J. Inorg. Chem.* **2006**, 2333-2351. (f) A. Nantalaksakul, D. R. Reddy, C. J. Bardeen and S. Thayumanavan, *Photosynth. Res*. **2006**, *87*, 133-150. (g) W. Y. Wong, X. Z. Wang, Z. He, K. K. Chan, A. B. Djurišć, K. Y. Cheung, C. T. Yip, A. M. C. Ng, Y. X. Yan, C. S. K. Mak and W. K. Chan, *J. Am. Soc. Chem.* **2007**, *129*, 14372-14380. (h) C. Röger, Y. Miloslavina, D. Brunner, A. R. Holzwarth and F. Würthner, *J. Am. Soc. Chem*. **2008**, *130*, 5929-5939. (i) Y. J. Cheng, S. H. Yang and C. S. Hsu, *Chem. Rev*. **2009**, *109*, 5868-5923. (j) M. R. Wasielewski, *Acc. Chem. Rev*. **2009**, *42*, 1910-1921. (k) P. M. Beaujuge, C. M. Amb and J. R. Reynolds, *Acc. Chem. Rev*. **2010**, *43*, 1396-1407. (l) K. C. D. Robson, B. D. Koivisto, A. Yella, B. Sporinova, M. K. Nazeeruddin, T. Baumgartner, M. Grätzel and C. P. Berlinguette, *Inorg. Chem*. **2011**, *50*, 5494-5508.

(2) (a) P. de Fremont, N. Marion and S. P. Nolan, *Coord. Chem. Rev*. **2009**, *253*, 862-892. (b) S. Grundemann, M. Albrecht, J. A. Loch, J. W. Faller and R. H. Crabtree, *Organometallics* **2001**, *20*, 5485-5488. (c) C. Heinemann, T.

Muller, Y. Apeloig and H. Schwarz, *J. Am. Soc. Chem*. **1996**, *118*, 2023-2038. (d) W. A. Herrmann, J. Schutz, G. D. Frey and E. Herdtweck, *Organometallics* **2006**, *25*, 2437-2448. (f) H. Jacobsen, A. Correa, A. Poater, C. Costabile and L. Cavallo, *Coord. Chem. Rev*. **2009**, *253*, 687-703. (g) A. Herbst, C. Bronner, P. Dechambenoit and O. S. Wenger, *Organometallics*, **2013**, *32*, 1807-1814. (h) M. J. Ingleson and R. A. Layfield, *Chem. Commun*. **2012**, *48*, 3579-3589.

(3) (a) P. T. Chou and Y. Chi, *Chem. Eur. J*. **2007**, *13*, 380-395. (b) P. C. Wu, J. K. Yu, Y. H. Song, Y. Chi, P. T. Chou, S. M. Peng and G. H. Lee, *Organometallics* **2003**, *22*, 4938-4946..

(4) (a) F. Barigelletti, L. Flamigni, M. Guardigli, A. Juris, M. Beley, S. ChodorowskiKimmes, J. P . Collin and J. P . Sauvage, *Inorg. Chem*. **1996**, *35*, 136-142. (b) V. Dragutan, I. Dragutan, L. Delaude and A. Demonceau, *Coord. Chem. Rev*. **2007**, *251*, 765-794. (c) P. Reveco, R. H. Schmehl, W. R. Cherry, F. R. Fronczek and J. Selbin, *Inorg. Chem*. **1985**, *24,* 4078-4082. (d) S. Serroni, A. Juris, S. Campagna, M. Venturi, G. Denti and V. Balzani, *J. Am. Soc. Chem*. **1994**, *116*, 9086-9091. (e) S. H. Wadman, M. Lutz, D. M. Tooke, A. L. Spek, F. Hartl, R. W. A. Havenith, G. P. M. van Klink and G. van Koten, *Inorg. Chem*. **2009**, *48*, 1887-1900. (f) R. Amadelli, R. Argazzi, C. A. Bignozzi and F. Scandola, *J. Am. Soc. Chem*. **1990**, *112*, 7099- 7103.

(5) (a) E. C. Constable, S. J. Dunne, D. G. F. Rees and C. X. Schmitt, *Chem. Commun*. **1996**, 1169-1170. (b) E. C. Constable and L. R. Sousa, J. *Organomet. Chem*. **1992**, *427*, 125-139.

(6) (a) A. Juris, V. Balzani, F. Barigelletti, S. Campagna, P. Belser and A. Vonzelewsky, *Coord. Chem. Rev*. **1988**, *84*, 85-277. (b) J. P. Sauvage, J. P. Collin, J. C. Chambron, S. Guillerez, C. Coudret, V. Balzani, F. Barigelletti, L. Decola and L. Flamigni, *Chem. Rev*. **1994**, *94*, 993-1019. (c) K. Kalyanasundaram and M. Gratzel, *Coord. Chem. Rev*. **1998**, *177*, 347-414. (d) F. Barigelletti and L. Flamigni, *Chem. Soc. Rev*. **2000**, *29,* 1-12. (e) C. A. Bignozzi, R. Argazzi and C. J. Kleverlaan, *Chem. Soc. Rev*. **2000**, *29*, 87-96. (f) V. Balzani, G. Bergamini, F. Marchioni and P. Ceroni, *Coord. Chem. Rev*., **2006**, *250*, 1254- 1266. (g) M. H. V. Huynh, D. M. Dattelbaum and T. J. Meyer, *Coord. Chem. Rev*. **2005**, *249*, 457-483.

(7) (a) S. U. Son, K. H. Park, Y. S. Lee, B. Y. Kim, C. H. Choi, M. S. Lah, Y. H. Jang, D. J. Jang and Y. K. Chung, *Inorg. Chem*. **2004**, *43*, 6896-6898. (b) H. J. Park, K. H. Kim, S. Y. Choi, H. M. Kim, W. I. Lee, Y. K. Kang and Y. K. Chung, *Inorg. Chem*. **2010**, *49*, 7340-7352..

(8) (a) J. Dinda, S. Liatard, J. Chauvin, D. Jouvenot and F. Loiseau, *Dalton Trans*. **2011**, *40*, 3683-3688. (b) S. Das Adhikary, T. Samanta, G. Roymahapatra, F. Loiseau, D. Jouvenot, S. Giri, P. K. Chattaraj and J. Dinda, *New J. Chem*. **2010**, *34*, 1974-1980. (c) E. Fogler, E. Balaraman, Y. Ben-David, G. Leitus, L. J. W. Shimon and D. Milstein, *Organometallics* **2011**, *30*, 3826-3833. (d) S. J. Gu, B. Liu, J. X. Chen, H. Y. Wu and W. Z. Chen, *Dalton Trans*. **2012**,

41, 962-970. (e) J. A. Wright, A. A. Danopoulos, W. B. Motherwell, R. J. Carroll, S. Ellwood and J. Sassmannshausen, *Eur. J. Inorg. Chem.* **2006**, 4857-4865.

(9) (a) Heuberger, B. D.; Shin, D.; Switzer, C. *Org. Lett.* **2008**, *10,* 1091–1094. (b) Savage, S. A.; Smith, A. P.; Fraser, C. L. *J. Org. Chem*. **1998**, *63*, 10048-10051. (c) Sullivan, B. P.; Calvert, J. M.; Meyer, T. J. *Inorg. Chem*. **1980**, *19*, 1404–1407

(10) The LUMO energy levels of bpy and tpy calculated by DFT method at B3LYP/6-31g(d) level are -1.51 and -1.55 eV, respectively.

5. Supporting Information

Table 3. Compositions of the CT-state wave functions of **Ru(tpy)L** and **RuL$_2$** in terms of the linear combination coefficients in the configuration expansion[a]

State[b]	Energy		f[c]	Wavefunction	Character	Transition Dipole Moment		
	eV	cm^{-1}				au		
1, Ru(tpy)(bim)								
S1	2.54	20543	0.0112	0.1631 $\Psi_{-2\rightarrow1}$ + 0.6757 $\Psi_{0\rightarrow1}$	MLCT[d]	0.0035	-0.4225	-0.0178
S2	2.706	21828	0.0241	0.1216 $\Psi_{-1\rightarrow1}$ + 0.6693 $\Psi_{0\rightarrow2}$ - 0.1227 $\Psi_{0\rightarrow3}$ -0.1021 $\Psi_{0\rightarrow4}$	MLCT[e] + MLCT[d]	-0.5424	0.0145	-0.2635
S5	2.827	22797	0.0173	0.1041 $\Psi_{-2\rightarrow2}$ + 0.5121 $\Psi_{-1\rightarrow1}$ - 0.1573 $\Psi_{0\rightarrow2}$ -0.4334 $\Psi_{0\rightarrow3}$	MLCT[d]	-0.4997	-0.0042	0.0001
S6	2.974	23985	0.1405	0.5201 $\Psi_{-2\rightarrow2}$ + 0.2473 $\Psi_{-1\rightarrow1}$ + 0.3952 $\Psi_{0\rightarrow3}$	MLCT[e] + MLCT[d]	-1.3783	0.0511	-0.1622
S7	2.981	24043	0.0474	0.1153 $\Psi_{-1\rightarrow2}$ + 0.6889 $\Psi_{-1\rightarrow3}$	MLCT[d]	-0.0636	-0.8021	-0.0454
S9	3.136	25297	0.0307	0.4220 $\Psi_{-2\rightarrow2}$ - 0.3569 $\Psi_{-1\rightarrow1}$ - 0.3495 $\Psi_{0\rightarrow3}$ -0.1796 $\Psi_{0\rightarrow4}$ - 0.1236 $\Psi_{0\rightarrow7}$	MLCT[d] + MLCT[e]	0.3770	0.0235	-0.5072
S13	3.733	30110	0.0487	-0.1580 $\Psi_{-4\rightarrow2}$ + 0.1344 $\Psi_{-3\rightarrow2}$ + 0.5823 $\Psi_{-2\rightarrow4}$ -0.1195 $\Psi_{-1\rightarrow9}$ - 0.1913 $\Psi_{0\rightarrow4}$ + 0.1727 $\Psi_{0\rightarrow7}$	MLCT[e]	0.7170	0.0058	-0.1343
S16	3.896	31422	0.0345	0.1092 $\Psi_{-4\rightarrow2}$ + 0.1231 $\Psi_{-2\rightarrow5}$ + 0.6601 $\Psi_{0\rightarrow5}$ -0.1151 $\Psi_{0\rightarrow7}$	MLCT[e]	0.5942	-0.0023	0.0918
S19	4.001	32271	0.0114	0.4824 $\Psi_{-2\rightarrow5}$ + 0.2050 $\Psi_{-2\rightarrow7}$ + 0.3698 $\Psi_{-1\rightarrow6}$ -0.2122 $\Psi_{-1\rightarrow9}$ - 0.1431 $\Psi_{0\rightarrow5}$	MLCT[e] + MLCT[d]	-0.3226	0.0285	-0.1059
S20	4.017	32396	0.1702	-0.1493 $\Psi_{-4\rightarrow1}$ + 0.5011 $\Psi_{-3\rightarrow1}$ - 0.3540 $\Psi_{-2\rightarrow6}$ -0.1119 $\Psi_{-1\rightarrow5}$ - -0.2658 $\Psi_{0\rightarrow6}$	LLCT[f]+ MLCT[d]	-0.0129	-1.3130	-0.0714
2, Ru(tpy)(bzim)								
S3	2.792	22515	0.0418	-0.1976 $\Psi_{-1\rightarrow1}$ + 0.6429 $\Psi_{0\rightarrow2}$ + 0.1585 $\Psi_{0\rightarrow3}$	MLCT[e] + MLCT[d]	-0.0822	-0.7777	0.0000
S5	2.876	23194	0.0211	-0.1253 $\Psi_{-2\rightarrow2}$ + 0.5234 $\Psi_{-1\rightarrow1}$ + 0.2342 $\Psi_{0\rightarrow2}$ -0.3661 $\Psi_{0\rightarrow3}$	MLCT[d] + MLCT[e]	-0.3213	0.4424	0.0000
S6	3.018	24339	0.1107	0.5263 $\Psi_{-2\rightarrow2}$ - 0.2017 $\Psi_{-1\rightarrow1}$ - 0.4039 $\Psi_{0\rightarrow3}$	MLCT[e] + MLCT[d]	0.3991	-1.1565	0.0002
S7	3.022	24375	0.0455	-0.1288 $\Psi_{-1\rightarrow2}$ + 0.6871 $\Psi_{-1\rightarrow3}$	MLCT[d] + MLCT[e]	0.0001	-0.0003	-0.7844
S9	3.175	25608	0.0481	0.4111 $\Psi_{-2\rightarrow2}$ + 0.3307 $\Psi_{-1\rightarrow1}$ + 0.3986 $\Psi_{0\rightarrow3}$ -0.1491 $\Psi_{0\rightarrow4}$	MLCT[e] + MLCT[d]	-0.7624	0.1921	0.0000
S13	3.748	30228	0.0254	-0.3916 $\Psi_{-3\rightarrow2}$ + 0.4636 $\Psi_{-2\rightarrow4}$ + 0.1223 $\Psi_{-1\rightarrow10}$ -0.2261 $\Psi_{0\rightarrow4}$ + 0.1165 $\Psi_{0\rightarrow7}$	MLCT[e] + LLCT[g]	-0.0596	0.5231	0.0000
S16	3.885	31333	0.1706	0.5158 $\Psi_{-3\rightarrow2}$ + 0.2967 $\Psi_{-2\rightarrow4}$ + 0.1721 $\Psi_{-1\rightarrow10}$ 0.2382 $\Psi_{0\rightarrow5}$	LLCT[g] + MLCT[e] + MLCT[d]	-1.3320	0.1337	0.0000

S17	3.891	31381	0.0409	-0.1270	$\Psi_{-5\rightarrow1}$	+	0.4937	$\Psi_{-4\rightarrow1}$	- 0.4677	$\Psi_{0\rightarrow6}$	$LLCT^f + MLCT^d$	0.0000	0.0000	0.6551
S18	3.965	31976	0.0281	-0.1831	$\Psi_{-3\rightarrow2}$	-	0.1350	$\Psi_{-2\rightarrow4}$	+ 0.2303	$\Psi_{-2\rightarrow5}$	$MLCT^d$	0.3214	0.4307	0.0000
				0.1103	$\Psi_{0\rightarrow4}$	+	0.5826	$\Psi_{0\rightarrow5}$						
3, Ru(tpy)(b^im)														
S1	2.365	19075	0.0124	0.6788	$\Psi_{0\rightarrow1}$	+	0.1146	$\Psi_{0\rightarrow2}$			$MLCT^d + MLCT^e$	-0.2131	-0.2295	-0.3417
S5	2.834	22858	0.0886	0.4720	$\Psi_{-2\rightarrow1}$	-	0.1313	$\Psi_{-2\rightarrow2}$	+ 0.1126	$\Psi_{-2\rightarrow3}$	$MLCT^d + MLCT^e$	1.1293	0.0051	-0.0383
				-0.2160	$\Psi_{-1\rightarrow1}$	+	0.1372	$\Psi_{-1\rightarrow2}$	- 0.3246	$\Psi_{-1\rightarrow3}$				
				-0.1645	$\Psi_{0\rightarrow2}$	-	0.1900	$\Psi_{0\rightarrow3}$						
S6	2.878	23214	0.0364	0.5550	$\Psi_{-2\rightarrow2}$	-	0.3511	$\Psi_{-2\rightarrow3}$	- 0.1291	$\Psi_{-1\rightarrow1}$	$MLCT^e + MLCT^d$	0.7063	0.0808	-0.1027
				-0.1852	$\Psi_{-1\rightarrow3}$									
S7	2.902	23406	0.0302	-0.1202	$\Psi_{-1\rightarrow1}$	+	0.6060	$\Psi_{-1\rightarrow2}$	+ 0.3213	$\Psi_{-1\rightarrow3}$	$MLCT^e + MLCT^d$	0.5741	-0.0831	-0.2976
S8	2.992	24134	0.0288	0.3843	$\Psi_{-2\rightarrow2}$	+	0.5746	$\Psi_{-2\rightarrow3}$			$MLCT^d + MLCT^e$	0.0160	0.4234	0.4616
S9	3.108	25070	0.0283	0.3102	$\Psi_{-2\rightarrow1}$	-	0.1226	$\Psi_{-2\rightarrow3}$	- 0.2338	$\Psi_{-1\rightarrow2}$	$MLCT^d + MLCT^e$	0.0413	-0.5211	0.3146
				0.4781	$\Psi_{-1\rightarrow3}$	-	0.1820	$\Psi_{0\rightarrow3}$	+ 0.1242	$\Psi_{0\rightarrow7}$				
S13	3.703	29866	0.0101	0.1691	$\Psi_{-3\rightarrow1}$	+	0.5491	$\Psi_{0\rightarrow5}$	+ 0.3187	$\Psi_{0\rightarrow6}$	$MLCT^d$	0.0460	0.3073	0.1228
				0.1457	$\Psi_{0\rightarrow9}$									
S14	3.742	30181	0.0173	0.1019	$\Psi_{-1\rightarrow6}$	-	0.2708	$\Psi_{0\rightarrow5}$	+ 0.5689	$\Psi_{0\rightarrow6}$	$MLCT^d$	-0.4283	-0.0329	0.0609
				-0.1852	$\Psi_{0\rightarrow9}$									
S15	3.790	30569	0.0101	-0.1658	$\Psi_{-2\rightarrow4}$	+	0.5553	$\Psi_{-1\rightarrow4}$	+ 0.1057	$\Psi_{-1\rightarrow5}$	$MLCT^e + MC$	0.2916	-0.0975	0.1205
				-0.1753	$\Psi_{-1\rightarrow9}$	-	0.2526	$\Psi_{0\rightarrow7}$						
S16	3.819	30803	0.0066	0.5185	$\Psi_{-2\rightarrow4}$	+	0.1123	$\Psi_{-2\rightarrow5}$	- 0.1227	$\Psi_{-1\rightarrow7}$	$MLCT^e$	0.1585	-0.1158	0.1783
				-0.3665	$\Psi_{0\rightarrow7}$									
S17	3.874	31247	0.0317	-0.2205	$\Psi_{-3\rightarrow1}$	+	0.3357	$\Psi_{-2\rightarrow4}$	- 0.1271	$\Psi_{-2\rightarrow9}$	$MLCT^d + MLCT^e + LLCT^f$	0.4450	0.3625	-0.0703
				0.1500	$\Psi_{-1\rightarrow4}$	-	0.1691	$\Psi_{-1\rightarrow5}$	+ 0.4031	$\Psi_{-1\rightarrow6}$				
				0.1086	$\Psi_{-1\rightarrow7}$	+	0.2426	$\Psi_{0\rightarrow7}$						
S18	3.889	31366	0.0451	-0.3892	$\Psi_{-3\rightarrow1}$	+	0.1377	$\Psi_{-2\rightarrow5}$	- 0.1278	$\Psi_{-1\rightarrow4}$	$MLCT^d + LLCT^f$	-0.1750	0.4233	0.5132
				0.5049	$\Psi_{-1\rightarrow5}$	+	0.1352	$\Psi_{-1\rightarrow6}$	+ 0.1143	$\Psi_{0\rightarrow6}$				
S19	3.929	31688	0.0808	-0.1638	$\Psi_{-5\rightarrow1}$	-	0.1232	$\Psi_{-4\rightarrow1}$	+ 0.4112	$\Psi_{-3\rightarrow1}$	$LLCT^f + MLCT^d + MLCT^e$	0.0049	-0.4557	-0.7949
				0.1099	$\Psi_{-2\rightarrow4}$	+	0.3676	$\Psi_{-1\rightarrow5}$	- 0.1128	$\Psi_{-1\rightarrow9}$				
				0.2361	$\Psi_{0\rightarrow7}$									
S20	3.971	32032	0.0202	0.5029	$\Psi_{-2\rightarrow5}$	-	0.2411	$\Psi_{-2\rightarrow6}$	+ 0.1158	$\Psi_{-1\rightarrow4}$	$MLCT^d$	0.3779	0.1278	-0.2211
				-0.1154	$\Psi_{-1\rightarrow5}$	-	0.2524	$\Psi_{-1\rightarrow6}$	+ 0.2021	$\Psi_{0\rightarrow7}$				
4, Ru(tpy)(b^zim)														
S1	2.469	19915	0.0137	0.1081	$\Psi_{-2\rightarrow1}$	+	0.6758	$\Psi_{0\rightarrow1}$	+ 0.1009	$\Psi_{0\rightarrow2}$	$MLCT^d + MLCT^e$	0.2139	0.1722	-0.3881
S3	2.706	21821	0.0104	-0.1359	$\Psi_{0\rightarrow1}$	+	0.5948	$\Psi_{0\rightarrow2}$	- 0.3209	$\Psi_{0\rightarrow3}$	$MLCT^e + MLCT^d$	-0.3376	0.1888	-0.0836
S4	2.781	22431	0.0098	0.4081	$\Psi_{-2\rightarrow1}$	-	0.1440	$\Psi_{-1\rightarrow1}$	+ 0.2199	$\Psi_{0\rightarrow2}$	$MLCT^d + MLCT^e$	0.1072	-0.2619	-0.2526
				0.5007	$\Psi_{0\rightarrow3}$									
S5	2.886	23277	0.0899	0.3947	$\Psi_{-2\rightarrow1}$	-	0.1130	$\Psi_{-2\rightarrow2}$	- 0.1800	$\Psi_{-1\rightarrow1}$	$MLCT^d + MLCT^e$	-0.1205	-1.1129	0.1378
				0.1249	$\Psi_{-1\rightarrow2}$	-	0.3448	$\Psi_{-1\rightarrow3}$	- 0.2380	$\Psi_{0\rightarrow2}$				

				-0.2936	$\Psi_{0\rightarrow3}$									
S6	2.923	23573	0.0311	0.5567	$\Psi_{-2\rightarrow2}$	-	0.3488	$\Psi_{-2\rightarrow3}$	-	-0.1150	$\Psi_{-1\rightarrow1}$	$MLCT^{e}$ + $MLCT^{d}$	0.1164	-0.6469	0.0404
				0.1456	$\Psi_{-1\rightarrow2}$	-	0.1511	$\Psi_{-1\rightarrow3}$							
S7	2.943	23733	0.0288	0.1079	$\Psi_{-2\rightarrow3}$	-	-0.1017	$\Psi_{-1\rightarrow1}$	+	0.6080	$\Psi_{-1\rightarrow2}$	$MLCT^{e}$ + $MLCT^{d}$	0.1821	-0.5758	-0.1877
				0.3150	$\Psi_{-1\rightarrow3}$										
S8	3.036	24491	0.0283	0.3940	$\Psi_{-2\rightarrow2}$	+	0.5648	$\Psi_{-2\rightarrow3}$	-	0.1033	$\Psi_{-1\rightarrow2}$	$MLCT^{d}$ + $MLCT^{e}$	-0.1679	0.0435	0.5914
S9	3.143	25350	0.0546	0.3000	$\Psi_{-2\rightarrow1}$	-	0.1614	$\Psi_{-2\rightarrow3}$	-	0.2121	$\Psi_{-1\rightarrow2}$	$MLCT^{d}$ + $MLCT^{e}$	-0.8124	-0.0437	-0.2162
				0.4795	$\Psi_{-1\rightarrow3}$	-	0.1062	$\Psi_{0\rightarrow2}$	-	0.2004	$\Psi_{0\rightarrow3}$				
				0.1065	$\Psi_{0\rightarrow8}$										
S15	3.821	30819	0.0322	0.4218	$\Psi_{-4\rightarrow1}$	-	0.1103	$\Psi_{-1\rightarrow4}$	+	0.1303	$\Psi_{-1\rightarrow5}$	$MLCT^{d}$ + $LLCT^{h}$	-0.2522	-0.3200	0.4218
				0.4660	$\Psi_{0\rightarrow5}$	-	0.1690	$\Psi_{0\rightarrow6}$							
S18	3.849	31041	0.0237	0.1001	$\Psi_{-5\rightarrow1}$	+	0.3460	$\Psi_{-4\rightarrow1}$	+	0.1907	$\Psi_{-1\rightarrow4}$	$MLCT^{d}$ + $LLCT^{h}$	0.2569	0.3195	0.2891
				-0.1129	$\Psi_{-1\rightarrow5}$	+	0.1494	$\Psi_{-1\rightarrow6}$	+	0.4940	$\Psi_{0\rightarrow6}$				
				-0.1093	$\Psi_{0\rightarrow7}$										
								5, $Ru(bim)_2$							
S1	2.590	20886	0.0271	-0.1298	$\Psi_{-1\rightarrow2}$	+	0.6721	$\Psi_{0\rightarrow1}$	+	0.1240	$\Psi_{0\rightarrow3}$	$MLCT^{e}$	0.5996	0.0000	0.2606
S5	2.928	23615	0.1260	0.4856	$\Psi_{-2\rightarrow1}$	+	0.5028	$\Psi_{-1\rightarrow2}$				$MLCT^{e}$	1.2670	0.0000	0.3887
S6	3.033	24465	0.0297	0.4811	$\Psi_{-2\rightarrow2}$	+	0.4428	$\Psi_{-1\rightarrow1}$	+	0.1005	$\Psi_{0\rightarrow2}$	$MLCT^{e}$	0.0000	-0.6324	0.0000
				0.1748	$\Psi_{0\rightarrow4}$	+	0.1019	$\Psi_{0\rightarrow6}$							
S7	3.314	26731	0.0299	0.1337	$\Psi_{-2\rightarrow3}$	-	0.1327	$\Psi_{0\rightarrow1}$	+	0.6570	$\Psi_{0\rightarrow3}$	$MLCT^{e}$	-0.5920	0.0000	0.1338
S11	3.619	29186	0.0977	0.1047	$\Psi_{-4\rightarrow1}$	+	0.1272	$\Psi_{-3\rightarrow2}$	+	0.4937	$\Psi_{-2\rightarrow3}$		1.0161	0.0000	-0.2640
				0.4323	$\Psi_{-1\rightarrow4}$	-	0.1164	$\Psi_{0\rightarrow3}$							
S13	3.842	30987	0.0461	0.1251	$\Psi_{-2\rightarrow5}$	+	0.6746	$\Psi_{0\rightarrow5}$				$MLCT^{e}$	0.6239	0.0000	0.3168
S14	3.965	31981	0.0285	0.1112	$\Psi_{-4\rightarrow2}$	-	0.1380	$\Psi_{-3\rightarrow1}$	-	0.1304	$\Psi_{-2\rightarrow4}$	$MLCT^{e}$	0.0000	0.5416	0.0000
				0.2578	$\Psi_{-2\rightarrow6}$	+	0.1223	$\Psi_{-2\rightarrow10}$	-	0.1068	$\Psi_{-1\rightarrow5}$				
				0.5587	$\Psi_{0\rightarrow6}$										
S15	3.981	32108	0.0226	0.5581	$\Psi_{-3\rightarrow1}$	-	0.1104	$\Psi_{-2\rightarrow4}$	-	0.1015	$\Psi_{-1\rightarrow3}$	$LLCT^{i}$	0.0000	-0.4816	0.0000
				-0.3763	$\Psi_{-1\rightarrow5}$										
S16	3.988	32169	0.0521	0.6251	$\Psi_{-3\rightarrow2}$	-	0.1765	$\Psi_{-2\rightarrow5}$	+	0.1418	$\Psi_{-1\rightarrow6}$	$LLCT^{i}$ + $MLCT^{e}$	-0.3317	0.0000	0.6505
				0.1054	$\Psi_{-1\rightarrow10}$										
S19	4.073	32848	0.0181	0.1281	$\Psi_{-2\rightarrow5}$	-	0.1209	$\Psi_{-1\rightarrow10}$	-	0.1134	$\Psi_{0\rightarrow3}$	MC + $MLCT^{e}$	-0.1418	0.0000	0.4021
				-0.3235	$\Psi_{0\rightarrow7}$	+	0.4888	$\Psi_{0\rightarrow9}$	+	0.1990	$\Psi_{0\rightarrow11}$				
				0.1173	$\Psi_{0\rightarrow15}$										
S20	4.098	33053	0.0436	0.1482	$\Psi_{-4\rightarrow1}$	-	0.2106	$\Psi_{-3\rightarrow2}$	-	0.3213	$\Psi_{-2\rightarrow5}$	$MLCT^{e}$ + $LLCT^{i}$	0.6464	0.0000	-0.1285
				0.5490	$\Psi_{-1\rightarrow6}$										
								6, $Ru(bzim)_2$							
S1	2.710	21860	0.0313	0.1709	$\Psi_{-2\rightarrow1}$	-	0.1742	$\Psi_{-1\rightarrow2}$	+	0.6414	$\Psi_{0\rightarrow1}$	$MLCT^{e}$	0.0559	0.0000	-0.6841
				0.1256	$\Psi_{0\rightarrow3}$										
S2	2.781	22432	0.0109	-0.2543	$\Psi_{-1\rightarrow1}$	+	0.6424	$\Psi_{0\rightarrow2}$				$MLCT^{e}$	0.0000	0.4008	0.0000

S5	3.004	24230	0.1085	0.5038 $\Psi_{-2\rightarrow1}$ + 0.4859 $\Psi_{-1\rightarrow2}$	MLCT^e	0.4272	0.0000	-1.1368
S6	3.103	25024	0.0389	0.5081 $\Psi_{-2\rightarrow2}$ + 0.4265 $\Psi_{-1\rightarrow1}$ - 0.1435 $\Psi_{0\rightarrow4}$	MLCT^e	0.0000	0.7157	0.0000
S7	3.418	27570	0.0282	0.2060 $\Psi_{-2\rightarrow3}$ - 0.1349 $\Psi_{0\rightarrow1}$ + 0.6352 $\Psi_{0\rightarrow3}$	MLCT^e	-0.4917	0.0000	0.3076
S11	3.668	29581	0.0699	0.1752 $\Psi_{-4\rightarrow1}$ - 0.2369 $\Psi_{-3\rightarrow2}$ + 0.4738 $\Psi_{-2\rightarrow3}$ -0.3653 $\Psi_{-1\rightarrow4}$ - 0.1465 $\Psi_{0\rightarrow3}$	MLCT^e + LLCT^i	0.7003	0.0000	-0.5363
S12	3.737	30137	0.0180	-0.1738 $\Psi_{-4\rightarrow2}$ + 0.4953 $\Psi_{-3\rightarrow1}$ + 0.3448 $\Psi_{-2\rightarrow4}$ -0.2273 $\Psi_{0\rightarrow4}$	LLCT^i + MLCT^e	0.0000	-0.4431	0.0000
S13	3.840	30971	0.1542	-0.1308 $\Psi_{-4\rightarrow1}$ + 0.6135 $\Psi_{-3\rightarrow2}$ + 0.1913 $\Psi_{-2\rightarrow3}$ -0.1583 $\Psi_{-1\rightarrow4}$	LLCT^i + MLCT^e	1.2801	0.0000	0.0034
S14	3.864	31164	0.0143	0.2551 $\Psi_{-4\rightarrow2}$ + 0.4803 $\Psi_{-3\rightarrow1}$ - 0.2977 $\Psi_{-2\rightarrow4}$ 0.1601 $\Psi_{-1\rightarrow3}$ + 0.2038 $\Psi_{0\rightarrow4}$ - 0.1142 $\Psi_{0\rightarrow8}$	LLCT^i + MLCT^e	0.0000	-0.3889	0.0000
S15	3.875	31250	0.0431	0.6376 $\Psi_{-4\rightarrow1}$ + 0.2187 $\Psi_{-3\rightarrow2}$ - 0.1543 $\Psi_{0\rightarrow5}$	LLCT^i + MLCT^e	-0.6639	0.0000	-0.1158
S16	3.911	31541	0.0666	0.6061 $\Psi_{-4\rightarrow2}$ + 0.2375 $\Psi_{-2\rightarrow4}$ - 0.1203 $\Psi_{-1\rightarrow3}$ -0.1186 $\Psi_{0\rightarrow4}$ - 0.1108 $\Psi_{0\rightarrow6}$	LLCT^i + MLCT^e	0.0000	0.8340	0.0000
S17	3.982	32116	0.0328	-0.1498 $\Psi_{-5\rightarrow2}$ 0.1737 $\Psi_{-4\rightarrow1}$ + 0.2056 $\Psi_{-2\rightarrow5}$ 0.6153 $\Psi_{0\rightarrow5}$	MLCT^e + LLCT^i	-0.2635	0.0000	-0.5162
S19	4.061	32757	0.0788	0.4412 $\Psi_{-5\rightarrow1}$ + 0.1007 $\Psi_{-4\rightarrow2}$ + 0.2922 $\Psi_{-2\rightarrow6}$ 0.1125 $\Psi_{-2\rightarrow12}$ + 0.3874 $\Psi_{0\rightarrow6}$	LLCT^i + MLCT^e	0.0000	0.8898	0.0000
S20	4.071	32835	0.0265	0.6765 $\Psi_{-5\rightarrow2}$ + 0.1438 $\Psi_{-2\rightarrow5}$	LLCT^i + MLCT^e	-0.4010	0.0000	-0.3243
				7, Ru(b^im)$_2$				
S1	2.405	19395	0.0189	-0.1484 $\Psi_{-1\rightarrow2}$ + 0.6814 $\Psi_{0\rightarrow1}$	MLCT^e	0.0000	0.0000	-0.5671
S2	2.443	19706	0.0080	-0.2956 $\Psi_{-1\rightarrow1}$ + 0.6352 $\Psi_{0\rightarrow2}$	MLCT^e	-0.2778	0.2388	0.0000
S3	2.590	20889	0.1086	0.6302 $\Psi_{-1\rightarrow1}$ + 0.2947 $\Psi_{0\rightarrow2}$	MLCT^e	-1.3005	0.1435	0.0000
S5	2.812	22681	0.0239	0.6961 $\Psi_{-2\rightarrow2}$	MLCT^e	0.5873	-0.0433	0.0001
S6	2.814	22699	0.0319	-0.3407 $\Psi_{-2\rightarrow1}$ + 0.5788 $\Psi_{-1\rightarrow2}$ + 0.1648 $\Psi_{0\rightarrow1}$	MLCT^e	0.0001	0.0000	-0.6797
S9	3.453	27849	0.0275	0.6596 $\Psi_{-1\rightarrow3}$ + 0.1022 $\Psi_{-1\rightarrow6}$ - 0.1553 $\Psi_{-1\rightarrow10}$	MLCT^e	0.5298	0.2097	0.0000
S10	3.547	28611	0.0459	0.6826 $\Psi_{0\rightarrow5}$	MLCT^e	0.3995	-0.6067	0.0000
S13	3.686	29734	0.0122	0.1578 $\Psi_{-2\rightarrow3}$ + 0.1369 $\Psi_{-1\rightarrow4}$ + 0.5457 $\Psi_{-1\rightarrow5}$ -0.3747 $\Psi_{0\rightarrow6}$	MLCT^e	0.0000	0.0000	0.3682
S14	3.762	30342	0.0477	-0.1676 $\Psi_{-3\rightarrow2}$ + 0.2855 $\Psi_{-2\rightarrow3}$ - 0.1139 $\Psi_{-2\rightarrow10}$ -0.1803 $\Psi_{-1\rightarrow4}$ + 0.2992 $\Psi_{-1\rightarrow5}$ + 0.4745 $\Psi_{0\rightarrow6}$	MLCT^e	0.0000	0.0000	-0.7195
S15	3.770	30406	0.0202	0.6199 $\Psi_{-2\rightarrow4}$ - 0.1044 $\Psi_{-2\rightarrow5}$ + 0.2757 $\Psi_{-1\rightarrow6}$	MLCT^e	-0.4675	-0.0091	0.0000
S17	3.855	31094	0.0224	0.6641 $\Psi_{-3\rightarrow1}$ + 0.1009 $\Psi_{-2\rightarrow4}$ + 0.1707 $\Psi_{-2\rightarrow5}$	MLCT^e	-0.3916	0.2893	0.0000
S18	3.904	31486	0.0238	-0.1898 $\Psi_{-3\rightarrow1}$ + 0.6571 $\Psi_{-2\rightarrow5}$ + 0.1330 $\Psi_{-1\rightarrow6}$	MLCT^e	0.4847	-0.1183	0.0000

[a]Subscripts correspond to the following orbitals: The highest occupied orbitals have i ndex 0, i.e. 0 = HOMO, while all other occupied orbitals have index –1. –2. …, -*n*, which correspond to HOMO-1, HOMO-2, …, HOMO-*n*, respectively. LUMO = 1, L UMO+1 = 2, LUMO+2 = 3, and so on. [b]State numbers obtained from the c alculatio

n. [c]Oscillator strength. [d]Charge transfer from metal to terpyridine. [e]Charge transfer fr om metal to bipyridyl part of NNC or NN^C ligand. [f]π–π* of terpyridine ligand. [g]C harge transfer from imidazole part to bipyridyl part of NNC or NN^C ligand. [h]Charg e transfer from imidazole part of NNC or NN^C ligand to terpyridine ligand. [i]π–π* of NNC or NN^C ligand.

국 문 초 록

서울대학교 대학원

화 학 부

김 형 묵

새로운 전자 이동 시스템으로 퀴논을 포함한 $\pi - \pi$ 쌓임 구조의 $[Ru(tpy)_2]^{2+}$를 합성하였다. tpy에 결합한 퀴논은 다른 tpy의 중앙 피리딘 고리와 반데르발스 거리를 두고 평행하게 병치되는 구조적 특이성을 가졌다. 전자 제공체와 수용체의 가까운 거리 때문에 강한 상호작용이 예상되었으나, 특징적인 전하 전이 띠를 관찰할 수 없었다. 따라서 일반적인 Mulliken-Hush 방법으로 측정할 수 없었던 H_{DA}를 처음으로 TrIR 분광법으로 확인하였다. 전자 이동은 퀴논의 카보닐 작용기의 신축 진동수 변화로 확인했으나, 구체적인 이동 경로는 알 수 없었다. 전자 이동 경로를 알아내기 위해, 앞서 합성한 화합물에서 tpy를 대신하여 전자 제공 능력이 강한 NHC로 바꾸고 리간드의 전자 비편재화를 막기 위해 메틸렌 작용기로 간격을 둔 리간드를 적용한 화합물을 새로 합성하였다. TrIR 분광법과 바닥 상태와 들뜬 상태의 진동수 시뮬레이션을 통해 전자 이동은 공유 결합을 통해서가 아니라 공간적으로 $\pi - \pi$ 쌓임 구조를

통해 일어남을 확정하였다. 더불어, Ru(NHC) 화합물에서의 구조와 물성의 상관관계에 영향을 미치는 요인을 알아내고자 7가지의 새로운 Ru(NHC) 화합물을 합성하였다. 분광학적, 전기화학적 측정으로 λ_{max}는 오직 NHC에 의해 결정되는 산화전위에 의해서만 결정됨을 알 수 있었고, Ru(NHC)의 λ_{max}를 조절할 수 있게 되었다.

주요어: 루테늄, 폴리피리딜, 카벤, 퀴논, 광유도 전자 전이

학번: 2007-20302